Forschungszentrum Jülich
in der Helmholtz-Gemeinschaft

MHD analysis of edge instabilities in the JET tokamak

Christian Pérez

promotoren: Prof. Dr. F. C. Schüller
Prof. Dr. R. Wolf
co-promotor: Dr. H. R. Koslowski

MHD analysis of edge instabilities in the JET tokamak /
by Christian P. Pérez von Thun
- Met een samenvatting in het Nederlands -

Proefschrift Universiteit Utrecht
ISBN: 90-393-3611-3
Printed in the Forschungszentrum Jülich GmbH

Electronic Version
Published by Eigenverlag der Forschungszentrum Jülich GmbH, Zentralbibliothek
Persistent Identifier: urn:nbn:de:0001-00101
Resolving URL: http://nbn-resolving.de/urn/resolver.pl?urn=urn:nbn:de:0001-00101

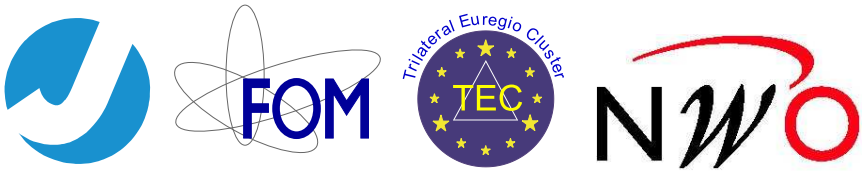

The work described in this thesis was performed as part of the research program of the EURATOM associations Institut für Plasmaphysik of the Forschungszentrum Jülich (FZJ) and the 'Stichting voor Fundamenteel Onderzoek der Materie' (FOM). Additional financial support was provided in the framework of the European Fusion Development Agreement (EFDA) by EURATOM and by the 'Nederlandse Organisatie voor Wetenschappelijk Onderzoek' (NWO). The work was carried out at the Institut für Plasmaphysik at the Forschungszentrum Jülich (Germany) and at the Joint European Torus (JET) at the Culham Science Centre (UK), in collaboration with the FOM-instituut voor Plasmafysica 'Rijnhuizen'.

a mis padres

Contents

Chapter 1

Introduction

1.1 Nuclear fusion

The ultimate aim of fusion energy research is to make progress towards demonstrate the scientific and technological feasibility of a nuclear fusion reactor, and to assess its sustainable qualities as an energy source for future generations. The fusion reaction with the largest cross section, and thus the least difficult reaction to initiate on earth, is that between the hydrogen isotopes deuterium and tritium:

$$\mathrm{D} + \mathrm{T} \rightarrow {}^{4}\mathrm{He}\ (3.5\ \mathrm{MeV}) + \mathrm{n}\ (14.1\ \mathrm{MeV})$$

resulting in the production of a fast alpha-particle and a fast neutron. Since the total mass of the fusion products is lower than the total mass before the reaction ("mass defect"), the equivalent amount of energy ($E = mc^2$) is released as kinetic energy of the fusion products. In a reactor, this energy is used for the production of electricity.

For the fusion process to take place the Coulomb repulsion of the positively charged nuclei has to be overcome. To produce sufficient reactions the temperature in a reactor has to be in the order of 100 to 200 million K. At such high temperatures matter is in a plasma state, that is, the atoms are ionised to form a "gas" of charged particles. The hot plasma has to be kept away from the surrounding material. Mainly two approaches have been developed which are compatible with such high temperatures: inertial confinement fusion and magnetic confinement fusion.

Inertial fusion uses laser or particle beams directed at frozen D-T pellets to reach the necessary fusion temperatures at high density but during extremely short periods. The plasma is free to expand, but because of its finite mass, it takes a finite time to fly apart. During this time the thermonuclear burn process has to be completed. The main challenge for reactor implementation will be the repetition rate at which beams and lasers can be operated, and fuel pellets produced.

Magnetic confinement fusion employs a strong magnetic field to confine the plasma, and is the concept relevant for this thesis. It makes use of the Lorentz force, which causes charged particles to move in helical orbits (Larmor orbits) around magnetic field lines in a uniform magnetic field. In the absence of collisions or fluctuations, the particles (more precisely: their guiding centres) remain tied to the field lines but are free to move along them. The confined plasma may then be heated by external means such as highly energetic particle beams (so-called neutral beam injection, or NBI), radiofrequency waves (ion cyclotron resonance heating, or ICRH) or microwaves (electron cyclotron resonance heating, or ECRH). In a reactor, the (doubly positively charged) alpha-particles produced in D-T reactions remain captured in the magnetic field, and transfer their energy back to the plasma through collisions. The plasma can thus sustain the heat by itself. Ignition is achieved when all external heat sources can be turned off. In contrast, the (uncharged) neutrons produced in large quantities through the D-T reaction are not affected by the magnetic field and directly escape from the plasma. They provide the basis for the electricity production of the power plant.
In practice, collisions and fluctuations will cause the particles to be confined only for a finite time inside the plasma. A sufficiently good confinement is important to reach ignition in a reactor of acceptable size. For the range of temperatures relevant for a fusion reactor (T = 10-20 keV) and neglecting the influence of impurities and helium ash in the plasma, the ignition condition requires

$$nT\tau_E \geq 3 \cdot 10^{21} \text{ m}^{-3}\text{keV s}$$

where n is the plasma density and τ_E is a measure for the quality of confinement, the energy confinement time. The quality of confinement strongly depends on the magnetic field geometry of the device. Various concepts have been studied over the last decades. Of all these, the tokamak is the most studied and most advanced fusion machine to date, and is the most likely system to demonstrate a burning fusion plasma.

1.2 The problem of Edge Localised Modes

Under certain conditions, it is observed that a transport barrier for energy and particles develops near the boundary of a tokamak plasma (and of some other fusion machines as well). This leads to the formation of a region with steep pressure gradients at the plasma edge and to an overall improvement of the energy confinement. Hence, the existence of an edge transport barrier is beneficial for the performance of a burning fusion plasma.
In such a situation, a class of plasma instabilities that have been called Edge Localised Modes, or ELMs, often occurs. The ELM bursts cause a partial collapse of the edge transport barrier, and lead to a sudden expulsion of energy

and particles out of the confined plasma. ELMs therefore tend to lower the efficiency of a burning fusion plasma. The energy bursts associated with ELMs may further lead to high transient heat loads onto plasma facing components, and thus reduce their lifetime below acceptable levels. However, ELMs are not purely detrimental. They help to avoid the accumulation of impurities in the plasma, and allow for stationary operation in the presence of an edge transport barrier.
ELMs constitute an extensive and very important field of present nuclear fusion research. The basic question is whether a good compromise can be found between sufficient particle exhaust, good enough energy confinement and tolerable transient heat loads in a burning fusion plasma.

1.3 This thesis

ELMs are a complex phenomenon and not well understood yet. This thesis intends to contribute to this field of research. The aim is to elucidate the origin of the ELM and advance the understanding of the plasma edge stability. The main emphasis is placed on the analysis of experimental data. Where found appropriate, extensive modelling calculations are also used.
For the purpose of this thesis the JET tokamak has been chosen, the world's largest tokamak. The thesis has been supported by an extensive team of specialists. For the analysis of JET discharges several high quality diagnostics as well as MHD-analysis codes have been used. In addition, an extensive collection of Matlab-based data analysis routines has been developed within this thesis and successfully applied.
In this thesis, the role of various edge instabilities observed in JET is explored. Their properties are analysed in detail, and the observations made are compared with theoretical predictions. An interpretation of the results in the context of present ELM models is given.
The outline of the thesis is as follows: First, some basic concepts, such as the tokamak and the divertor, are briefly discussed in chapter 2. Chapter 3 gives a general introduction to the theory and the phenomenology of ELMs. Chapter 4 gives an overview of the experimental setup, including the JET device, the diagnostics relevant for this thesis, and the various data analysis methods deployed. Chapters 5 and 6 form the main chapters of this thesis. In chapter 5 the characteristics of a class of edge instabilities that regularly precedes type-I ELMs on JET are discussed in detail. Chapter 6 presents evidence for the involvement of a type of instability, called the Washboard Mode, in the ELM and plasma edge dynamics. It further explores the relationship of Washboard Modes with a regime recently identified at JET that has been called the mixed type-I/type-II ELM regime. Finally, a discussion of the results is given and future plans are outlined.

1.4 Publications related to this thesis

Journal contributions

C P Perez, H R Koslowski, G T A Huysmans, T C Hender, P Smeulders, B Alper, E de la Luna, R J Hastie, L Meneses, M F F Nave, V Parail, M Zerbini and JET-EFDA contributors, *Type-I ELM precursor modes in JET*, EFDA-JET-PR(02)11 (preprint available online at http://www.iop.org/Jet/main), submitted to *Nucl. Fusion*

C P Perez, H R Koslowski, T C Hender, P Smeulders, A Loarte, P J Lomas, G Saibene, R Sartori, M Becoulet, T Eich, R J Hastie , G T A Huysmans, S Jachmich, A Rogister, F C Schüller and JET EFDA contributors, *Washboard modes as ELM-related events in JET*, *Plasma Phys. Control. Fusion* **46** (2004) 61-87

H R Koslowski, B Alper, T Eich, S E Sharapov, C P Perez, E Westerhof and JET-EFDA contributors, *Observation of the palm tree mode, a new MHD mode excited by type-I ELMs on JET*, to be submitted to Nucl. Fusion

Conference contributions

C P Perez, H R Koslowski, G T A Huysmans, P Smeulders, B Alper, T C Hender, L Meneses, M Zerbini and contributors to the EFDA-JET workprogramme, *Type-I ELM precursor modes in JET*, Proc. 29th EPS Conf. on Controlled Fusion and Plasma Physics (Montreux, 2002), P1.023

C P Perez, H R Koslowski, G T A Huysmans, P Smeulders, B Alper, T C Hender, L Meneses, M Zerbini and contributors to the EFDA-JET workprogramme, *Type-I ELM precursor modes in JET*, CPS conference 2002

H R Koslowski, C P Perez, G D Conway, P J Lomas, G Saibene, R Sartori and JET-EFDA contributors, *Relation between type-II ELMs, edge localised turbulence, washboard modes and energy losses between ELMs in high density ELMy H-modes on JET*, Proc. 30th EPS Conf. on Controlled Fusion and Plasma Physics (St Petersburg, 2003), ECA Vol. 27A, P-1.102

H R Koslowski, C P Perez, B Alper, T Eich, T C Hender, G T A Huysmans, S E Sharapov, P Smeulders, E Westerhof and JET-EFDA contributors, *Observation of Pre- and Postcursor Modes of Type-I ELMs on JET*, Proc. 19th IAEA Fusion Energy Conf. (Lyon, 2002), EX/P1-14

H R Koslowski, M F F Nave, B Alper, C P Perez, S D Pinches, O Sauter, S E Sharapov and contributors to the EFDA-JET workprogramme, *MHD studies in radiating mantel plasmas on JET*, Proc. 28th EPS Conf. on Controlled Fusion and Plasma Physics (Funchal, 2001), ECA Vol. 25A, P3.010

G Saibene *et al* (many authors), *Pedestal and ELM characterisation of highly shaped single null and quasi double null plasmas in JET*, Proc. 30th EPS Conf. on Controlled Fusion and Plasma Physics (St Petersburg, 2003), ECA Vol. 27A, P-1.092

A Loarte, G Saibene, R Sartori, M Becoulet, P J Lomas, S Ali-Arshad, B Alper, M Beurskens, M Kempenaars, H R Koslowski, C P Perez, A Kallenbach, W Suttrop, *Correlation of type-I ELM energy losses with pedestal plasma characteristics and global discharge parameters in JET ELMy H-modes*, Proc. 30th EPS Conf. on Controlled Fusion and Plasma Physics (St Petersburg, 2003), ECA Vol. 27A, P-1.096

R Sartori *et al* (many authors), *Interaction between core and edge in JET ELMy H-modes with mixed Type I-II ELMs: consequences for the extension of this regime towards high plasma current*, Proc. 30th EPS Conf. on Controlled Fusion and Plasma Physics (St Petersburg, 2003), ECA Vol. 27A, P-1.101

Invited talks

C P Perez *Washboard modes as ELM-related events in JET*, Culham Colloquium (Culham, 2002)

Chapter 2

Some basic concepts

2.1 Tokamaks

A tokamak [1] is a toroidal device in which a strong toroidal magnetic field is generated by a toroidal field coil system, and a poloidal magnetic field is created by a toroidal current I_p flowing through the plasma. The toroidal current is induced by means of a transformer. The plasma itself forms the secondary winding of the transformer, the primary winding being (usually) wound on an iron core. Figure 2.1 gives a schematic overview of a tokamak. Since the plasma ring has a natural tendency to expand radially outwards in an effort to lower its magnetic energy, a vertical magnetic field B_{V} is also needed. B_{V} interacts with the toroidal current to give an inward force. Extra field coils may be used to change the shape of the plasma cross section. For instance, D-shaped plasmas (in other words, plasmas with a certain amount of *elongation* and *triangularity*, as defined in figure 2.2) are found to have better confinement properties than plasmas with circular cross section, and are therefore often employed.
In reality, not all the current I_p flowing in the tokamak plasma is induced by the transformer. There are certain currents which naturally arise from kinetic effects in the plasma (in particular, from particle drifts that ultimately arise from the natural spatial inhomogenity of the magnitude of the magnetic field in a tokamak, $B \sim 1/R$). One such current is the so-called bootstrap current [2]. It flows parallel to the magnetic field lines, and its magnitude depends on the shape of the radial electron and ion temperature profiles, as well as the density profile. High bootstrap current density can be expected in regions with strong radial decay of density or temperature. For given profiles the magnitude of the bootstrap current does also depend on the frequency of particle collisions, more precisely, on a quantity called electron collisionality $\nu_e(r)$, which is proportional to the ratio n_e/T_e^2. Basically, the higher ν_e is the smaller the bootstrap current density becomes. The physics behind the bootstrap current is complex, and its detailed discussion goes out of the scope of this thesis. Over the years exten-

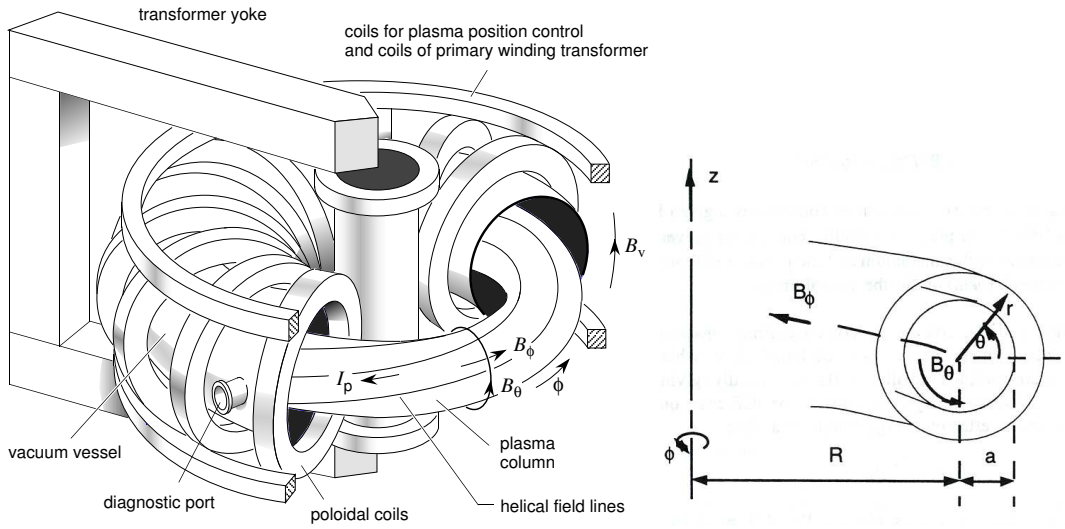

Figure 2.1: Schematic drawing of a tokamak. A toroidal vacuum vessel containing the plasma is surrounded by a set of poloidal coils which produces the toroidal magnetic field B_ϕ. A transformer induces a current I_p in the plasma, which gives rise to a poloidal magnetic field B_θ. The combination of B_ϕ and B_θ results in a magnetic field with helical structure which confines the plasma. Additional externally applied magnetic fields, such as the vertical field B_v, are necessary to maintain the plasma ring in its position. The coordinate definitions used in this thesis are shown to the right, including the major radius R, the minor radius r, the toroidal angle ϕ and the poloidal angle θ.

sive analytical formulas for the calculation of the bootstrap current have been elaborated. The interested reader may find the present state-of-the-art formulas, which are routinely employed in a number of numerical transport codes, in [3]. In addition to the above, it is worth mentioning that it is possible to drive current externally by applying electromagnetic waves to the plasma, either in the radiofrequency range (ion cyclotron current drive, ICCD) or the microwave range (electron cyclotron current drive, ECCD, or lower hybrid current drive, LHCD). The presence of a toroidal and a poloidal magnetic field results in a set of helical field lines located on closed surfaces nested around the plasma center (so-called magnetic surfaces). For each magnetic surface the helicity of the magnetic field lines can be described with the so-called safety factor q, given in approximation for circular cross sections of the magnetic surfaces by

$$q(r) = \frac{1}{2\pi} \oint \frac{r}{R} \frac{B_\phi}{B_\theta} \, \mathrm{d}\theta$$

where the integral is carried out over a single poloidal circuit around the flux surface. It should be noted that the expression for q becomes more complicated in case the shape of the cross section of magnetic surfaces becomes non-circular

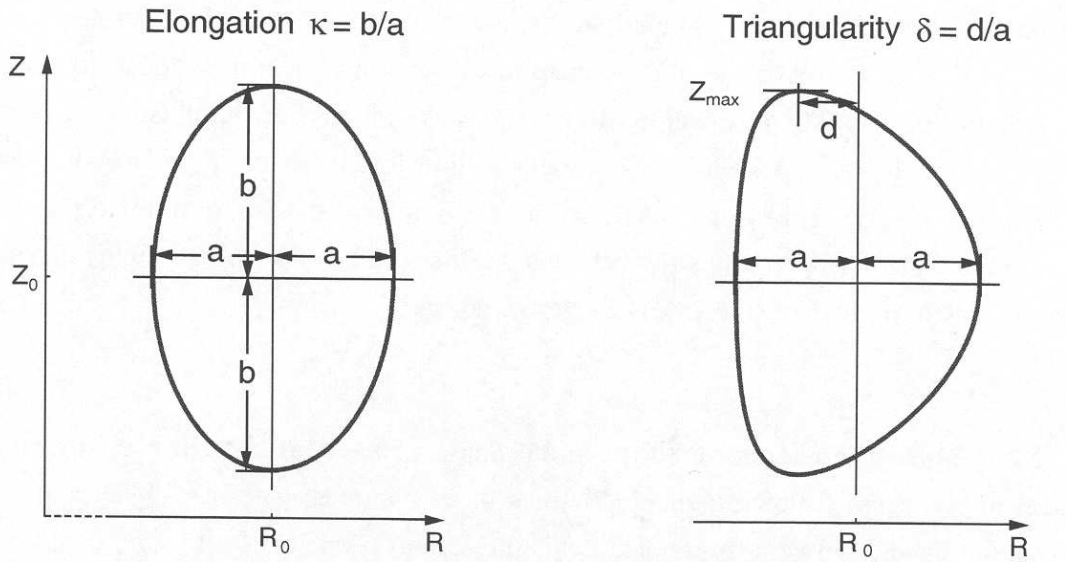

Figure 2.2: Definition of (a) the elongation κ, and (b) the triangularity δ, for a plasma with a minor radius a.

like in figure 2.4. q specifies for a given magnetic surface the number of toroidal turns necessary to perform a complete poloidal turn along a field line. If q is equal to a number being the ratio of two integers m/n, then the field lines close on themselves after performing m poloidal and n toroidal turns. If q is irrational, then the field lines are not closed and cover ergodically the whole magnetic surface. The name "safety factor" comes from the important role of q in the stability of tokamak plasmas. In standard operational scenarios in tokamaks q(r) has a minimum on the magnetic axis (usually $q(0) \approx 1$), and increases monotonically towards the plasma edge. The notation q_X is often encountered in literature and is used to denote the value of q for a particular magnetic flux surface. Here X is a number that stands for the percentage of the poloidal magnetic flux that surrounded by that surface with respect to the poloidal magnetic flux that is surrounded by the plasma boundary. Hence, X goes from 0 at the magnetic axis to 100 at the separatrix. For instance, q_0 and q_{95} denote the value of the safety factor at the plasma center and near the plasma boundary, respectively.
A related quantity describing the variation of q across the magnetic surfaces is the magnetic shear, s, defined (again, for simplicity, in the approximation of circular flux surfaces) as

$$s(r) = \frac{r}{q}\frac{\mathrm{d}q}{\mathrm{d}r}$$

Another quantity relevant for stability is the plasma beta, β, which is a measure of the efficiency of confinement of plasma pressure by the magnetic field, and is represented in a simple way by the ratio

$$\beta = \frac{\langle p \rangle_V}{B^2/2\mu_0}$$

where $\langle p \rangle_V$ denotes the plasma pressure averaged over the plasma volume, and B is the total magnetic field, usually taken at the magnetic axis. A related quantity is the poloidal beta, β_p, defined as

$$\beta_p = \frac{\langle p \rangle_S}{\langle B_\theta \rangle_S^2/2\mu_0}$$

where now the pressure and the poloidal magnetic field are averaged over the flux surface at the plasma boundary.
Several tokamak devices are being currently operated for fusion energy research around the world. The largest tokamaks are JET (Abingdon, UK), JT-60U (Naka, Japan), DIII-D (San Diego, US) and ASDEX Upgrade (Garching, Germany). The material presented in this thesis is based on measurements made on JET. The next step in the development of fusion energy research towards a reactor is the planned tokamak ITER [4,5], the aim of which is to demonstrate a burning fusion plasma for the first time (a burning fusion plasma means that a significant part of the plasma heating is provided by the α-particles of the fusion reaction). Figure 2.3 gives an overview of the ITER device, together with some of the main plasma parameters.

2.2 The divertor

A burning fusion plasma will have to exhaust particles (mainly the thermalised α-particles) and energy (which leaves the plasma in the form of radiation or of kinetic energy of the escaping particles). A possible solution for the exhaust of energy and particles is the poloidal field divertor configuration. This configuration is generated by extra field coils basically consisting of conductors that are concentric with the plasma current. The resulting magnetic configuration can be divided into two zones, separated by so-called separatrix (see figure 2.4). Inside the separatrix, where the hot fusion plasma is confined, the magnetic field is composed of nested magnetic surfaces. A particle escaping from this inner zone towards the outside (into the so-called scrape-off layer, SOL) meets field lines that convey it to a target plate in the exhaust region.
The point where the poloidal field is zero is called the X-point. Note that the X-point also implies that the safety factor q becomes infinity at the separatrix. Plasma configurations with one X-point (most often located at the bottom of

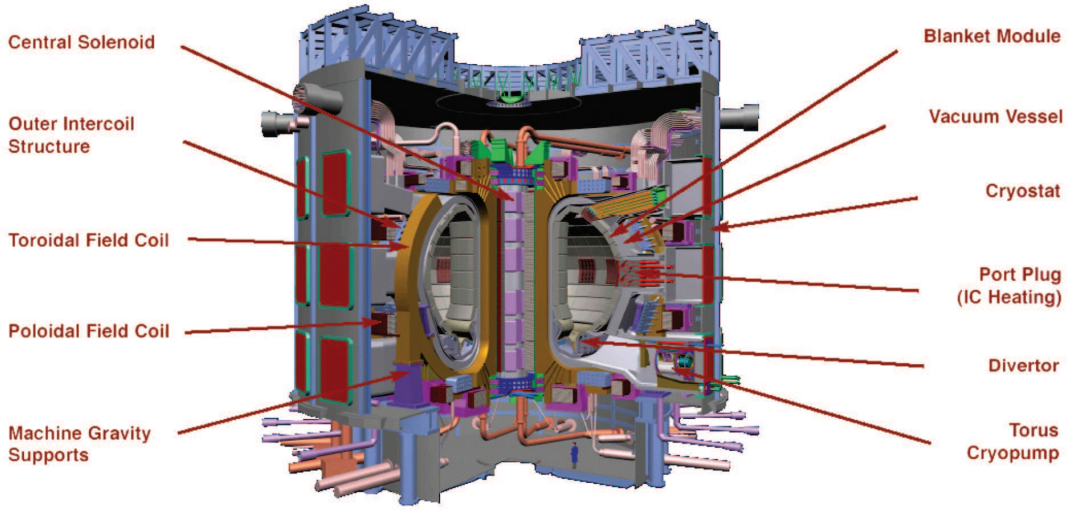

Main Plasma Parameters and Dimensions	
Total fusion power	*500 MW*
Q — Fusion power/auxiliary heating power	*≥ 10*
Average (14 MeV) neutron wall loading	*0.57 MW/m²*
Plasma major radius	*6.2 m*
Plasma minor radius	*2.0 m*
Plasma current	*15 MA*
Toroidal field @ 6.2 m radius	*5.3 T*
Plasma Volume	*837 m³*
Installed auxiliary heating/current drive power	*73 MW*

Figure 2.3: Schematic overview of the ITER device [5].

the plasma) are called single null (SN) configurations. Double null (DN) configurations have two X-points, one at the top and one at the bottom of the plasma. The points where the separatrix hits the target plates in the divertor are called the strike points. For each X-point there are two strike points: one in the inner and one in the outer part of the divertor.

The divertor target plates are heated by the incoming energy and bombarded by the escaping particles. It is important to (i) reduce the power density to the target plates to levels that can be handled by state-of-the-art materials and cooling techniques, and (ii) decrease the kinetic energy of the incoming particles below the threshold energy at which target damage occurs.

This task becomes particularly critical due to the existence of certain plasma instabilities localised near the plasma boundary, the so-called Edge Localised Modes (ELMs). ELMs are relaxation oscillations which cause quasi-periodic heat and particle losses of short duration (typically in the order of 100 μs), but

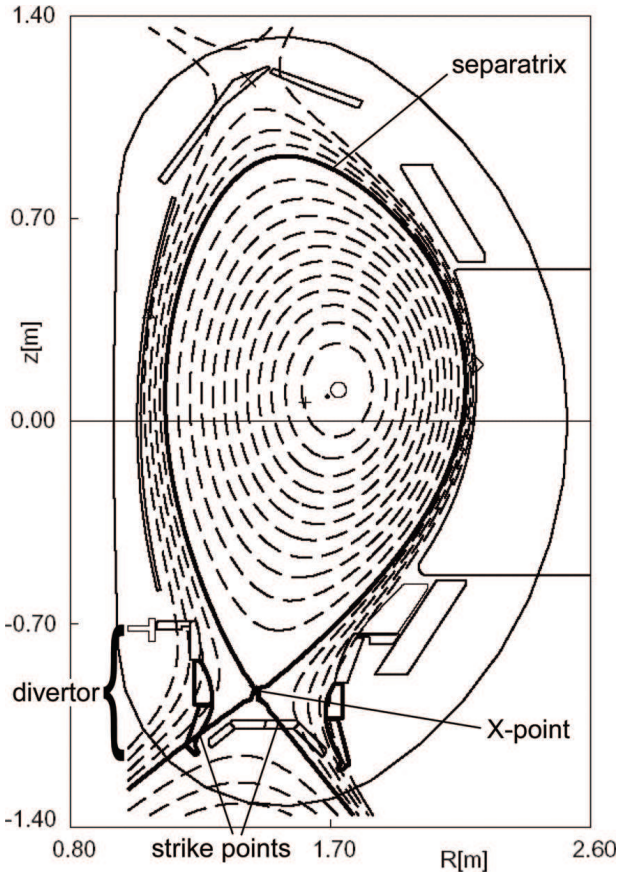

Figure 2.4: Magnetic contour lines for a typical discharge in the divertor tokamak ASDEX Upgrade.

of high energy, into the SOL, and thus also into the divertor. They further have an influence on the plasma confinement. Empirically, at least three different types of ELMs have been identified, which are normally classified as "type-I" to "type-III" ELMs. Much effort has been spent world-wide in an attempt to improve the understanding of these instabilities, and to explore ELM scenarios which combine high confinement with tolerable heat loads, also when extrapolating to a burning fusion plasma experiment such as ITER. This thesis is meant to give a contribution to this field of research.

2.3 Plasma stability

An important subject in nuclear fusion research is the study of equilibrium and stability of a plasma with respect to large scale displacements. Generally, instabilities lead to a deterioration of the energy and particle confinement, or, in the worst case (only for tokamaks), to a rapid and violent termination of the dis-

charge ("disruption"). Evidently, the plasma must preferably be operated in a regime where it is stable against these displacements. On the other hand, some instabilities can be beneficial, e.g. to avoid accumulation of impurities in the plasma and allow for stationary plasma operation, and may thus be desirable. One of the simplest self-consistent models for the description of these large scale motions is magnetohydrodynamics (MHD), where the plasma is modelled as a conducting fluid embedded in a magnetic field. Because of the relative simplicity of the MHD equations, it is possible to (in most cases numerically) calculate the stability properties of a plasma in the complicated geometry of a tokamak. This in turn allows for the predictions of MHD theory to be compared with the experimentally observed instabilities.

One general classification of the different MHD instabilities divides the modes into ideal and resistive modes. In ideal MHD, the plasma is assumed to have an infinite electrical conductivity, while in resistive MHD the finite resistivity, η, of the plasma is taken into account. Inclusion of finite resistivity can generally have an impact on the plasma stability, and give rise to effects not predicted in ideal MHD theory, such as magnetic field line reconnection. However, for modes predicted to be ideally unstable, finite resistivity leads only to small corrections and plays a minor role.

Given an axisymmetric plasma in equilibrium, in ideal MHD the energy of a linear perturbation around the equilibrium is given by [6]:

$$\begin{aligned}\delta W &= \frac{1}{2}\int_P \mathrm{d}V \Big[|\vec{Q}_\perp|^2 + B^2|\nabla\cdot\vec{\xi}_\perp + 2\vec{\xi}_\perp\cdot\vec{\kappa}|^2 + \gamma p|\nabla\cdot\vec{\xi}|^2 \\ &\quad -2(\vec{\xi}_\perp\cdot\nabla p)(\vec{\kappa}\cdot\vec{\xi}^*_\perp) - j_\parallel B^{-1}(\vec{\xi}^*_\perp\times\vec{B})\cdot\vec{Q}_\perp\Big] \qquad (2.1)\end{aligned}$$

where $\vec{\xi}(\vec{r})$ is an arbitrary displacement of a plasma volume element at the position $\vec{r}$, $\vec{B}$ and $j_\parallel$ are the equilibrium magnetic field and the current density parallel to the magnetic field, respectively, $\vec{\kappa}$ is the curvature vector of the magnetic field, and $\vec{Q}$ is the linear perturbation of the magnetic field. The plasma is stable if $\delta W \geq 0$ for any displacement $\vec{\xi}$. The first three terms in (2.1) are positive definite (thus stabilizing) and describe the contributions from field line bending, compression of the magnetic field, and plasma compression, respectively. The two terms which are not positive definite constitute the driving forces of the ideal instabilities, notably the current density parallel to the magnetic field, $j_\parallel$, and the pressure gradient ∇p. The pressure gradient is destabilizing only in those regions of the plasma where the curvature of the magnetic field lines is positive, which is, in general, the outside of the torus.

Since field line bending is stabilizing, plasma instabilities tend to align with the field lines of the equilibrium magnetic field, and thus have helical structure. In the approximation of "straight" (cylindrical) tokamak geometry the equilibrium is symmetric in θ and ϕ. Hence, the plasma displacement may be Fourier de-

composed as follows

$$\vec{\xi}(\vec{r}) = \vec{\xi}(r)e^{i(m\theta - n\phi)} \tag{2.2}$$

where m and n are the poloidal and toroidal mode numbers, respectively. Analysis reveals that an MHD instability with mode numbers m and n can only occur at a flux surface with safety factor $q = m/n$. For standard (monotonic) q profiles this implies that the higher the ratio m/n of a mode is, the closer it will be to the plasma boundary. In toroidal geometry the poloidal symmetry is lost, and for a given n number the poloidal components of various modes can couple. In analogy to (2.2), this can be taken into account with the following ansatz

$$\vec{\xi}(\vec{r}) = e^{-in\phi} \sum_m \vec{\xi}_m(r)e^{im\theta}$$

Several instabilities occur in tokamaks, and they can be detected and studied by measuring the perturbations of the magnetic field, or of local plasma quantities such as the electron temperature and density. If they are not too shortlived, the perturbations become visible in the form of periodic signal oscillations. This is because the instabilities usually rotate, toroidally and/or poloidally, due to the plasma rotation velocity and the diamagnetic drift velocity of the electrons, which is given by

$$\vec{v}_{e,\mathrm{dia}} = \frac{1}{en_eB^2}\nabla p_e \times \vec{B}$$

It can be seen that the diamagnetic drift is proportional to the pressure gradient. Since in tokamaks $B_\phi \gg B_\theta$, it goes predominantly in the poloidal direction. In the plasma core mode rotation is usually dominated by the plasma rotation in the toroidal direction, while the diamagnetic drift only gives a minor contribution and is often neglected in first approximation. At the plasma edge the diamagnetic drift may however give an important contribution to the final mode rotation frequency, particularly in the presence of a steep pressure gradient, and therefore needs to be taken into account.

References

[1] Wesson J A 1997 *Tokamaks* (Clarendon Press: Oxford)

[2] Peeters A G 2000 *Plasma Phys. Control. Fusion* **42** B231

[3] Sauter O and Angioni C 1999 *Phys. Plasmas* **6** 2834

[4] ITER Physics Basis Editors, ITER Physics Expert Group Chairs and Co-Chairs and ITER Joint Central Team and Physics Integration Unit 1999 *Nucl. Fusion* **39** 2137

[5] ITER Technical Basis 2002 ITER EDA Documentation Series 24, IAEA Viena

[6] Freidberg J P 1987 *Ideal Magnetohydrodynamics* (Plenum Press, New York)

Chapter 3

A review of ELM physics

3.1 The high confinement regime H-mode

In the early 80's a high confinement regime was discovered during NBI-heating experiments in divertor tokamak ASDEX [1]. This new regime has been called H-mode (where H stands for "high"). In this regime the confinement time was typically twice that of the low confinement or L-mode. Subsequently, the H-mode regime could be established in many other tokamaks. Over the last 20 years the H-mode has been studied extensively and now is foreseen to become the standard operational scenario for ITER due to its favourable confinement properties.
The change in confinement comes from the formation of a transport barrier for energy and particles at the plasma boundary, leading to the development of a region with steep density and temperature gradients for the electron and ion species in the vicinity of the separatrix, the *pedestal*. The name pedestal originates from the observation that the profiles further inside the plasma are "lifted up" by the transport barrier (in reality, the profiles are not just lifted up; strictly speaking, the shape of the core profiles does also change). The radial extent of the transport barrier is typically of the order of a few cm. Figure 3.1 shows a time sequence of density profiles building up a pedestal, where the time slice 1 gives the L-mode density profile just prior to the L to H transition.
Despite considerable effort, both experimentally and theoretically, the physical origin of the L- to H-transition is not yet understood completely. It is known that sufficient heating (better: power flow across the separatrix) is required for the transition, and that H-mode is much easier to achieve in divertor configurations. In general, the power threshold appears to increase with density, magnetic field and the size of the tokamak, as represented by the empirical law [3]

$$P_{\mathrm{th}} = 0.45 B \bar{n}_e^{0.75} R^2 \quad (\mathrm{MW},\ \mathrm{T},\ 10^{20}\mathrm{m}^{-3},\ \mathrm{m}^2)$$

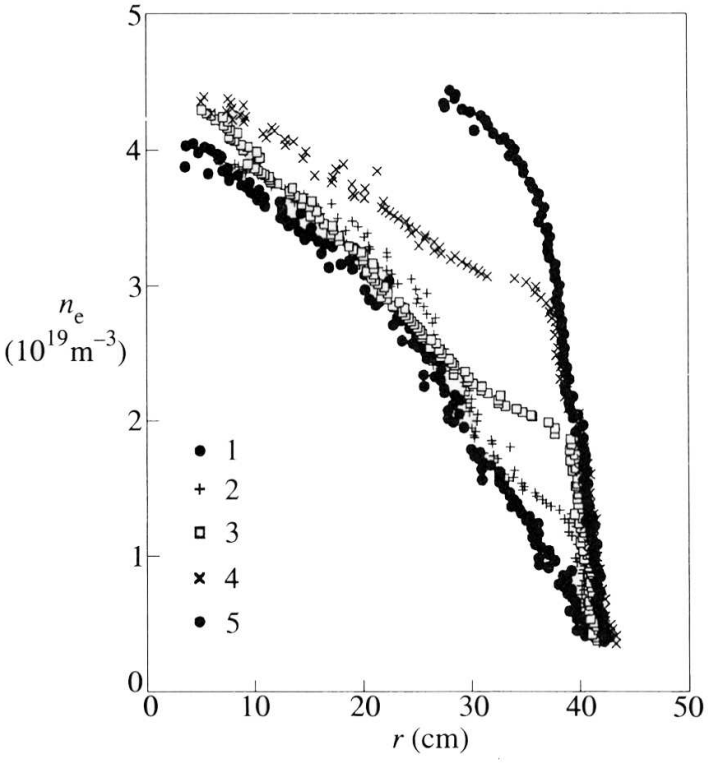

Figure 3.1: Sequence of density profiles measured on ASDEX following the development of a pedestal (from [2]). The first time sequence shows the L-mode density profile just before the L-H transition. The profiles have been measured through reflectometry.

where $\bar{n}_e$ is the line-averaged density. In terms of local edge quantities, there is some evidence for the existence of a critical edge temperature for the L to H transition, which is only weakly dependent on the edge density (figure 3.2). A fairly large number of theories for the H-mode regime exist (a review of these theories can be found in [5]). A widely held view is that the transition originates from the stabilisation of turbulent transport through large rotational shear at the plasma edge.

The discovery of the H-mode was accompanied by the observation of short bursts of a new type of instability localised at the plasma edge, which has been called the Edge Localised Mode, or ELM. The bursts are detected on different diagnostics, including Mirnov coils, electron cyclotron emission (ECE) measurements and soft-X ray cameras, and are also visible as spikes of short duration on the H_α emission. The ELM crash causes a partial breakdown of the pedestal, and leads to a sudden expulsion of energy and particles across the separatrix into the SOL, typically within a few hundred μs or less. While the ELM itself is certainly

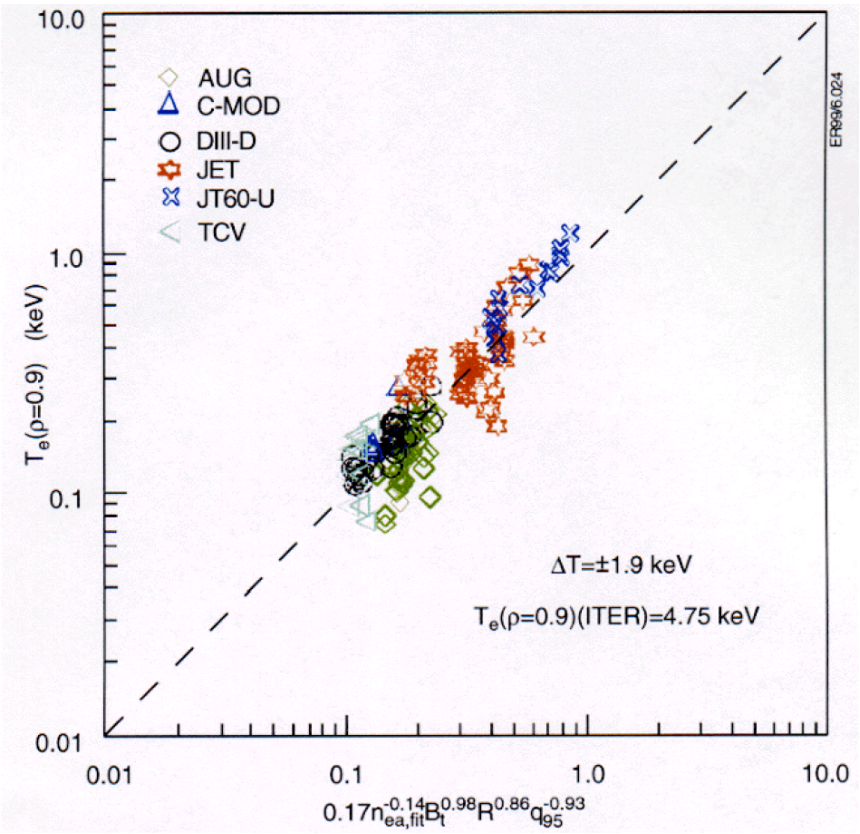

Figure 3.2: Experimental data from six tokamaks comparing the edge electron temperature $T_e(\rho{=}0.9)$, where $\rho = r/a$, to a scaling $T_e = 0.17\bar{n}_e^{-0.14}B^{0.98}R^{0.86}q_{95}^{-0.93}$ (from [4]).

localised at the plasma edge, its consequences are in general not restricted to the plasma boundary but can also extend into the plasma core. The effect of an ELM on the plasma is conceptually depicted in figure 3.3, where the pressure profiles prior to an ELM, and just after an ELM, are shown. Figure 3.4 shows an example of edge density and electron temperature profiles before and after an ELM.

The ELM causes a decrease in the overall energy content W of the plasma, where $W = 3/2 \int p \, \mathrm{d}V$. Assuming that the core profiles remain unaffected, the energy loss caused by the ELM can be approximated as $\Delta W_{\mathrm{ELM}} = 3/2 \, \Delta p_{\mathrm{ped}} \, V$, where p_{ped} denotes the plasma pressure at the top of the pedestal, and V is the total plasma volume. Some of this energy may dissipate in the SOL in the form of radiation, while the remaining part will be deposited on plasma facing components such as the divertor target plates. Thus, ELMs can give rise to transient heat loads of short duration but considerable energy onto the target plates. For present size devices the ELM heat loads do not impose a threat to the

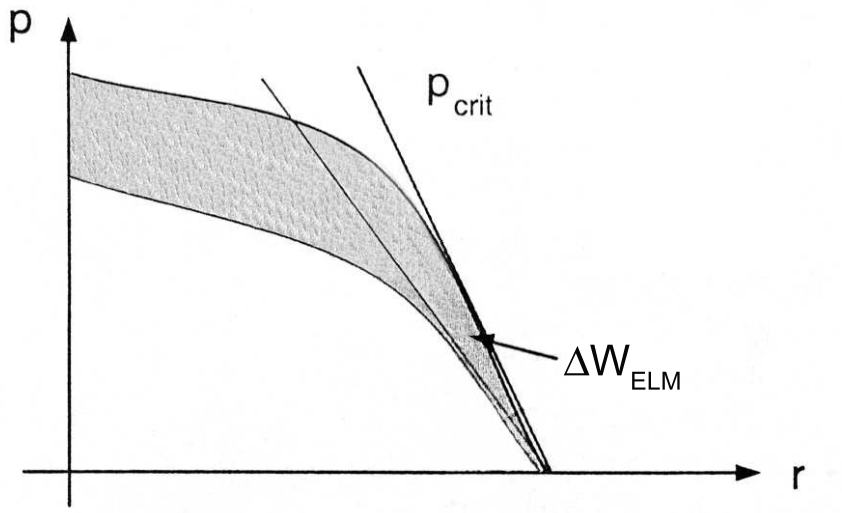

Figure 3.3: Schematical draw of the effect of an ELM crash on the plasma. Shown are pressure profiles prior to an ELM (upper curve), and just after an ELM (lower curve).

divertor. However, when extrapolated to a Next Step Device such as ITER, the heat loads associated with large ELMs are of major concern for the divertor [6,7]. If the ELM deposits enough energy on the target, the surface temperature can rise above the erosion threshold. During each discharge many, maybe thousands, ELMs will occur. If each ELM will exceed the erosion threshold this would result in excessive target erosion and unacceptably short divertor lifetime.

3.2 Classification of ELMs

The standard classification scheme for ELMs was first introduced in DIII-D [9], and subsequently adopted on basically all devices. At least three types of ELMs are known, which are commonly classified as "type-I" (or "giant"), "type-II" (or "grassy") and "type-III" ELMs. In the following the characteristics of the individual ELM types are discussed.

Type-I and type-III ELMs

Figure 3.5 illustrates the evolution of a typical JET discharge when the external heating is switched on. Shown are traces for the applied NBI power (top plot), the electron temperature at the plasma edge (second plot), the line-averaged densities for the plasma core and for the plasma edge (third plot) and the H_α-emission in the inner divertor (bottom plot).
The plasma is initially in L-mode. Soon after switching on the NBI, the plasma

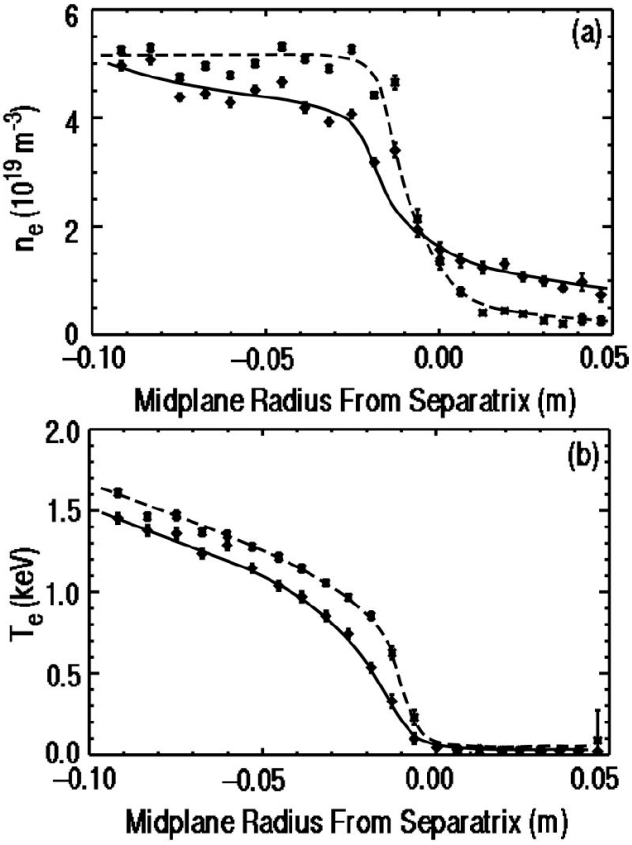

Figure 3.4: Example for (a) edge density and (b) edge electron temperature profiles before and after an ELM (here of type-I) on DIII-D, obtained from Thomson scattering (from [8]).

makes an L to H transition (at 17.39 s), which is recognisable through the step-like increase in the edge temperature. In addition, the rate of increase of the plasma density is seen to become faster after the transition. A characteristic signature of L to H transitions is the observation of a sudden reduction in the level of H_α-emission. In general, the H_α-emission comes from neutral hydrogen entering the plasma as part of the recycling process and so the H_α-signal is a measure of the recycling of hydrogen between the plasma and the surrounding surfaces. Thus, the abrupt fall of the H_α-signal at the L to H transition marks a sudden decrease in recycling.
The L to H transition is followed by a phase with frequent spikes visible on the H_α-signal, which indicate bursts of recycling induced by a loss of particles from the plasma, that lasts until 17.75 s. Those spikes are due to type-III ELMs.
The type-III ELMy H-mode is followed by an ELM-free H-mode phase, which lasts from 17.75-18.65 s. During the ELM-free phase, the plasma is not stationary, and the density increases continuously even in the absence of gas fuelling.

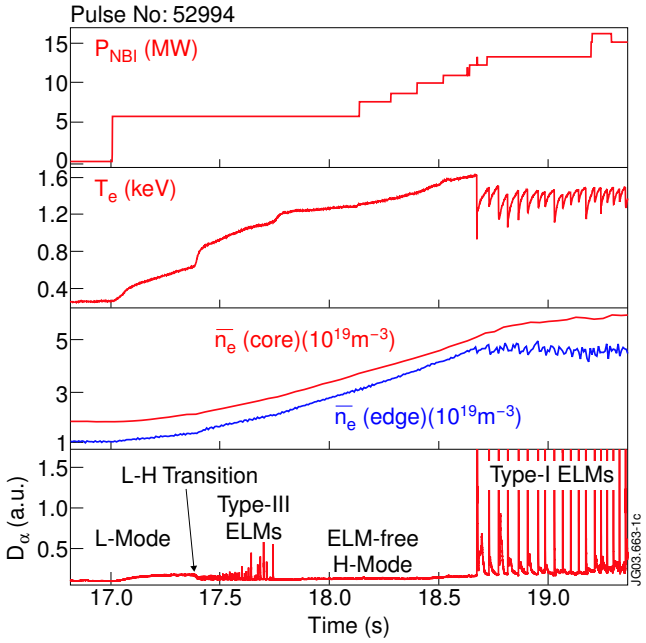

Figure 3.5: JET discharge showing the typical sequence of ELM regimes during the power ramp-up phase. Shown are: the applied NBI power (top plot), the electron temperature at the plasma edge (second plot), the line-averaged electron densities for the plasma core and for the plasma edge (third plot) and the H_α-emission in the inner divertor (bottom plot).

Without further arrangements, the discharge would finally reach its density limit and experience a radiative collapse, a so-called MARFE. (Such a radiative collapse can occur because, when the electron temperature decreases due to an increase in the plasma density, the line-radiation from light impurities is strongly enhanced. This in turn leads to a further cooling of the plasma, again enhancing the radiation until the discharge collapses.)
A further increase in the heating power, however, gives rise to the onset of quite regular spikes of large amplitude visible on the H_α-signal, the type-I ELMs. Coinciding with the H_α-bursts, sharp drops in the edge electron temperature and the edge density trace become visible. After an ELM the plasma gradually recovers until the next ELM occurs. Hence, the quasiperiodic temperature and particle losses associated with the type-I ELMs allows the discharge to become stationary. The type-I ELMy H-mode remains for the whole flat top phase of the discharge, which lasts several seconds, until the heating is finally ramped down (not shown here).
It is found that the ELM frequency behaves differently for type-I and type-III ELMs. The frequency of type-I ELMs increases with increasing energy flux across

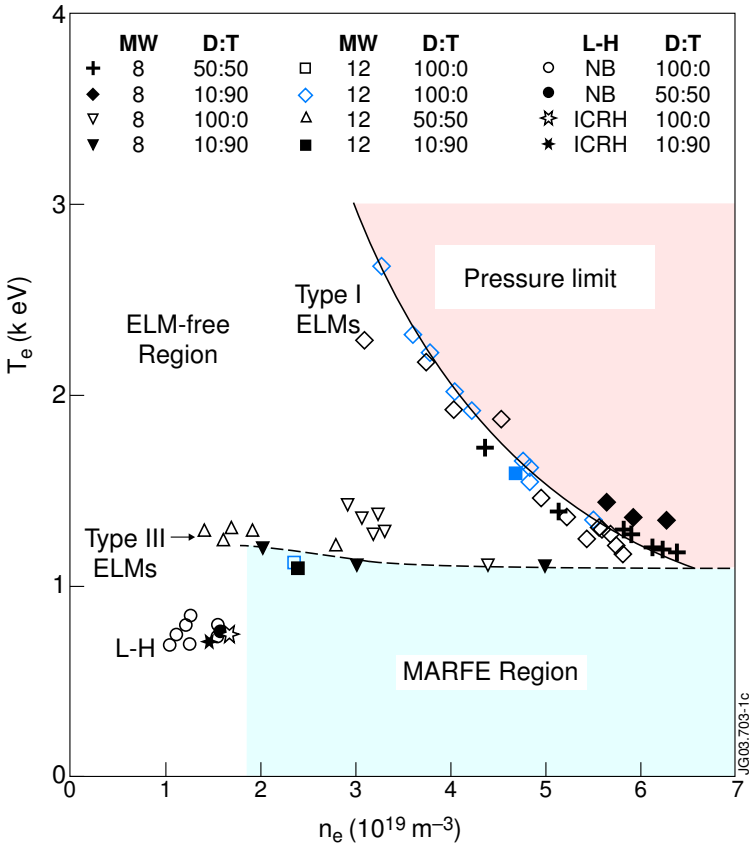

Figure 3.6: Edge operational space for various ELM regimes and the L-H transition for a set of D-T discharges in JET (from [10]). The typical time evolution in this diagramm can be inferred from figure 3.5.

the separatrix into the scrape-off layer (P_{SOL}). P_{SOL} is given by

$$P_{\mathrm{SOL}} = P_{\mathrm{heat}} - P_{\mathrm{rad}} - \mathrm{d}W/\mathrm{d}t$$

where P_{heat} denotes the total heating power, P_{rad} the total power radiated in the bulk plasma, and W the total energy content of the plasma. In contrast to type-I ELMs, the frequency of type-III ELMs decreases with increasing P_{SOL}. In general terms, the ELM frequency tends to be higher for type-III ELMs than for type-I ELMs. The latter criterion is however only of limited applicability for the classification of ELMs, since under certain discharge conditions the frequency of type-I and type-III ELMs may become comparable.
Figure 3.6 shows the operational space in terms of edge density and edge electron temperature for type-I ELMs, type-III ELMs and the L to H transition, here for a set of discharges with various D-T mixtures and two levels of heating (8 and 12 MW) [10]. Such operational studies have been performed on several machines [10–14] yielding similar trends. Type-I ELMs are observed when the

	Type-I	Type-III
f_{ELM} (Hz), typically	∼5-80	∼50-500
With increasing P_{SOL}...	f_{ELM} increases	f_{ELM} decreases
n_e-T_e operational space	near edge pressure limit	slightly above L-H power threshold / at high n_e
$\Delta W_{\mathrm{ELM}}/W_{\mathrm{ped}}$	∼2-20 %	(< 5 %)

Table 3.1: Type-I and type-III ELM characteristics. $\Delta W_{\mathrm{ELM}}/W_{\mathrm{ped}}$ denotes fraction of the pedestal energy content lost due to the ELM. Due to their higher repetition frequency $\Delta W_{\mathrm{ELM}}/W_{\mathrm{ped}}$ is often difficult to measure for type-III ELMs, and hence the number given is to be regarded as an upper limit.

plasma approaches a critical value for the edge pressure p_{crit}, which in itself depends on the particular discharge configuration (magnetic field, plasma current, shaping, etc). Type-III ELMs tend to occur at lower edge pressure. They can be obtained either by low heating power just above the L to H threshold, or, at high heating power, either by increasing n_e through gas puffing, or P_{rad} through impurity seeding. In literature, type-III ELMs are sometimes subclassified into low density type-III ELMs (also called type-IV ELMs on DIII-D) and high density type-III ELMs. The ELM-free regime, which is not stationary, tends to occur at heating powers intermediate between the type-I and type-III ELM regimes. Direct backtransitions from type-I to type-III ELMs can however also be observed, in particular at high density.
Due to the high pedestal pressure, type-I ELMy H-modes exhibit good confinement properties. In particular, type-I ELMs are compatible with good confinement at high density, as is required for a Next Step Device such as ITER. The main drawback are the large transient heat loads onto plasma facing components that are associated with type-I ELMs. Considerable effort has been invested in the assessment of these energy losses (see e.g. [6–8, 15–23]). While there is still some uncertainty in their extrapolation to a larger device, it seems likely that type-I ELMs will be unacceptable for ITER operation and hence will have to be avoided. Type-III ELM scenarios have more benign energy losses, but at the expense of a confinement degradation and hence a lower plasma performance (see e.g. [24]).
A brief overview of the various features of type-I and type-III ELMs is given in table 3.1.

Type-II ELMs

So far we have not considered the so-called type-II, or "grassy", ELMs. While ELMs of type-I and type-III have been robustly established on all large tokamaks,

type-II ELMs are much more difficult to achieve. Type-II ELMs provide small but frequent energy losses at high confinement, while maintaining the energy and particle exhaust across the edge transport barrier required for stationary operation. It appears that these modes only occur in a rather narrow operational window, whose exploration is currently subject of intense research.

The first observation of a transition from type-I to small ELMs at high plasma confinement was reported by DIII-D in 1990 [25]. In that experiment, the suppression of type-I ELMs was achieved by a simultaneous increase of the plasma elongation ($\kappa > 1.8$) and triangularity ($\delta > 0.4$), at high edge safety factor ($q_{95} \sim 7$). The identification of these small ELMs as a new type was put forward by the DIII-D team [26].

More recently, high confinement regimes with small ELMs were also found in JT-60U [27–29]. Type-I ELMs disappear and minute grassy ELMs appear if the triangularity δ, the edge safety factor q_{95} and β_p are high enough [28]. Complete suppression of type-I ELMs was observed at $\delta \gtrsim 0.45$, $q_{95} \gtrsim 6$ and $\beta_p \gtrsim 1.6$ [28], or alternatively at $\delta \gtrsim 0.58$ and $q_{95} \gtrsim 3.8$ [29]. The threshold for δ decreases if q_{95} is increased, and vice versa. The rather irregular H_α pattern is dominated by repetition frequencies of about 0.5 kHz. In contrast to the case of DIII-D (Ref. [25]), δ and κ could be varied independently, and δ turned out to be the relevant parameter to reach the grassy ELM regime [27].

A type-II ELM regime was also discovered on ASDEX Upgrade [30]. Here, steady-state pure type-II ELMy H-mode phases are only obtained at high densities. This is in contrast to JT-60U. Additional requirements are $q_{95} \geq 4.2$, and an equilibrium close to a double-null configuration with an average triangularity $\delta = 0.40$. The results of ASDEX Upgrade raise the question whether it is the closeness to double-null configuration rather than the plasma triangularity, which determines the transition to type-II ELMs. In phases with type-II ELMs a characteristic magnetic broadband fluctuation in the frequency range 30 ± 10 kHz can be observed on magnetic pick-up coils. The type-II ELM repetition frequencies are in the order of 0.5 to 1 kHz. Recently, mixed type-I/type-II ELM phases have been obtained in ASDEX Upgrade for $3.6 \lesssim q_{95} \lesssim 4$ in high power plasmas at high β_p [31].

In JET, a pure type-II ELM regime could not be established so far. However, an anomalous decrease in the type-I ELM frequency could be observed at high pedestal densities (high gas fuelling) in high triangularity discharges ($\delta \sim 0.45 - 0.5$) [32]. The observed reduction of f_{ELM} with density is accompanied by increased activity on the H_α emission in the form of small and irregular fluctuations, and by a characteristic enhancement of MHD fluctuations in the frequency range 10-30 kHz observed with magnetic pick-up coils. The similarity of these observations with the ones reported in ASDEX Upgrade [30], suggests that this regime at JET is a mixed type-I/type-II ELM regime. One difference between the ASDEX Upgrade and JET operational conditions in type-II

(or mixed) ELMs is the value of the edge safety factor, which is lower at JET ($q_{95} \sim 3$) than in ASDEX Upgrade. So far, attempts to establish on JET a pure type-II ELM regime through an increase of q_{95} or β_p, or through variation of the closeness of the plasma shape to double-null configuration, have not been successful [33]. There is some evidence that the access from type-I to mixed type-I/type-II ELM regime could be easier with higher input power [34], but this still requires confirmation.
Since type-II ELMs lead to a much more steady heat flux to the divertor than type-I ELMs, with significantly reduced peak loads, and provide stationary high confinement, they constitute a very attractive candidate scenario for ITER. However, as the access to type-II ELMs is not straightforward, they are still relatively unexplored. For instance, no characterisation exists for the power dependence of the type-II ELM frequencies, in contrast to type-I and type-III ELMs. Although there are similarities, it is even not completely clear yet whether the small ELM regimes identified on the various devices, and which share the common label "type-II" or "grassy", really originate from the same phenomenon.

Further regimes

A somewhat special case is the so-called Enhanced D_α (or EDA) regime of the Alcator C-Mod tokamak [35, 36], which is a high magnetic field device ($B \sim$ 5-8 T). The EDA regime is a stationary regime, which is free of type-I and type-III ELMs, found at moderate to high densities. It has good energy confinement and is characterised by a high level of continuous D_α emission. EDA plasmas require a moderate pedestal temperature ($T_e \lesssim 400$ eV) [37] and are more likely at low plasma current ($q_{95} > 3.7$), medium to high triangularity ($\sim$ 0.35-0.55) and high neutral pressures. The EDA regime appears to be maintained by a continuous mode in the steep edge gradient region that has been called the quasi-coherent mode (QCM) [38]. The QCM is believed to cause an enhanced particle transport across the edge barrier and thus allow for stationarity. Since on Alcator C-Mod no type-I ELMs have been observed so far, most probably due to a lack of heating power [39], the classification of the EDA regime in the context of the type-II ELM regimes discussed above is difficult. The analysis on the basis of intermachine comparisons is not yet conclusive, but at present a widely held view is that the EDA mode of Alcator C-Mod is not related to type-II ELMs but constitutes an operational regime of its own. So far the EDA regime could not be reproduced in other devices.
Another operating regime is the quiescent H-mode (QH-mode) regime, first seen in DIII-D [40–42] and recently also achieved in ASDEX Upgrade [43]. Three key factors are required for this regime: neutral beam injection in a toroidal direction opposite to that of plasma current (counter-injection), a large clearance between the separatrix and the wall, and good pumping conditions achieved by locating

the divertor strike points near the divertor cryopump entrance. The QH-mode is ELM-free and yet has stationary (low) density. The density control seems to be possible due to the presence of an edge MHD instability, which has been called the edge harmonic oscillation, or EHO, that appears to enhance the edge particle transport while leaving the energy transport unaffected. There has been recent success in DIII-D to achieve higher plasma densities while maintaining the QH-mode edge [44]. A still unsolved problem of QH-mode discharges is their rather high impurity content (Z_{eff}) [45]. The impurities dilute the primary fuel ions, thus reducing the neutron production rates. The achievement of a low Z_{eff} is clearly a necessary condition before the QH-regime can be considered reactor-relevant.

Overview

One may summarise the above considerations as follows:

1. Standard *ELM-free H-mode* plasmas show no ELMs and, linked to this, low edge transport. This yields good energy and particle confinement but also an impurity exhaust problem. Consequently, ELM-free H-modes are not stationary.

2. Plasmas with *type-I ELMs* show more or less strong relaxation oscillations with low repetition frequency and have sufficiently low edge transport. This scenario is a good compromise between high confinement and sufficient particle exhaust. The main problem are the unacceptably high transient heat loads expected in the divertor of a burning fusion plasma.

3. Plasmas with *type-III ELMs* show relaxation oscillations with high repetition frequency, sufficient particle exhaust and tolerable transient heat loads. The main disadvantage is the rather high overall energy transport, leading to a degradation of the energy confinement of the plasma.

4. *Type-II ELMs* show relaxation oscillations with high repetition frequency, sufficient particle exhaust and tolerable transient heat loads. In contrast to type-III ELMs, they also provide good energy confinement. They appear to occur only in a narrow operational window, and it is still unclear whether type-II ELMs will be possible to achieve in a burning fusion plasma.

The basic question is whether a good compromise can be found between sufficient particle exhaust, low enough energy transport and tolerable transient heat loads in a burning fusion plasma.

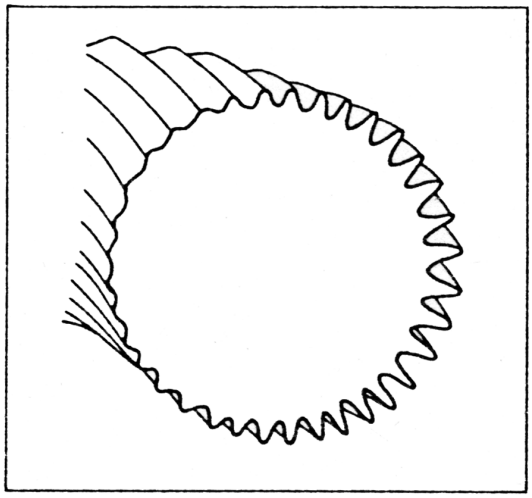

Figure 3.7: Ballooning mode displacement (from [46]).

3.3 Theory of ELMs

ELMs are not well understood yet. Ideal MHD modes driven by the steep current and pressure gradients at the edge transport barrier are regarded as the most likely candidates to explain their origin. This applies in particular to type-I ELMs, to which the majority of the theoretical work done so far was devoted. For type-III ELMs, resistive modes are also considered to be a strong contender. From stability calculations performed on the basis of experimental data three types of ideal MHD instabilities can be expected at the transport barrier: kink-/peeling-modes, ballooning modes and coupled peeling-ballooning modes. Over the last two decades considerable theoretical work has been performed, both analytically and through modelling calculations, to improve their theoretical background. In the following a brief description of the three above mentioned instabilities is given.

3.3.1 Ballooning modes

Ballooning instabilities are driven by the pressure gradient. This type of instability arises from the toroidicity, in other words, it does not occur in a straight cylinder geometry. In general, the magnetic field has a favourable curvature with respect to field line bending by the pressure gradient on the inner side of the torus, and an unfavourable curvature on the outer side. Ballooning modes develop as a localised instability on the outboard (low field) side of the plasma. At sufficiently high pressures structures can eventually develop which "balloon" towards the low field side such that the field lines are bent radially outwards (figure 3.7).

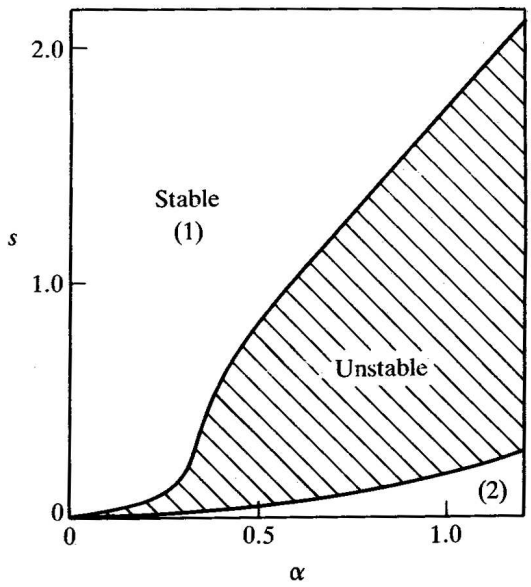

Figure 3.8: Marginal stability diagram for ideal infinite-n ballooning modes, calculated numerically for circular flux surfaces and $a/R \ll 1$, showing the regions of first (1) and second (2) ballooning stability (from [47]).

In literature, the ballooning stability is often characterised by the so-called ballooning stability parameter α, defined as

$$\alpha = -\frac{2\mu_0 R q^2}{B^2}\frac{\mathrm{d}p}{\mathrm{d}r}$$

Ballooning stability also depends on the magnetic shear s, which has (in the first stability region, see below) a stabilising effect. This is because the shear of magnetic field lines opposes the movement of the fingers radially outwards across the flux surfaces. Since s varies with the plasma shape, ballooning stability can therefore be influenced by quantities such as the plasma triangularity and elongation.
A stability diagram for ballooning modes in s-α space is shown in figure 3.8. The two solid curves represent the marginal stability boundaries, as a function of shear and α, computed numerically for the case of circular flux surfaces in the limit $a/R \ll 1$. One branch separates the "first region of stability" from the unstable region. At a fixed value of shear the system is stable for small pressure gradients. As the pressure gradient (i.e. α) increases the perturbation develops a progressively larger ballooning component. At sufficiently high α, the destabilising contribution from the unfavourable curvature region overcomes the stabilising influence of the magnetic shear, and the system becomes unstable. As expected, when the shear increases, the maximum stable pressure gradient also increases.

A somewhat surprising feature of the s-α diagram is the so-called "second region of stability". In this region sufficiently large values of the pressure gradient are stabilised. Interestingly, this region is most easily accessible at low values of magnetic shear. In the proximity of the second stable region magnetic shear becomes destabilizing for ballooning modes. The origin of the second stable region for ballooning modes is hidden in the ballooning mode equations, and not easy to justify in an intuitive manner. It turns out that it is related to the variation of the local value of the magnetic shear along a flux surface (due to toroidicity, the local shear has different values on the low and high field side). Effectively, the second region of stability is generated by a pressure-driven modification of the local shear. Since this local shear modulation increases with the poloidal beta, β_p, access to second stability is predicted to be easier to achieve in high β_p plasmas.
With increasing mode numbers ballooning modes become more and more unstable. In fact, within ideal MHD, infinite-n ballooning modes are the most unstable ballooning modes. However, inclusion of correction terms in the ideal MHD equations which are related to the finite size of Larmor orbits (so called finite Larmor radius, or FLR, effects, also referred to in literature as diamagnetic stabilisation effects) will impose an upper limit on the most unstable mode numbers.
The theory of ballooning modes is rather involved and still in the process of development. In the following a brief overview of past theoretical work is given.

Core and edge ballooning modes

The standard analytical expressions for conventional (internal) ballooning mode theory were published in 1978 [48]. Starting from the ideal MHD equations, the derivation makes use of an expansion in the small quantity $1/\sqrt{n}$. The stability boundaries are then computed in the limit $n \to \infty$. At finite n, conventional ballooning theory predicts a $1/\sqrt{n}$ dependence of the ballooning mode width and a finite-n correction of the critical α proportional to $1/n$ [49].
It turns out that some details in this derivation are not applicable to the plasma edge. A modified ballooning formalism, which is valid at the plasma edge, has been developed only rather recently [50]. The analytic calculations show that the edge ballooning mode has the same infinite-n stability boundary as that predicted by the conventional ballooning equation (when the coupling to the peeling mode is not important, see also section 3.3.3). The analytic calculations further predict that the edge ballooning mode has a larger, stabilizing, finite-n correction, proportional to $n^{-2/3}$, than conventional ballooning theory would predict

$$\alpha_{\mathrm{crit}}(n) - \alpha_{\mathrm{crit}}(\infty) \propto \frac{1}{n^{2/3}}$$

and a mode width that scales with $n^{-2/3}$. Furthermore, the analytic expressions predict the individual poloidal Fourier harmonics to be coupled and have an envelope with the shape of an Airy function, while conventional ballooning theory would predict a Gaussian envelope.
Detailed modelling computations performed by Huysmans *et al* [51] with the ideal MHD code MISHKA [52] have however refuted some of the features predicted in the analytic treatment of edge ballooning modes. It turns out that the value of the marginally stable pressure gradient can be well described by

$$\alpha_{\mathrm{crit}}(n) = \alpha_{\mathrm{crit}}(\infty) + \frac{c_\alpha}{n\Delta_{\mathrm{ped}}}$$

where Δ_{ped} is the width of the transport barrier and c_α is a constant. The $1/n$ correction is consistent with the conventional ballooning theory, and does not agree with the modified scaling with $n^{-2/3}$ as found in [50] (the reasons for this are further discussed in [51]). The correction is inversely proportional to the width of the edge pedestal i.e. a narrow barrier is more stable to lower toroidal mode numbers than a wide barrier. The width of the ballooning mode in the edge pedestal does not follow the $1/\sqrt{n}$ dependence expected from the conventional ballooning theory, nor the scaling for edge ballooning modes $n^{-2/3}$ [50]. Instead, the width shows a strong scaling with the pedestal width and a weak dependence on the toroidal mode number. The half-width of the ballooning mode can be approximated by $\Delta_{\mathrm{ball}} \sim \Delta_{\mathrm{ped}}^{3/4} n^{-1/4}$. The mode width basically fills up the width of the pedestal.

Finite Larmor radius effects

As mentioned above, finite Larmor radius (FLR) effects, not considered in standard ideal MHD, affect the ballooning stability. The stabilizing influence of a radially constant ion-diamagnetic drift frequency, ω_i^*, on ballooning modes was first demonstrated in [53] for a simple model toroidal equilibrium (and later extended to more general equilibria in [54]). Figure 3.9 illustrates the effect of the diamagnetic stabilisation on the marginal stability boundaries for ballooning modes. The effects of a constant ion diamagnetic drift and the finite radial localization of the pedestal pressure gradient were studied in [55] using the Braginskii equations and a simple analytical model. The effect is found to be strongly stabilizing when $\Delta_{\mathrm{ped}} < \Delta_R$, where $\Delta_R \sim \rho_i^{2/3} R^{1/3}$ in the center of the pedestal. In this limit, conventional ballooning modes within the pedestal region become stable, and a stability condition is obtained, $\alpha/\alpha_c < (4/3)\Delta_R/\Delta_{\mathrm{ped}}$, which is much less stringent than that predicted by local magnetohydrodynamic theory ($\alpha/\alpha_c < 1$).
While treating ω_i^* as a constant is normally a reasonable assumption, it often fails in the pedestal region where the density and temperature vary strongly over short distances. The formalism was extended in [56] to retain the strong radial

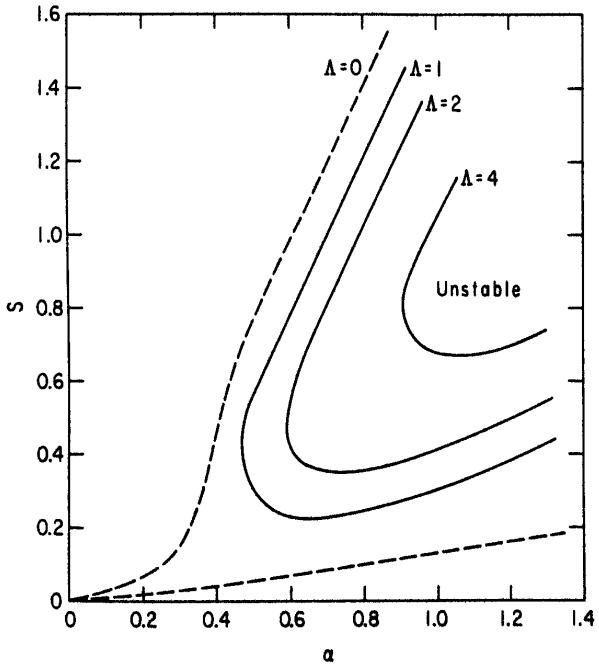

Figure 3.9: Marginal stability boundaries for ballooning modes in s-α space, as a function of the finite gyroradius parameter $\Lambda \equiv n^2\rho_i^2 q^2 R/(2r^2 L_p)$, where $L_p = |\mathrm{d}(\ln p)/\mathrm{d}r|^{-1}$ denotes the scale length of the pressure gradient. $\Lambda = 0$ corresponds to the case with no diamagnetic stabilisation (from [53]).

variation of ω_i^* characteristic of edge plasmas in the pedestal region. As a consequence, the FLR stabilization is modified and can be weaker than in the case of constant diamagnetic frequency.
Extensive numerical computations have been performed by Huysmans *et al* [51] with a modified version of the MISHKA-1 code, MISHKA-D, that accomodates FLR effects in general axi-symmetric toroidal geometry. The stabilisation of ballooning modes due to FLR effects is strongest for narrow pedestals. For a low enough density, where the effect of the ion-diamagnetic drift is largest, the ω_i^* stabilisation can lead to a second stable regime with all ballooning modes stable for any value of the pressure gradient. The calculations also confirm that a strong radial variation of ω_i^* reduces the efficiency of diamagnetic stabilisation, and that no complete stabilisation is found if ω_i^* varies too much [57].

Finite edge current

Due to the strong temperature and density gradients encountered at the transport barrier the bootstrap current density needs also to be considered. The finite edge current plays an important role in the ballooning stability, because it re-

duces the magnetic shear. Miller *et al* [58] found that the edge pressure gradient (H-mode pedestal) for computed equilibria in which the current density profile is consistent with the bootstrap current may not be limited by the first-regime ballooning limit. According to [58], the transition to second stability is easier for higher plasma elongation, intermediate triangularity, narrower pedestal width, higher q_{95} and lower collisionality. The inclusion of the current in studies of the pedestal leads to a separate dependence of MHD stability (i.e. also ballooning modes) on density and temperature, rather than just pressure, because of the strong dependence of the bootstrap current on the collisionality ν_e (as mentioned earlier, $\nu_e \propto n_e/T_e^2$) [59].

Further effects to be considered

Despite the extensive work of recent years, linear ballooning theory is still incomplete. In addition to the effects discussed above, there are at least two further effects that are likely to have an impact on ballooning stability and have not been accounted for so far: the strong rotational shear that is expected at the plasma edge, and the effect of a poloidal field null and the associated singularity of the safety factor q when approaching the separatrix.

Nonlinear ballooning theory

Although at an early stage of development, inclusion of nonlinear effects in ballooning theory has already highlighted some interesting features, which may have relevance beyond the field of fusion research. Nonlinear ballooning is currently being regarded as a possible candidate to explain the sudden loss of confinement that occurs in solar flares, tokamak disruptions and ELMs [60], among other phenomena. The theory predicts a general explosive feature of the ideal ballooning instability ("detonation") emerging from non-linear effects through the development of tube-like structures, the ballooning fingers. In the case of ELMs, the ballooning fingers depart from inside the separatrix and move outwards into the SOL (see figure 3.10).
The theory of nonlinear ballooning modes has been developed in a series of papers. The basic nonlinear mechanisms were first investigated in a plasma slab with gravity with the field lines tied to conducting walls [61]. Later on, this analysis was generalised to three-dimensional geometry [62] with line-tied boundary conditions (the displacement is zero at the end of the field lines), including the effects of magnetic shear and curvature. The analysis in [61,62] used ideal MHD equations—Fong *et al* [63, 64] included finite Larmor radius terms and showed that this effect determined the width of the fingers in tokamak disruptions. Very recently, the analysis has been extended to toroidal plasmas [65], relaxing the line-tied boundary conditions.

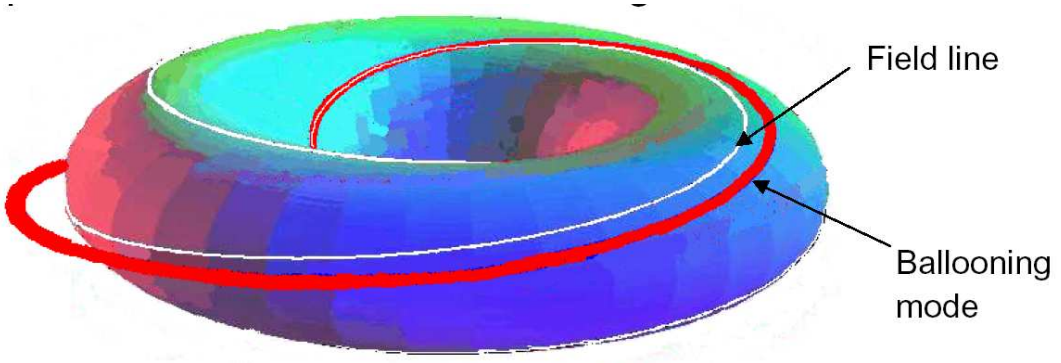

Figure 3.10: Cartoon of field lines in nonlinear ballooning. The ballooning red flux tube (field line) has been displaced from the white line on the surface. The displacement is large on the outside of the surface (from [60]).

3.3.2 External kinks and peeling modes

The external kink mode is generally considered to be a current-driven mode. The theory of kink modes has not been developed in divertor geometry, where the edge safety factor becomes infinity at the separatrix. The theory assumes that at the plasma boundary q has a finite value, q_{edge}, and that further rational surfaces are present outside the plasma in the vacuum region. External kink modes become destabilised when the safety factor at the plasma edge, q_{edge}, is low enough such that a mode with $m/n > q_{\text{edge}}$ (where m and n are the poloidal and toroidal mode numbers, respectively) can be destabilised. External kinks are normally dominated by a single helicity m/n (in contrast to the ballooning modes, for which each toroidal component is usually composed of a large number of poloidal components with comparable amplitude).
It becomes clear that the kink mode's rational surface is located in the vacuum region outside the plasma. The instability is sensitive to the distance of the rational surface to the plasma. In particular, when the rational surface is very close to the plasma (e.g. $m/n = 3$ and $q_{\text{edge}} = 2.95$), the resulting instability is strongly localised near the plasma edge and has a large growth rate. In literature this particular type of external kink is often termed as the "peeling mode". As q_{edge} is reduced the instability has a greater radial extent, and the growth rate decreases until q_{edge} crosses the next rational value where a peeling mode reappears. Figure 3.11 illustrates the poloidal mode structure of an $n = 1$ kink (peeling) mode, and the displacement profile associated with the mode as a function of radius.
In theory, external kinks should be stable in plasmas with divertor configuration, since $q = \infty$ at the separatrix, and hence all rational surfaces are located inside the plasma. However, it turns out that for practical considerations the plasma boundary can be effectively set (somewhat arbitrarily) at a finite value of q near

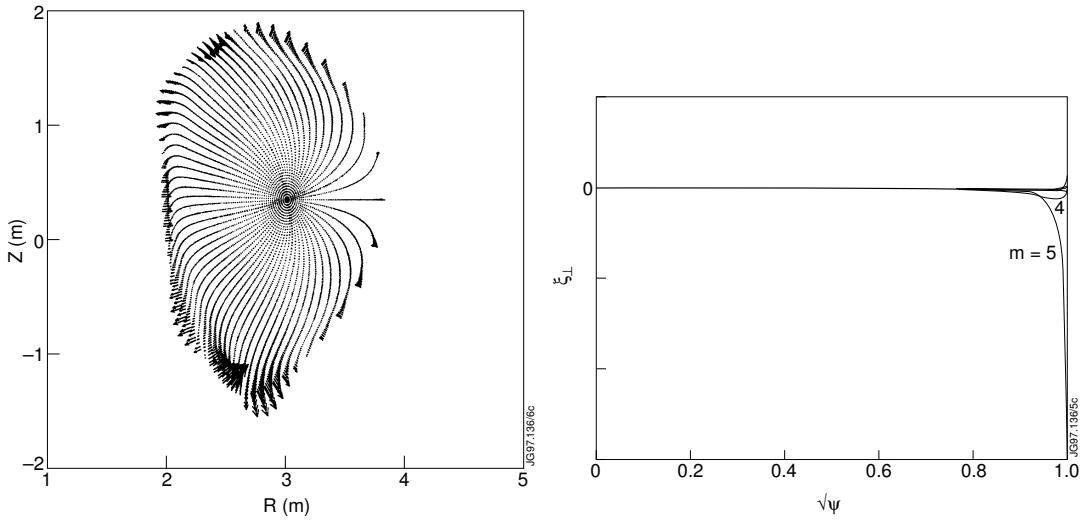

Figure 3.11: (a) Mode structure of an $n = 1$ external kink mode, where the perpendicular component of the displacement vector of the perturbation is shown in the poloidal plane. (b) Radial displacements of the individual Fourier harmonics for the same mode, as a function of the radial coordinate $\sqrt{\psi}$ (where ψ is the normalised poloidal magnetic flux corresponding to each flux surface).

the plasma edge (e.g. q_{95} or q_{99}) due to finite resistivity effects. External kinks could indeed be unambiguously identified experimentally in divertor plasmas in JET [66], thus supporting the above approach.
In the following a brief overview of past theoretical work on kink modes is given. The basic paper for (general) kink stability in tokamaks was published by Shafranov back in 1970 [67]. The standard analytical expressions for the particular case of peeling modes have been published later on by Lortz in 1975 [68]. Starting from the ideal MHD equations, an expansion is made in powers of the (small) distance of the mode's rational surface to the plasma boundary. A summary of further results on kink stability for a range of cases is given in [69]. Results from modelling computations on kink stability with the PEST code [70] in circular geometry and with L-mode profiles (i.e. no pedestal) are given in [71]. The stability to the external kink mode is shown to depend on the details of the current density near the plasma edge, in addition to $q_{\rm edge}$. In particular, the build-up of the current density near the plasma edge is shown to decrease the magnetic shear and lead to a destablilization of the kink mode. Later, Huysmans et al [72] explored the influence of combined edge currents (mainly the bootstrap current) and pressure gradients on the stability of low-n external kink modes in real JET geometry and taking into account the steep pedestal gradients of the H-mode transport barrier. For the analysis the codes CASTOR [73, 74], HELENA [75] and JETTO [76] were used. The results confirmed the destabilising role of a

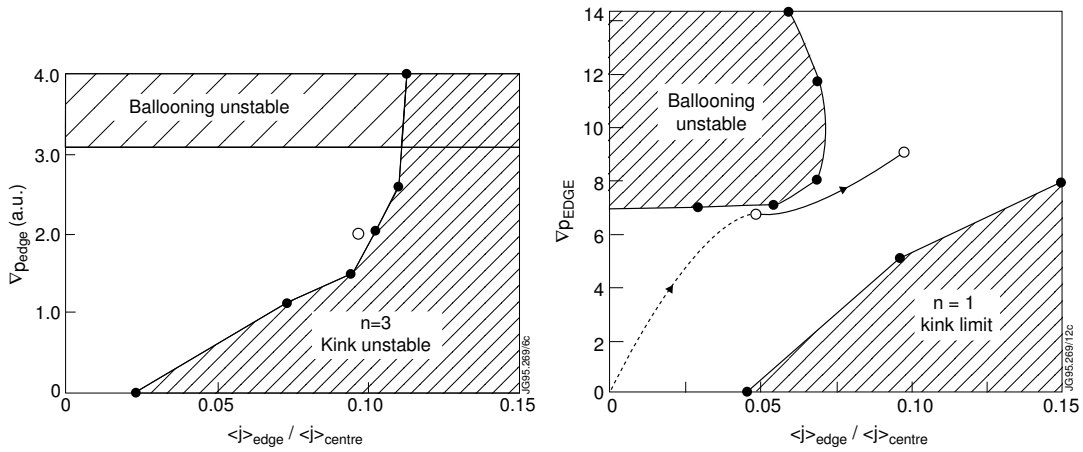

Figure 3.12: (a) The stability diagram for JET discharge 30591 at $t = 12.2$ s, for $n = 3$ kink modes and infinite-n ballooning modes, in the plane of edge current density and edge pressure gradient. (b) Stability diagram for the high β_p JET discharge 32344 at 12.25 s for $n = 3$ kink modes and infinite-n ballooning modes. In contrast to (a), access to the second stable regime for ballooning modes (in the upper right corner of the plot) is possible here. The ballooning mode stability is evaluated at the flux surface which encloses 95% of the poloidal magnetic flux. The open circles indicate the edge pressure gradient and edge current density evolution of the discharge from the JETTO simulation (from [72]).

finite edge current density, and established an operating diagram in j_{edge} and ∇p_{edge} (an often used alternative to s-α diagrams) for low-n external kinks and ballooning modes (see figure 3.12).

3.3.3 Coupled peeling-ballooning modes

The toroidicity of axisymmetric systems such as the tokamak, and shaping effects associated with ellipticity, triangularity, etc., have the effect of coupling poloidal Fourier harmonics with the same toroidal mode number. The coupling to finite-n ballooning modes is neglected in the original analytic formula used for peeling modes [68]. The theoretical framework for the analysis of coupling effects on peeling and ballooning modes has been developed in [77, 78] and applied to a simplified model, which was later on extended in [50]. The calculations show that the toroidal coupling plays a destabilizing role, and that the peeling mode, normally dominated by a single poloidal Fourier harmonic associated with the first rational surface outside the plasma, can drive several "sideband" harmonics in the plasma edge region.
The effect of the coupling is illustrated in figure 3.13, which shows the marginal stability boundaries in j-α space including the coupling of peeling and ballooning

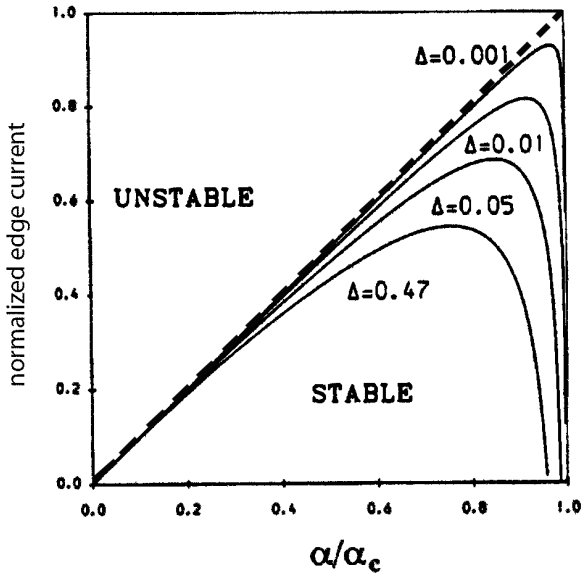

Figure 3.13: Typical behaviour of the marginal stability boundaries in j-α space (here calculated for a model equilibrium) with coupling of peeling and ballooning modes (solid curves), as a function of the parameter $\Delta \equiv -n(\mathrm{d}q/\mathrm{d}r)|_{r=a}(a - r_0)$, where a is the minor radius of the plasma boundary, and r_0 is the radius of the peeling mode rational surface. Δ increases with the distance of the peeling mode rational surface to the plasma boundary. The dashed line represents the peeling mode stability threshold. The ideal ballooning threshold is given by $\alpha/\alpha_c = 1$, a vertical line in this plot (from [78]).

modes. As the stability threshold of either the ballooning mode or the external kink mode is approached, the interaction effect becomes more prominent. It is possible for the coupled ballooning kink-instability to be unstable when the pure ballooning and pure kink modes are independently stable. Subsequently also some numerical studies on coupled peeling-ballooning stability have been done [57, 59, 79–81]. The coupled peeling-ballooning modes are driven by both the pressure gradient and the edge current density.
The implications of peeling-ballooning coupling on the access to the second stable regime for ballooning modes have been numerically studied in [80] with the ELITE code [81] (see figure 3.14). It is shown that access to second stability depends on a so-called magnetic well factor d_M, which is related to the average curvature of a magnetic flux surface and describes the effects of shaping and finite aspect ratio (since d_M is a rather complicated function, and is not further needed here, its exakt definition is not given; the exakt definition can be found e.g. in [46], page 73). In the $n \to \infty$ limit, the peeling and ballooning thresholds can both be obtained from simple 1-D calculations, and these are shown in

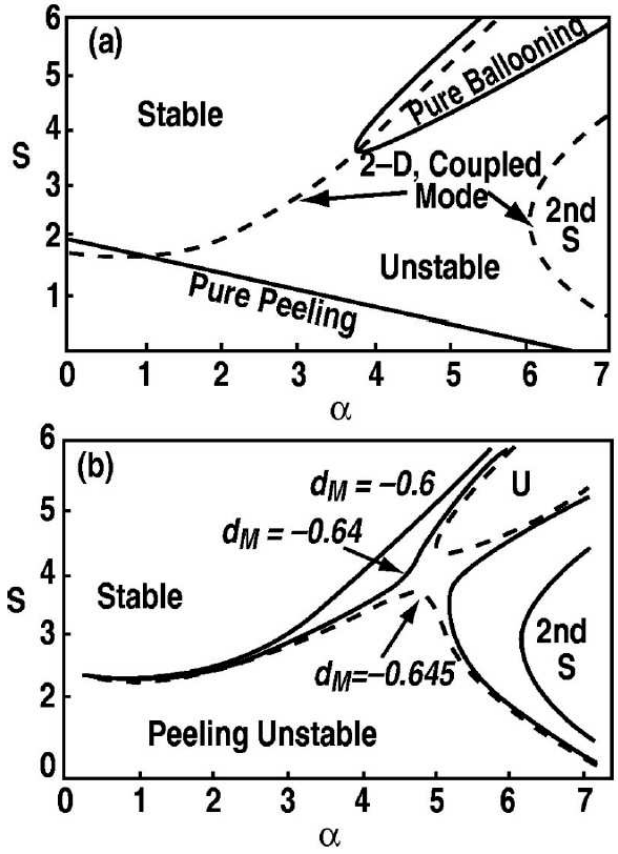

Figure 3.14: (a) The marginal stability contours in s-α space for the $n = \infty$ pure peeling mode and the $n = \infty$ pure ballooning mode (solid curves), and for the coupled peeling-ballooning mode (dashed line, here for $n = 20$ and $d_M = -0.6$) (b) A sequence of curves for the $n = 20$ coupled mode, with $d_M = -0.6, -0.64, -0.645$, showing second access reopening at the deepest well ($d_M = -0.645$) (from [80]).

figure 3.14(a). Note that a wide stable path to the second stability region exists between the pure peeling and the pure ballooning unstable regions. However, at finite values of n, the peeling and ballooning modes couple and can close access to the second stability region. Increasing the magnitude of the magnetic well (i.e. increasing shaping) decouples the modes and reopens again the access to second stability. This is shown in figure 3.14(b). The strength of the peeling ballooning mode coupling is a function of n, and the second stability gap opens more easily for higher n modes.

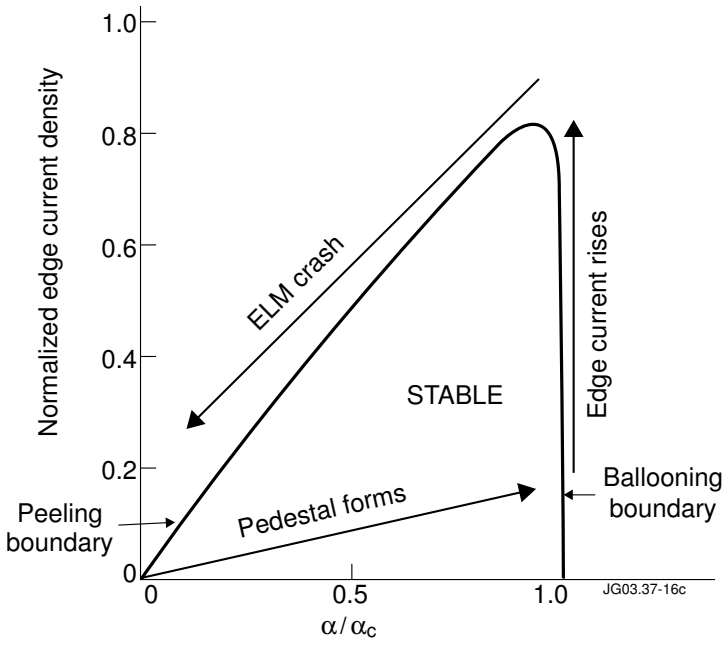

Figure 3.15: Stability diagram for coupled peeling-ballooning modes in the space of normalised edge current and ballooning stability parameter showing the order of events predicted by the peeling-ballooning cycle originally proposed in [50].

3.3.4 ELM cycles

The above theoretical considerations have led to the proposition by Connor *et al* [50] of a model for type-I ELMs, the so-called peeling ballooning cycle, that has gained wide acceptance. The order of events predicted by this cycle is conceptually depicted in figure 3.15. Just after the previous ELM crash the plasma edge resides in a state of low pressure and low edge current (lower left corner in diagram). Heating builds up the pedestal pressure gradient on a relatively fast time scale until the ideal ballooning limit is reached, where, according to the model, the pressure gradient is kept constant. Here, the model assumes that the ideal ballooning instability is a benign instability that does not induce a violent event but rather limits the pressure gradient in a smooth way. In a further step, with the edge current gradually building up on a slower (resistive) timescale, the pedestal state moves towards the upper right corner of the stability diagram. The ELM is finally triggered when the peeling stability boundary is crossed, where the onset of peeling (or coupled peeling-ballooning) modes causes a degradation of confinement and therefore a further destabilisation of the modes.
A qualitative modification of the peeling-balloning cycle model to include further types of ELMs has been recently proposed by *Snyder et al* [59]. Within that model, the various ELM-types are described by cycles with alternative tra-

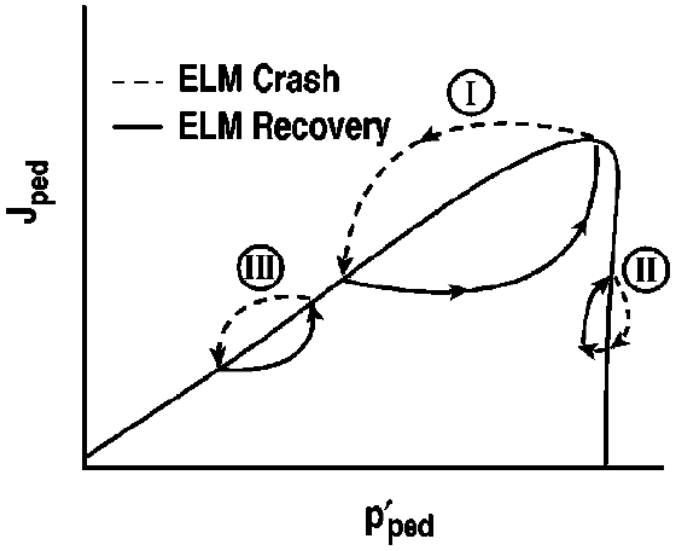

Figure 3.16: ELM cycles proposed in [59] for various types of ELMs.

jectories in the edge current/edge pressure stability diagram. The model also postulates that ELM size correlates with the radial depth of the most unstable mode.

Figure 3.16 illustrates the model conceptually. The cycle labeled "III" will occur at low density and low input power, such that the current rises to exceed the peeling limit well before the pressure gradient reaches the ballooning limit. These ELMs are expected to be small, both because the peeling modes triggering them have narrow mode structures, and because they occur at low pedestal height. The ELM frequency is expected to decrease with input power, because the pressure gradient will rise more quickly, stabilizing the peeling mode. This cycle provides a model for the low density type-III ELMs. High density type-III ELMs are likely driven by resistive modes, and have thus not been included by this model.

At higher power and low density, cycle "I" will occur, generating large ELMs both because the relatively low-n peeling-ballooning modes have a broad radial structure (see also chapter 5), and because the initial pedestal pressure collapse will leave the pedestal in the unstable domain until the current relaxes to a much lower value. This cycle's frequency will increase with input power, and it provides a model for large type-I ELMs.

Finally, cycle "II" occurs at large input power if the current remains below the marginal peeling stability boundary. This can occur either at high density, where high collisionality leads to a low bootstrap current, or it can occur at somewhat lower density when the peeling limit is high due to strong shaping or large magnetic shear. This cycle is expected to yield relatively small ELMs because the

pressure loss immediately following the ELM crash returns the pedestal to a stable region of the parameter space, and is proposed to explain type-II ELMs.
In the context of [59] no reference is made to the particular case of ELM-free H-modes, but it is natural to expect this regime to occur in those situations in which neither the ballooning nor the peeling marginal stability boundary are hit.
It must be recognised that, while the above extended model for ELM cycles is attractive in that in confers a to the ELM phenomenon a remarkable simplicity, it is somewhat handwavy, and so far no direct experimental evidence exists for its validity. There are a number of weak points in this model. It does not explain why the type-I ELM cycle does not hit in first instance the ballooning stability limit although enough heating power is applied, or why a type-I ELM or type-III ELM crash is not immediately followed by a cascade of further type-III ELMs.
Note that within the proposed models of ELM cycles, the pedestal dynamics and the energy loss resulting from an ELM crash are merely justified through linear MHD stability considerations. Nonlinear effects are not included in this model.

3.4 Comparisons of theory and experiment

Due to diagnostic limitations the comparison of theoretical predictions with experiment is challenging. A number of edge quantities, which are critical for the edge plasma stability, are difficult to measure. In order to resolve the steep gradients at the transport barrier very high spatial resolution, at the limit of the present achievable values, is required. Furthermore, it has not been possible so far to measure the radial distribution of the edge current density, at least not with sufficient accuracy to determine if second stability access is open or not, and thus assumptions about the edge current distribution have to be made when comparing with theory. Due to these limitations, direct comparisons of experiment with results from stability simulations need to be generally regarded with caution. A fairly large number of interpretations of the ELM event have emerged from such comparisons, and no clear picture exists yet.

Localisation of ELMs

A number of experimental observations shows that the mode responsible for type-I ELMs must be localised on the low field side of the plasma. In [82] it is reported that the onset of the D_α emission at the outside midplane, which is the region most susceptible to the ballooning instability, and at the outside divertor plates precedes that at the inside divertor plates by 200 μs, which is consistent with the type-I ELM occurring initially at the outside midplane and then propagating poloidally at approximately the ion sound velocity along the plasma periphery. Such delays have been also observed in JET and JT-60U in discharges with high pedestal collisionality [22, 83]. In discharges with low

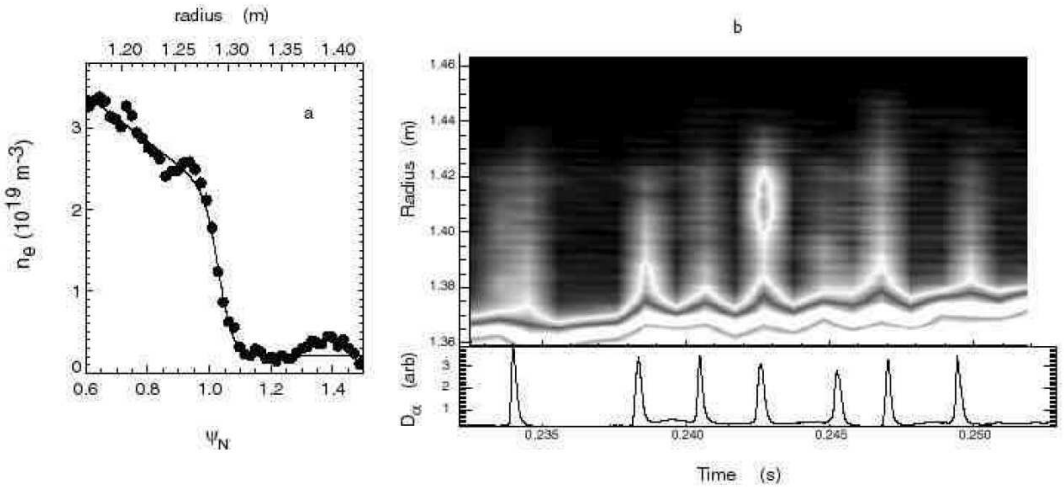

Figure 3.17: MAST measurements showing (a) a density profile of the outboard edge within 20 μs of an ELM, obtained from Thomson scattering, and (b) an Abel inverted signal from a linear D_α array viewing the outboard mid-plane (from [87]).

pedestal collisionality the delay is however not observed. It has been argued that in those cases the transport in the SOL to the divertor may be dominated by the much faster electrons [83].
It has been reported in DIII-D that, in discharges close to double-null configuration, the deposition of energy and particles from type-I ELM bursts occurs entirely at the outer, and not the inner, divertor plates [84]. Further evidence for the poloidal asymmetry of the type-I ELM collapse was obtained from edge density measurements on the low and high field side of JT-60U [85]. Again, the density perturbation from the ELM was found to be initiated at the low field and then propagate on a slower time scale towards the high field side of the plasma. ELMs observed on MAST, which are believed to be of type-III [86], are also found to be localised on the outboard side of the plasma [86, 87]. Some remarkable measurements have been made very recently. Figure 3.17 shows (a) a Thomson scattering density profile of the outboard edge within 20 μs of an ELM, and (b) the Abel inverted signal from a linear D_α array viewing the outboard mid-plane plotted as radius versus time. In both cases there seems to be a plasma "blob" associated with the ELM. This blob seems to occur only on the low field side (Thomson scattering profiles of the inboard side, not shown here, show very little change with the ELM [87]). Figure 3.18 shows a "snapshot" of an ELM, together with a further image just after the ELM, obtained with a high speed video camera. In the picture taken at the start of the ELM clear tube-like structures can be observed on the outboard side, which by the end of the ELM have disappeared. The structures have a similar spatial distribution as

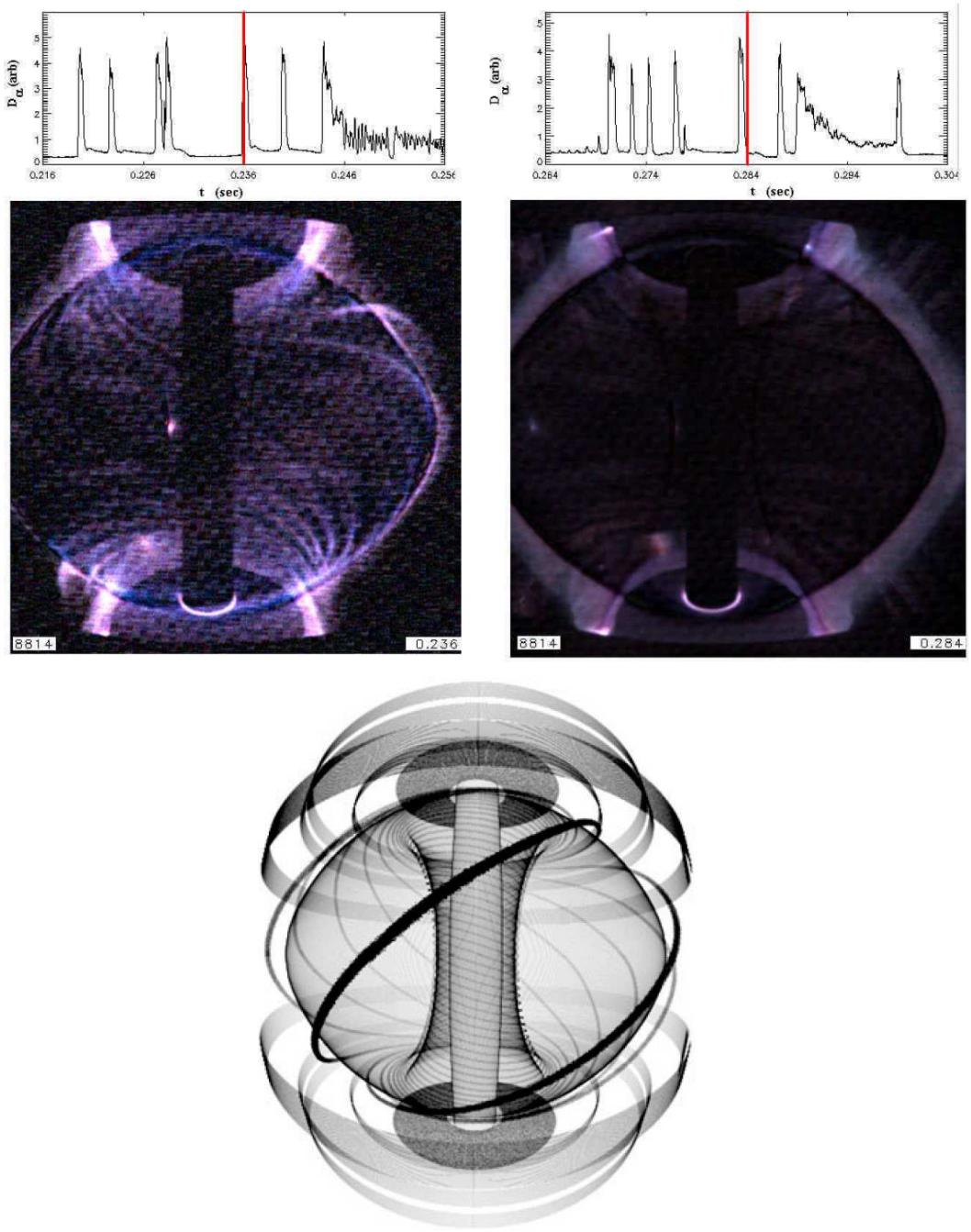

Figure 3.18: Top: Video image of ELMs on MAST, obtained with a high speed camera with short exposure time (25 μs). The left hand image was taken at the start of an ELM, the right hand image at the tail of an ELM (the red vertical line on the D_α trace indicates the time of the photo in each case). Bottom: An image plane simulation of what the structure would look like if close to the $q = 4$ surface and $n = 10$ (from [87, 88]).

in the image simulation shown below, suggesting that they are aligned with the magnetic field lines. It can further be seen that at least part of the structures are located outside the separatrix (cf. the single extended tube in the upper right corner of the figure), and strongly resemble the behaviour predicted by the nonlinear ballooning model (compare with figure 3.10).
Magnetic measurements of precursor activity found prior to ELMs on TCV (which, as in the case of MAST, are believed to be of type-III) have been made. The measurements showed also a strong localisation of the activity, both toroidally and poloidally, on the bad curvature side of the torus [89].
These observations support the role of the ballooning mode (or the coupled peeling-ballooning mode) in triggering both the type-I and the type-III ELM. This is somewhat surprising in that type-I and type-III ELMs clearly have different characteristics, as discussed in section 3.2. It may be speculated that type-I ELMs become triggered by ideal type ballooning modes, while type-III ELMs are triggered by resistive type ballooning modes.

Pedestal measurements

Detailed edge pressure gradient measurements and comparison against predictions from high-n ballooning theory have been made on various devices, for the first time in DIII-D in 1988 [82]. More recent measurements with improved diagnostics show that, for given plasma shape, the pedestal pressure gradient prior to type-I ELMs is found to scale as would be expected for a stability limit set by ideal infinite-n ballooning modes ($p' \propto B^2/(2\mu_0 R q_{95}^2)$ or $p' \propto I_p^2$) [12,23,27,90,91]. (In the case of [27], p' is approximated as the pressure measured near the pedestal top, divided by the pedestal width.) However, in DIII-D the measured absolute values of p' are significantly in excess (by up to a factor 2) of that predicted by stability calculations in the absence of bootstrap current [23]. Two possible explanations for this are currently being considered. Firstly, that the finite edge current at the transport barrier and the associated decrease in edge shear could allow for access to the second stable regime for ballooning modes, and that the pressure gradient is then finally limited by finite-n coupled peeling-ballooning modes triggering the ELM. Secondly, that the plasma edge is still in the first stable region for ballooning modes, and that FLR stabilisation effects increase the threshold for ideal ballooning mode destabilization.
Pedestal measurements on DIII-D reveal that the pressure gradient prior to type-III ELMs is much lower than the critical value obtained for ballooning stability ($0.3 \leq \alpha/\alpha_{crit} \leq 0.5$). On ASDEX Upgrade it is found that the pressure gradient prior to type-III ELMs is generally lower than, but in some cases also similar to, values expected from ideal ballooning stability calculations [12].

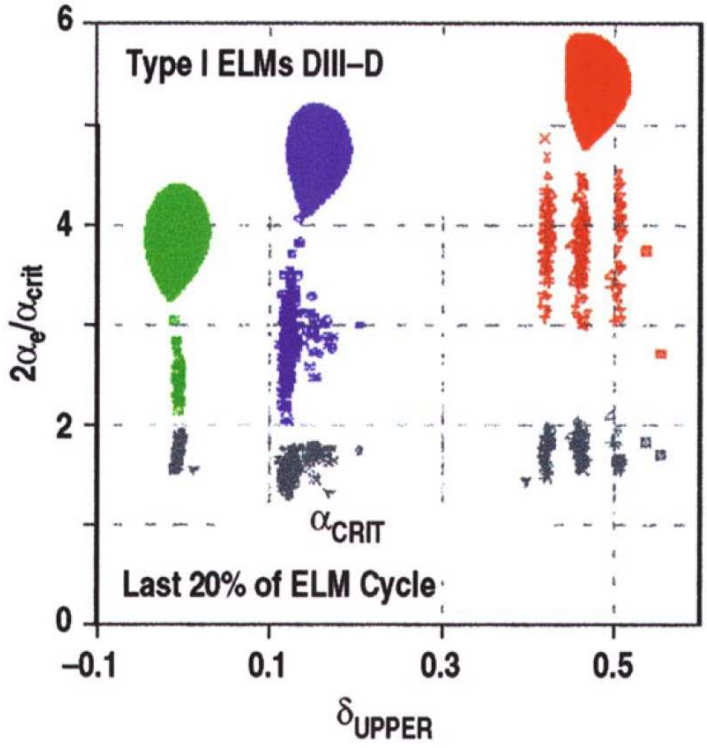

Figure 3.19: Normalised edge pressure gradient α averaged over the last 20% of the ELM cycle as a function of the upper triangularity of the plasma shape for a set of moderate density DIII-D discharges. Also shown are the normalised pressure gradients α_{crit} at the first ballooning stability limit in the absence of bootstrap current [90].

Shape dependence

It has been found in DIII-D that the pressure at the top of the pedestal increases strongly with triangularity δ (see figure 3.19) [90]. This is primarily due to an increase in the margin by which the edge pressure gradient exceeds the ballooning mode first stability limit (the pedestal width is found to be relatively independent of δ). The edge pressure gradient is found to increase with triangularity also at ASDEX Upgrade [92]. Furthermore, an increase of the estimated α with plasma triangularity and elongation was reported from JT-60U [27]. This observation can so far not be explained by diamagnetic stabilisation, at least as long as the pedestal width remains constant. On the other hand, modelling computations of discharges have shown that access to second stability is easier to achieve at high triangularity [57, 93, 94, 103], as predicted by [58, 80], and may thus explain the observed increase of the pedestal pressure gradient.
It has been identified that ELM behaviour (frequency and amplitude) on DIII-D may be changed through variation of the squareness of the plasma shape [95,96].

The observed behaviour was found to be consistent with the reduced access to second stability at low and high squareness predicted by stability simulations. However, in contrast to this, a subsequent multi-machine comparison of the modelling simulations performed on various devices yielded no obvious correlation between access to second stability and the ELM regime [97].

Modelling calculations

The Connor model for type-I ELMs was tested in realistic ASDEX Upgrade geometry in [98]. The bootstrap current showed to be destabilising for peeling modes, and stabilising for ballooning modes. The results were found to be compatible with the Connor model, and hence with the possibility that a combination of peeling and ballooning modes may trigger the type-I ELM collapse.
In linear stability calculations of Alcator C-Mod plasmas, the stability of infinite-n ideal ballooning modes and intermediate n coupled peeling-ballooning modes was studied. The results suggest that EDA plasmas are ideal MHD stable [37]. This, together with the requirement of low pedestal temperature for EDA existence, supports theoretical models on the resistive character of the quasi-coherent mode (QCM).
The effect of strong gas fuelling on plasma stability in JET has been modelled in [93, 99] (figure 3.20). It is found that, while the discharge with no gas fuelling enters the second ballooning stability region, a sufficiently high gas flux can bring the JET plasma from a second stable regime back to first ballooning stability regime. Gas fuelling further keeps the discharge away from the marginal kink stability boundary. This results from the increase in edge collisionality with gas fuelling and the associated decrease of the bootstrap current at the transport barrier.
It has been conjectured that the transition from type-I to type-II ELM regime could be related to the access from first to second ballooning stability. Results from modelling computations on DIII-D [25], JT-60U [28] and JET [32, 101] are at least consistent with this picture.
Alternatively, it has been proposed in [102], on the basis of modelling results of JET data, that type-II ELMs might occur if only flux surfaces very close to the plasma edge become unstable to ideal ballooning modes. Within this model, high triangularity, β_p and edge safety factor are favourable for type-II ELMs. In modelling calculations from ASDEX Upgrade discharges with and without type-II ELMs [103], peeling-ballooning modes showed to become more stable and more localised at high triangularity, high q_{95} and in configurations close to double-null. It was concluded that these changes of stability properties may provide an explanation for the small amplitude of type-II ELMs.

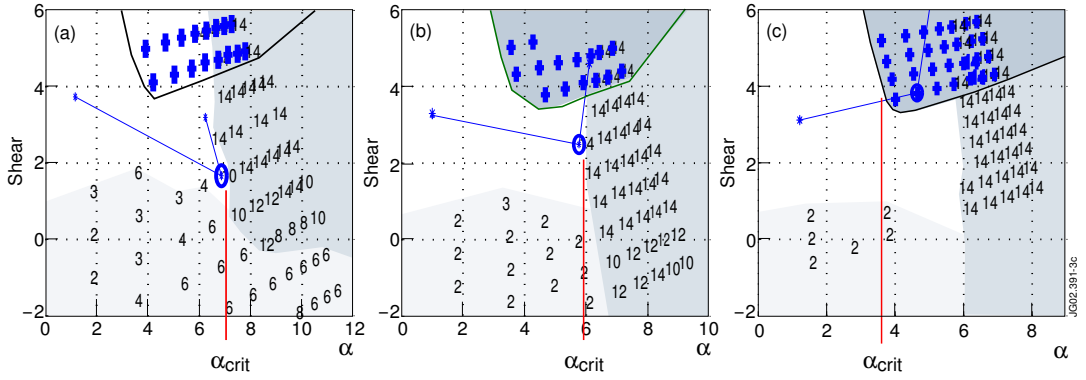

Figure 3.20: MHD stability diagrams in s-α space with different levels gas fuelling: (a) 0 el/s, (b) $4{\cdot}10^{22}$ el/s, (c) $1{\cdot}10^{23}$ el/s. The numbers indicate the mode number of the most unstable mode. The infinite-n ballooning unstable region has been marked with crosses. Three operational points have been plotted (for $\rho = 0.92$, 0.95 and 0.99, where ρ is the normalised minor radius). The location of the top of the transport barrier ($\rho = 0.95$) has been marked with a circle. α_{crit} marks the maximum allowed pressure gradient in each case (from [93]).

ELM affected area

As mentioned in section 3.3.4, it has been conjectured in [59] that the size of ELMs (which is usually quantified as the fraction of pedestal energy content lost with the ELM) could be related to the radial extent of the most unstable mode. While initial comparisons on DIII-D of the calculated mode structure with the experimentally observed radial ELM depth (here obtained through analysis of temperature profiles just before and just after an ELM crash) yielded reasonable agreement [59], a more detailed analysis has shown that the region of perturbation of an ELM is in general considerably wider than the predicted eigenmode width [8]. This indicates that there may not be a direct correspondence between the eigenmode width and the ELM affected region.

Benchmark of modelling

Kink (peeling) modes with low n ($n = 1$ mostly) could be unambiguously identified in JET [66]. Thus, discharges with external kinks provide a good opportunity to test modelling simulations.
One example is shown in figure 3.21 [104]. It shows the trajectories of two discharges in j-α space, one with and one without a current ramp down during the

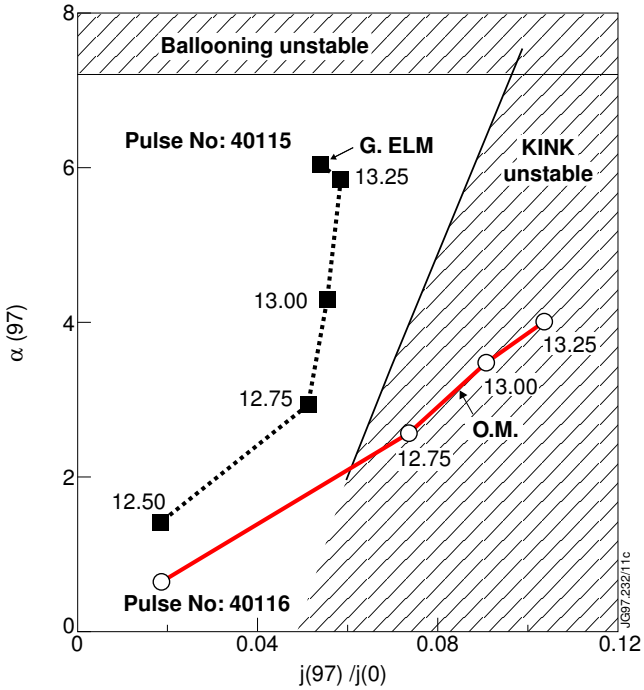

Figure 3.21: Trajectories in j-α space of two discharges with (dashed curve) and without (solid curve) a current ramp down during the hot-ion phase of the discharge. The numbers given along the trajectories specify the time (in sec). The discharge without a current ramp down shows to be more unstable to external kink modes, and less unstable to ballooning modes, than the discharge with current ramp down. "O.M." marks the time of the onset of the external kink observed in experiment. The current density is taken at the flux surface which encloses 97% of the total poloidal magnetic flux (from [104]).

discharge. The aim of the current ramp down technique is to reduce the edge current density and thus avoid the onset of external kinks [104].
In figure 3.21, the pressure gradient at the edge (i.e. α) is not measured. Both the edge pressure profile and the edge current density, including the contribution of the bootstrap current, are taken from numerical simulations which use a transport model (described in [105]). The pressure profiles calculated numerically were compared with the experimental profiles, such that the calculated and measured profiles at the top of the pedestal coincide within the experimental uncertainty.
Experimentally, it is observed that in the discharge without a current ramp down an external kink becomes destabilised at 12.9 s, and lasts until $\sim$ 13.25 s where it is interrupted by an ELM. In the discharge with current ramp down (dashed trajectory) the kink is inhibited, at least until very shortly before the giant ELM appears.

Although the accuracy of the theoretical predictions is limited, it can be seen that the modelling calculations predict the discharge without a current ramp down to become kink unstable, while the discharge with a current ramp down remains kink stable.

Summarising, the comparison of theory with experimental observations has so far not yielded a clear picture of the ELM phenomenon. It is clearly necessary to provide improved measurements, in particular of the critical pedestal quantities, in order to constrain modelling simulations and reduce the number of free parameters involved. Further constraints are needed from the analysis and interpretation of fast MHD signals, since they can provide direct experimental information about edge instabilities present in the plasma, and thus validate, or refute, theoretical predictions. Such MHD studies constitute the central subject of this thesis, and will be presented in chapters 5 and 6. In contrast to kink modes, which have been identified on JET, so far ballooning modes or coupled peeling-ballooning modes could not be identified on any device. The material that will be presented in chapter 5 provides strong evidence for the existence of coupled peeling-ballooning modes on JET.

References

[1] Wagner F *et al* 1982 *Phys. Rev. Lett.* **49** 1408

[2] Wagner F *et al* 1991 *Plasma Physics and Controlled Nuclear Fusion Research (Proc. 13th Int. Conf., Washington, 1990)* vol. 1 (Vienna: IAEA) p 277

[3] ITER Confinement Database and Modelling Expert Group (presented by Takizuka T) 1997 *Fusion Energy (Proc. 16th Int. Conf., Montreal, 1996)* vol 2 (Vienna: IAEA) p795

[4] The ITER H-mode Threshold Database Working Group (presented by Righi E) 1998 *Plasma Phys. Control. Fusion* **40** 857

[5] Connor J W and Wilson H R 2000 *Plasma Phys. Control. Fusion* **42** R1

[6] Leonard A W *et al* 1999 *J. Nucl. Mater.* **266-269** 109

[7] Janeschitz G 2001 *J. Nucl. Mater.* **290-293**

[8] Leonard A W *et al* 2003 *Phys. Plasmas* **10** 1765

[9] Doyle E J *et al* 1991 *Phys. Fluids B* **3** 2300

[10] Bhatnagar V P *et al* 1999 *Nucl. Fusion* **39** 353

[11] Horton L D *et al* 1999 *Plasma Phys. Control. Fusion* **41** B329

[12] Suttrop W *et al* 1997 *Plasma Phys. Control. Fusion* **39** 2051

[13] Hubbard A E *et al* 1998 *Phys. Plasmas* **5** 1744

[14] Osborne T H *et al* 1997 *Proc. 24th EPS Conf. on Plasma Physics and Controlled Fusion Research (Berchtesgaden, Germany)* vol 21A, part III, p 1101

[15] Eich T, Herrmann A, Andrew P and Loarte A 2003 *J. Nucl. Mater.* **313-316** 919

[16] Federici G *et al* 2003 *J. Nucl. Mater.* **313-316** 11

[17] Ghendrih P *et al* 2003 *J. Nucl. Mater.* **313-316** 914

[18] Herrmann A *et al* 2003 *J. Nucl. Mater.* **313-316** 759

[19] Horton L D *et al* 1999 *Nucl. Fusion* **39** 1 1

[20] Leonard A W *et al* 2002 *Plasma Phys. Control. Fusion* **44** 945

[21] Loarte A *et al* 2003 *J. Nucl. Mater.* **313-316** 962

[22] Loarte A *et al* 2002 *Plasma Phys. Control. Fusion* **44** 1815

[23] Osborne T H *et al* 1998 *Plasma Phys. Control. Fusion* **40** 845

[24] Rapp J *et al* 2002 *Plasma Phys. Control. Fusion* **44** 639

[25] Ozeki T *et al* 1990 *Nucl. Fusion* **30** 1425

[26] DIII-D Team 1990 *Plasma Phys. Control. Nucl. Fusion Res.* **1** 69 IAEA-CN-53/A-I-4

[27] Kamada Y *et al* 1996 *Plasma Phys. Control. Fusion* **38** 1387

[28] Kamada Y *et al* 2000 *Plasma Phys. Control. Fusion* **42** A247

[29] Kamada Y *et al* 2002 *Plasma Phys. Control. Fusion* **44** A279

[30] Stober J *et al* 2001 *Nucl. Fusion* **41** 1123

[31] Sips A C C *et al* 2002 *Plasma Phys. Control. Fusion* **44** A151

[32] Saibene G *et al* 2002 *Plasma Phys. Control. Fusion* **44** 1769

[33] Saibene G *et al* 2003 *Proc. 30th EPS Conference on Contr. Fusion and Plasma Phys. (St. Petersburg, Russia)*, ECA Vol. 27A, P-1.092

[34] Sartori R *et al* 2002 *Plasma Phys. Control. Fusion* **44** 1801

[35] Greenwald M *et al* 1999 *Phys. Plasmas* **6** 1943

[36] Hubbard A E *et al* 2001 *Phys. Plasmas* **8** 2033

[37] Mossessian D A *et al* 2002 *Plasma Phys. Control. Fusion* **44** 423

[38] Snipes J A *et al* 2001 *Plasma Phys. Control. Fusion* **43** L23

[39] Snipes J A *et al* 1998 *Plasma Phys. Control. Fusion* **40** 765

[40] Doyle E J *et al* 2001 *Plasma Phys. Control. Fusion* **43** A95

[41] Burrell K H *et al* 2002 *Plasma Phys. Control. Fusion* **44** A253

[42] Burrell K H *et al* 2001 *Phys. Plasmas* **8** 2153

[43] Suttrop W *et al* 2003 *Plasma Phys. Control. Fusion* **45** 1399

[44] Doyle E J *et al* 2002 *Proc. 19th IAEA Conf. on Fusion Energy (Lyon, 2002) (CD-ROM)(Vienna: IAEA)* IAEA-CN-94/EX/C3-2

[45] West W P *et al* 2002 *Phys. Plasmas* **9** 1970

[46] Freidberg J P 1987 *Ideal Magnetohydrodynamics* (Plenum Press, New York)

[47] Wesson J A 1997 *Tokamaks* (Clarendon Press: Oxford)

[48] Connor J W, Hastie R J, and Taylor J B 1978 *Phys. Rev. Lett.* **40** 396

[49] Connor J W, Hastie R J, and Taylor J B 1979 *Proc. R. Soc. Lond.* **A365** 1

[50] Connor J W, Hastie, R J, Wilson H R, and Miller R L 1998 *Phys. Plasmas* **5** 2687

[51] Huysmans G T A, Sharapov S E, Mikhailovskii A B, and Kerner W 2001 *Phys. Plasmas* **8** 4292

[52] Mikhailovskii A B, Huysmans G T A, Sharapov S E, and Kerner W 1997 *Plasma Phys. Rep.* **23** 844

[53] Tang W M, Connor J W, and White R B 1981 *Nucl. Fusion* **21** 891

[54] Tang W M, Dewar R L, Manickham J 1982 *Nucl. Fusion* **22** 1079

[55] Rogers B N, and Drake J F 1999 *Phys. Plasmas* **6** 2797

[56] Hastie R J, Catto P J, and Ramos J J 2000 *Phys. Plasmas* **7** 4561

[57] Huysmans G T A 2001 *9th European Fusion Physics Workshop (Saariselkä, Finland)*

[58] Miller R L, Lin-Liu J L, Osborne T H, and Taylor T S 1998 *Plasma Phys. Control. Fusion* **40** 753

[59] Snyder P B *et al* 2002 *Phys. Plasmas* **9** 2037

[60] Cowley S C, Wilson H, Hurricane O A and Fong B 2003 *Plasma Phys. Control. Fusion* **45** A31

[61] Cowley S C, Artun M and Albright B 1996 *Phys. Plasmas* **3** 1848

[62] Hurricane O A, Fong B H, Cowley S C 1997 *Phys. Plasmas* **4** 3565

[63] Fong B H, Cowley S C and Hurricane O A 1999 *Phys. Rev. Lett.* **82** 4651

[64] Fong B H 1999 "Metastable and explosive properties of ballooning modes in laboratory and space plasmas", *PhD thesis*, available at http://www.asp.ucar.edu/∼bhlfong/thesis.pdf

[65] Wilson H and Cowley S C *Phys. Rev. Lett.* submitted

[66] Huysmans G T A, Hender T C, and Alper B 1998 *Nucl. Fusion* **38** 179

[67] Shafranov V D 1970 *Soviet Physics-Technical Physics* **15** 175

[68] Lortz D 1975 *Nucl. Fusion* **15** 49

[69] Wesson J A 1978 *Nucl. Fusion* **18** 87

[70] Grimm R C, Greene J M, and Johnson J L 1975 *Methods Comput. Phys.* **16** 273

[71] Manickam J 1992 *Phys. Fluids* B **4** 1901

[72] Huysmans G T A, Challis C D, Erba M, Kerner W and Parail V V 1995 *Proc. 22nd EPS Conf. on Controlled Fusion and Plasma Physics (Bournemouth, 1995)* ed B E Keen *et al* (Geneva: European Physical Society), part I, p 201

[73] Kerner W, Poedts S, Goedbloed J P, Huysmans G T A, Keegan B, Schwarz E 1991 *Proc. 18th EPS Conf. on Controlled Fusion and Plasma Physics (Berlin, 1991)*, part IV, p 89

[74] Goedbloed J P, Holties H A, Poedts S, Huysmans G T A and Kerner W 1993 *Plasma Phys. Control. Fusion* **35** B277

[75] Huysmans G T A, Goedbloed J P, Kerner W 1991 *Proc. CP90 Conf. on Comput. Physics*, ed. A. Tenner (World Scientific Singapore) p 371

[76] Cenacchi G, Taroni A 1988 Rapporto ENEA RT/T1B 88 (5)

[77] Hegna C C, Connor J W, Hastie R J, Wilson H R 1996 *Phys. Plasmas* **3** 584

[78] Connor J W, Wilson H R 1997 *Theory of Fusion Plasmas,*, Varenna, ed J W Connor, E Sindoni and J Vaclavik (Editrice Compositori, Bologna, 1997), p 441

[79] Wilson, H R, Snyder P B and Huysmans G T A 2001 *Proc. 28th EPS Conference on Contr. Fusion and Plasma Phys. (Funchal, Portugal)* P3.039

[80] Wilson H R, Miller R L 1999 *Phys. Plasmas* **6** 873

[81] Wilson H R, Snyder P B, Huysmans G T A, and Miller R L 2002 *Phys. Plasmas* **9** 1277

[82] Gohil P *et al* 1988 *Phys. Rev. Lett.* **61** 1603

[83] Chankin A V *et al* 2002 *Nucl. Fusion* **42** 733

[84] Petrie T W, Watkins J G, Lao LL, Snyder P B, *Phys. Rev. Lett.* submitted for publication

[85] Oyama N *et al* 2003 *Nucl. Fusion* **43** 1250

[86] Kirk A *et al* 2003 *J. Nucl. Mater.* **313-316** 1081

[87] Kirk A *et al* 2003 *Proc. 30th EPS Conf. on Controlled Fusion and Plasma Physics (St. Petersburg, 2003)* P-3.201

[88] Akers R *et al* 2003 *Plasma Phys. Control. Fusion* **45** A175

[89] Reimerdes H, Pochelon A, Suttrop W 1998 *Nucl. Fusion* **38** 319

[90] Osborne T *et al* 2000 *Plasma Phys. Control. Fusion* **42** A175

[91] Suttrop W *et al* 1996 *Proc. 23rd EPS Conf. on Contr. Fusion and Plasma Physics (Kiev, 1996)*, ed D Gresillon *et al* (Geneva: European Physical Society), part I, p 47

[92] Suttrop W *et al* 2000 *Plasma Phys. Control. Fusion* **42** A97

[93] Parail V *et al* 2002 *Proc. 19th IAEA Fusion Energy Conference (Lyon, 2002)* IAEA-CN-94-TH/P3-08

[94] Osborne T *et al* 1995 *Nucl. Fusion* **35** 23

[95] Turnbull A D, Lin-Liu Y R, Miller R L, Taylor T S, and Todd T N 1999 *Phys. Plasmas* **6** 1113

[96] Lao L L *et al* 1999 *Nucl. Fusion* **39** 1785

[97] Horton L D *et al Plasma Phys. Control. Fusion* **44** A273

[98] Saarelma S, Günter S, Kurki-Suonio T, and Zehrfeld H-P 2002 *Plasma Phys. Control. Fusion* **44** A103

[99] Lonnroth J S *et al* 2002 *Proc. 29th EPS Conf. on Controlled Fusion and Plasma Physics (Montreux, 2002)* P1.024

[100] Zohm H *et al* 1995 *Nucl. Fusion* **35** 543

[101] Becoulet M *et al* 2002 *Plasma Phys. Control. Fusion* **44** A103

[102] Lonnroth J S *et al* 2003 *Proc. 30th EPS Conf. on Controlled Fusion and Plasma Physics (St Petersburg, 2003)* P1.184

[103] Saarelma S *et al* 2003 *Nucl. Fusion* **43** 262

[104] Nave M F F *et al* 1999 *Nucl. Fusion* **39** 1567

[105] JET Team (presented by Taroni A) 1997, in Fusion Energy 1996 (*Proc. 16th Int. Conf. Montreal, 1996*), Vol. 2, IAEA, Vienna, p. 477

Chapter 4

The experimental setup

4.1 The JET tokamak

JET is to date the world's largest tokamak. It produced its first plasma in June 1983. Since January 2000 the scientific programme is conducted by researchers from associations all over Europe in the framework of the European Fusion Development Agreement (EFDA).
Figure 4.1 shows an overview of the JET device, together with some typical plasma parameters. The toroidal magnetic field is produced by a set of 32 D-shaped coils. Inductive coupling between the primary winding and the toroidal plasma is supported by the massive eight limbed transformer core. Around the outside of the vacuum vessel, a set of six poloidal magnetic field coils (outer poloidal field coils) is used for positioning, shaping and stabilising the position of the plasma inside the vessel.
The NBI heating system (not shown in the figure) consists of two racks of injectors capable of delivering a total of 17 MW (recently upgraded to 23 MW) into the plasma for 10 s at injection energies up to 140 keV. The fast particles are injected tangentially into the plasma, in standard mode of operation in the same direction as the plasma current (co-injection). After field and current reversal, counter-injection is also possible. Nominally up to 32 MW of ICRH heating are also available, but since the coupling efficiency is low in the presence of type-I ELMs, in practice not more than 4-8 MW are usually delivered into the plasma. The ICRH antennas can be operated as a phased array for current drive studies. LHCD is also available at JET. The generators are capable of delivering up to 12 MW for 10 s. In practice, the power effectively coupled to the plasma depends on the plasma conditions.
Figure 4.2 shows a magnetic equilibrium reconstruction for a typical JET discharge, calculated by the equilibrium code EFIT [1, 2]. EFIT reconstructs the MHD equilibrium of JET plasmas, i.e. plasma shape, current profiles, etc. using the Grad-Shafranov equation constrained by external magnetic measurements.

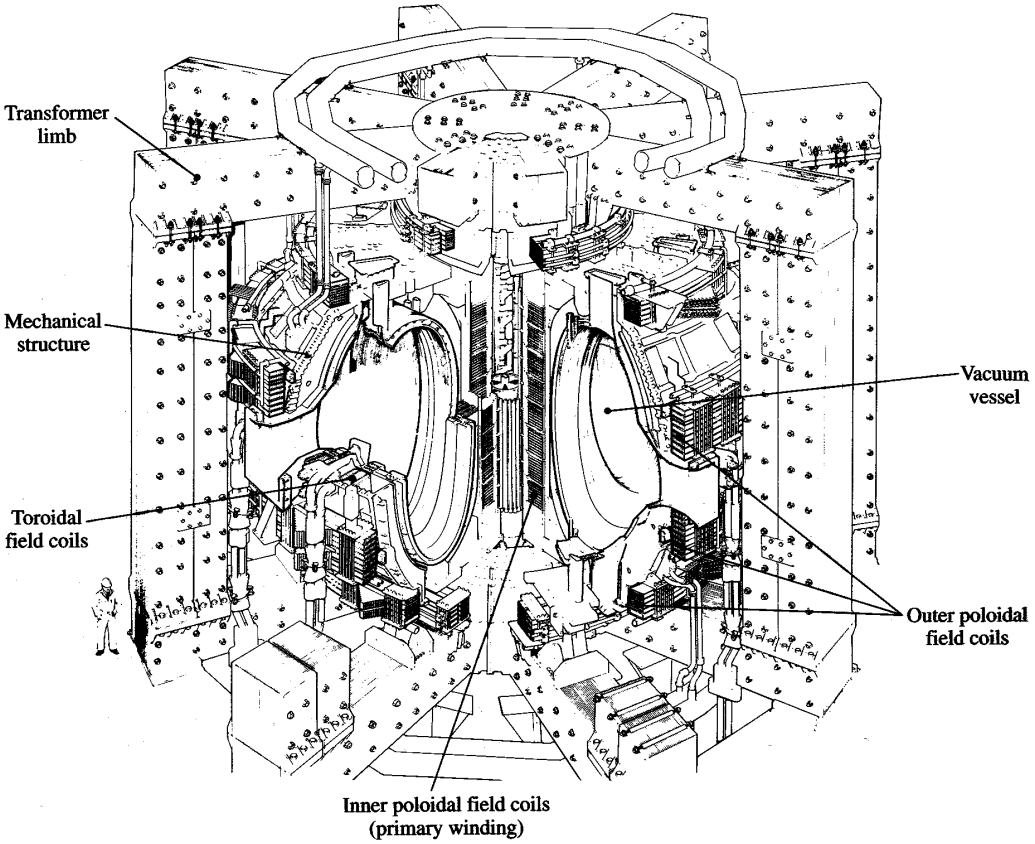

Typical plasma parameters and dimensions	
Major radius (R_0)	$\sim$ 3 m
Minor radius (horizontally)	$\sim$ 0.9 m
Elongation	$\sim$ 1.6 - 1.8
Triangularity	$\sim$ 0.2 - 0.5
Toroidal field	$\sim$ 1.0 - 3.8 T
Plasma current	$\sim$ 0.9 - 4.0 MA
Pulse length	$\sim$ 10 - 32 s
NBI power	$\lesssim$ 17 MW
coupled ICRH power	$\lesssim$ 8 MW
coupled LHCD power	$\lesssim$ 5 MW

Figure 4.1: Layout of the JET device, together with some typical plasma parameters.

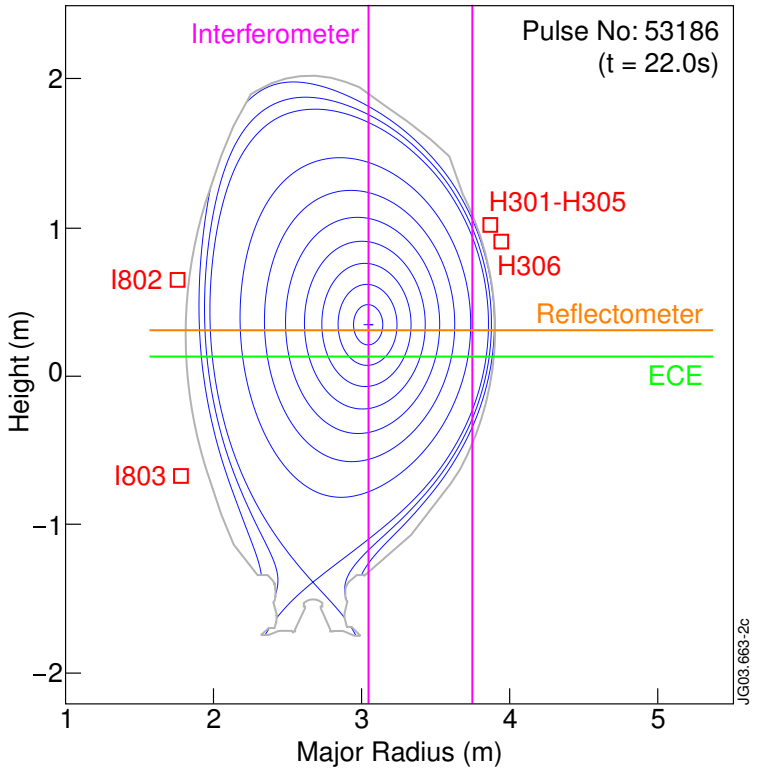

Figure 4.2: Magnetic equilibrium reconstruction for a JET discharge (no. 53186) together with the JET first wall. Also shown are the lines of sight of selected diagnostics (ECE, O-mode edge reflectometer and FIR interferometer) and the position coordinates of various Mirnov coils in the poloidal plane (□).

Optionally the code is able to utilise, as additional constraints, internal measurements, such as motional Stark effect (MSE) or far-infrared polarimetry (Faraday rotation) data. As standard for the reconstruction EFIT uses parametrised profiles (e.g. of parabolic shape), and hence does not properly take into account the presence of an edge transport barrier in H-mode plasmas. For that purpose more sophisticated codes are available, such as the equilibrium and transport code JETTO [3]. JETTO calculates the edge magnetic surfaces self-consistently from the edge pressure gradient and the edge current density including the bootstrap current contribution.
Also shown in figure 4.2 are the lines of sight of selected diagnostics relevant for this thesis, namely the ECE detection system, the multichannel O-mode edge reflectometer system and various cords of the far-infrared (FIR) interferometer. The position coordinates of various Mirnov coils in the poloidal plane are also given. These diagnostics will be described in more detail in the following section.

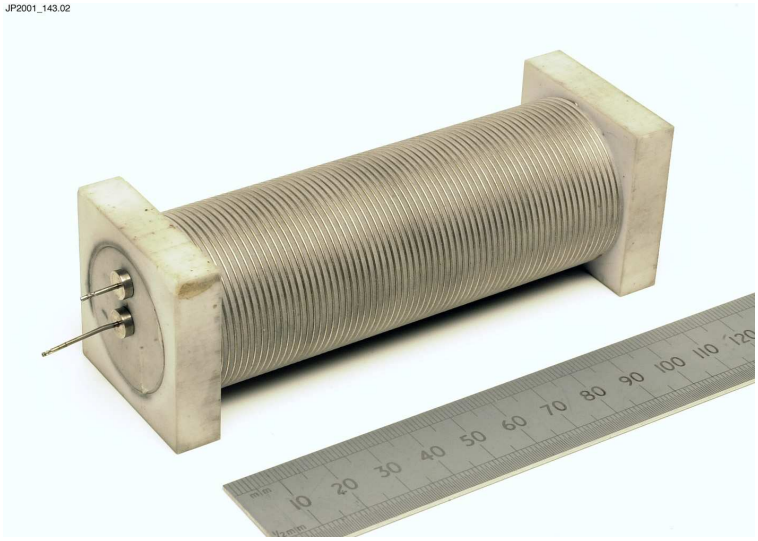

Figure 4.3: A Mirnov coil from the high resolution array installed at JET. The coils are wound from titanium wire in a single layer onto an alumina ceramic former with a return wire through the center of the coil.

4.2 JET diagnostics relevant for this thesis

4.2.1 Mirnov coils

Mirnov coils pick up fluctuations of B_θ (better: changes of the poloidal magnetic flux through the coil, $\int \dot{B}_\theta \, \mathrm{d}A$), and are used as a standard MHD diagnostic on almost all tokamak devices. The coils are installed within the vacuum vessel close to the plasma boundary. By making measurements at different poloidal and toroidal locations the structure of magnetic field perturbations can be determined, as well as their amplitude and frequency. Since magnetic coils detect the time derivative of B (Faraday's law), for a given mode amplitude the detected amplitude of the oscillations on the Mirnov signal will be proportional to the frequency f of the mode. This implies that, in principle, the higher the mode frequency is, the more sensitive the Mirnov diagnostic becomes for that mode. However, technical constraints such as the finite sampling rate of the signal or the finite capacitance of the coil circuit will impose an upper limit on the highest detectable frequency of oscillations.
On JET a number of coil arrays with high frequency response are available. The poloidal distribution of the coils is shown in figure 4.2. The coils are designed for high frequencies up to 500 kHz (figure 4.3).
For this thesis two sets of Mirnov coils are relevant: a set of five coils at same poloidal angles but at different toroidal locations (labelled in figure 4.2 as H301-H305, table 4.1), and a set of four coils at nearly the same toroidal angle at

Coil	R(m)	Z(m)	$\phi(^\circ)$
H301	3.881	1.001	-13.0
H302	3.881	1.013	2.94
H303	3.881	1.005	13.11
H304	3.880	1.045	18.74
H305	3.882	1.007	20.38

Table 4.1: Coordinates of the toroidal set of Mirnov coils H301-H305, for the standard vessel temperature of 200 °C.

different poloidal locations around the plasma (coils I802, I803, H304 and H306 in figure 4.2). Coils H304 and H306 are poloidally 6 degrees apart, while coils I802 and I803 are 50 degrees apart.
The data is collected for selected time windows in the discharge with either 250 kHz or 1 Mhz sampling rate, thus allowing for the study of modes with up to 125 or 500 kHz frequency (Nyquist frequency limit), respectively. In addition, there is a signal from a single Mirnov coil, sampled at 250 kHz, available throughout the whole discharge.

4.2.2 Electron cyclotron emission

The measurement of electron cyclotron emission (ECE) is a passive technique that under certain circumstances can be used to determine the local electron temperature $T_e(r)$ in the plasma. The theory of ECE emission is well understood [4], and its capabilities for measuring T_e are used routinely on almost every fusion device.
The electrons of a magnetically confined plasma gyrate around the field lines and as a consequence emit electromagnetic radiation at their cyclotron frequency

$$\omega_{ce} = \frac{eB}{\gamma m_e}$$

(where γ is the relativistic factor) and its harmonics ($\omega = n\omega_{ce}$, with $n = 1, 2 ...$). The EC waves can propagate in two modes of polarisation perpendicular to the magnetic field in the plasma: as Ordinary (O-mode) waves and eXtraordinary (X-mode) waves. O-mode waves have their electric field vector pointing parallel to the magnetic field in the plasma ($\vec{E} \parallel \vec{B}$), while for X-mode waves $\vec{E} \perp \vec{B}$. On its path towards the receiving antenna, EC waves with frequency ω are continuously emitted and reabsorbed by particles in the plasma resonant at that frequency. The final intensity of EC radiation emitted by the plasma is a convolution of the emission and absorption processes taking place in the plasma

$$I(\omega) = \int \beta_\omega(l) \exp\left[-\int_l \alpha_\omega(l')\ \mathrm{d}l'\right]\mathrm{d}l$$

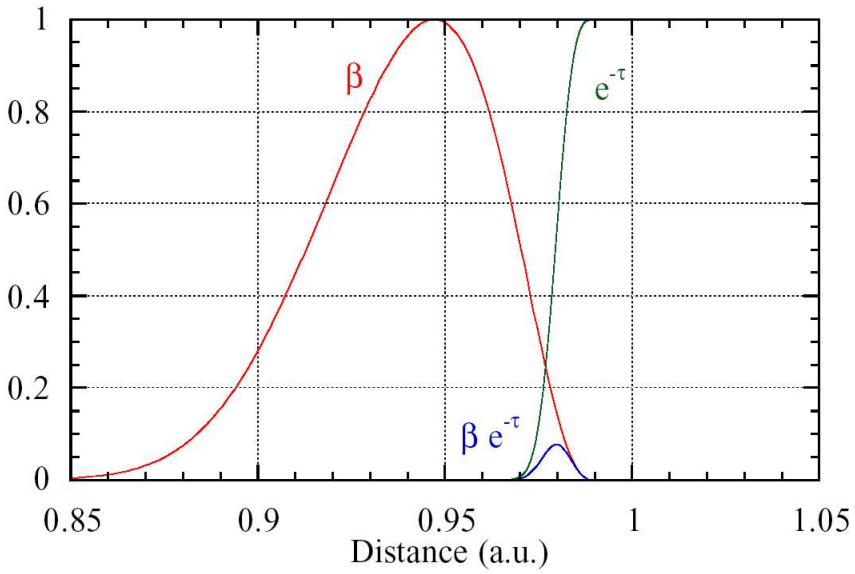

Figure 4.4: Sketch of emission, β, and transmission, $e^{-\tau}$, and emitting profiles (from [5]).

where β_ω and α_ω are the emission and absorption coefficients, respectively. The quantity $\tau(l) \equiv \int_l \alpha_\omega(l')\, \mathrm{d}l'$ is known as the optical depth, and $e^{-\tau}$ as the transmission coefficient. For thermal plasmas the emission and absorption coefficients are proportional (Kirchhoff's law of radiation)

$$\beta_\omega(\vec{r}) = \left(\frac{\omega}{c}\right)^2 \frac{T_e(\vec{r})}{(2\pi)^3} \alpha_\omega(\vec{r})$$

Thus, when the distribution function of the electrons is Maxwellian, the emitted intensity $I(\omega)$ is related to the electron temperature. For plasma conditions where a certain harmonic (and propagating mode) of the electron cyclotron resonance is highly absorbed (the transmission coefficient is very low, or the optical depth is very high) the variation of the transmission coefficient has a peaked shape around the resonance region (see figure 4.4). Hence, for optically thick plasmas the emitted intensity is a measure of the local electron temperature in that region.
The EC absorption coefficient, α, is a complicated function depending on the harmonic, the mode of propagation and the plasma parameters (density and temperature). Generally, the best absorbed harmonics and modes are the 1st harmonic O-mode and the 2nd harmonic X-mode. For these modes the absorption coefficient increases linearly with the density and more than linearly with the temperature. Thus the plasma should be hot and dense enough to be optically thick. These conditions are not necessarily fulfilled in certain plasma regions, i.e. the plasma edge.

On JET an array of 48 (recently upgraded to 96) ECE heterodyne radiometer channels is available, viewing the plasma horizontally from the low field side, slightly below the plasma midplane (figure 4.2). The total range of frequencies that can be measured is 70-140 GHz, but only a subrange of frequencies is selected for operation in a discharge. The frequencies are usually selected such that the ECE channels have their resonance on the low field side, and hence the temperature profile on the outboard midplane is measured. From the receiving antenna on the low field side of the vessel the waves are transmitted to an acquisition system through ~ 40 m long oversized waveguides. First a polarisation switch is used to switch from O- to X-mode operation. Then the signal is passed on to a set of two (out of six available) downconverters. To adjust the range of radii to be covered an algorithm controls the polarisation switch and selects the appropriate downconverters depending on the toroidal magnetic field of the discharge. The downconverters consist of a local oscillator and a mixer. The mixer produces lower and upper sidebands, from which the upper side band is selected (the lower sideband is suppressed by filters). The outcoming signal then has a frequency of 6-18 GHz. From each downconverter the signal is passed on to a low noise amplifier and a splitter, which splits the signal into 24 individual channels 500 MHz apart. Each of these channels passes through a filter bank with 250 MHz bandwidth. The signals are then demodulated by Schottky diodes. The outcoming voltage is proportional to the radiation temperature of the plasma. After passing through a number of amplifiers the resulting DC signal is finally digitised in an ADC. The absolute calibration of the ECE signals is done through cross-calibration with a Michelson-Interferometer.
ECE data with a frequency response of 1 kHz is available throughout the discharge, while for selected time windows fast ECE data with 250 kHz sampling rate is available as well.

4.2.3 O-mode reflectometer

The use of reflectometry [6] is based on the reflection of electromagnetic waves in a plasma. In general, a reflectometer consists of a probing beam (O-mode or X-mode waves) propagating through the plasma and a reference path outside the plasma (see figure 4.5). In the following only the case of O-mode waves is discussed (X-mode reflectometry has not been used within this thesis).
For O-mode waves total reflection occurs at the critical density n_c when the wave frequency, ω, equals the plasma frequency, ω_{pe}, defined as

$$\omega_{pe}(R) = \left(\frac{e^2 n_e(R)}{\epsilon_0 m_e} \right)^{1/2}$$

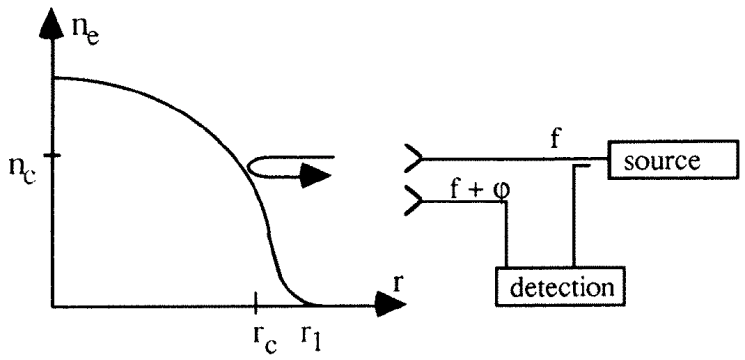

Figure 4.5: A schematic representation of a microwave reflectometer [6].

The microwave beam probing the plasma will undergo a phase shift with respect to the beam in the reference arm. This phase difference is given by [7]

$$\Delta\varphi = 2\frac{\omega}{c}\int_{R_c}^{R_{\text{ant}}}\left(1-\frac{\omega_{pe}^2(R)}{\omega^2}\right)^{1/2}\mathrm{d}R - \frac{\pi}{2} + \frac{\omega}{c}\left(L_s - L_r\right)$$

where R_c is the position of the reflecting layer in the plasma, R_{ant} is the position of the launching antenna, L_s is the length of the waveguides of the signal arm to and from the antenna, and L_r is the length of the waveguides used in the reference arm. Thus, when the source frequency is held constant, a reflectometer will measure changes in the phase difference between the signal path and reference path as a result of variations in the electron density.
Since the set up of the O-mode reflectometer at JET has changed repeatedly over time, here only the configuration relevant for this thesis will be discussed. The system consists of ten channels probing densities from 0.4-6.0 $\times$ 10^{19} m^{-3}. Thus, it can perform simultaneous measurements of density fluctuations at ten radial positions. The distribution of channel frequencies and respective cut off densities is given in table 4.2. The plasma is probed from the low field side along the midplane of the torus (figure 4.2). Due to the relatively low probing densities, in H-mode most, if not all, channels have their cut off at pedestal radii. This converts the JET O-mode reflectometer into a valuable tool for studying density fluctuations at the edge transport barrier.
The waves are generated by voltage-controlled Gunn diodes at different frequencies and combined into a single oversized waveguide. Separate launching and receiving antenna are used to avoid spurious reflections. The phase changes for fluctuation analysis are measured by a coherent detector system (equivalent to a homodyne detector). For each channel phase variations are acquired with a phasemeter at a maximum time resolution of 2 μs.

Channel	Frequency (GHz)	Density (10^{19} m^{-3})
1	18.6	0.43
2	24.3	0.73
3	29.2	1.06
4	33.8	1.42
5	39.5	1.94
6	45.2	2.53
7	50.3	3.14
8	57.1	4.05
9	64.2	5.11
10	69.5	6.00

Table 4.2: Frequencies and cut off densities of the multichannel O-mode reflectometer at JET.

4.2.4 FIR interferometer

Laser interferometry for measuring electron density has become a standard diagnostic tool on most tokamaks. When a coherent O-mode wave passes through the plasma the wave undergoes a change in its phase with respect to a reference beam running in vacuum, due to the finite refractive index of the plasma. At frequencies which are large compared with the plasma frequency, the change in the phase of the beam is proportional to the electron density integrated along the beam probing the plasma

$$\Delta\varphi = \frac{e^2}{4\pi\epsilon_0 m_e c^2}\lambda \int n_e \mathrm{d}l$$

where λ is the vavelength of the radiation. This phase difference can be measured by a Mach-Zehnder interferometer arrangement as shown in figure 4.6.
A multichannel FIR interferometer has been used on JET routinely since 1984 [9]. The system presently consists of four vertical and 4 lateral (oblique) viewing cords. For the purpose of this thesis only the two vertical cords shown in figure 4.2 are of interest, which measure the line-integrated density in the plasma core and at the plasma edge. The instrument is of the Mach-Zehnder type, with a heterodyne detection system. The basic source is a DCN (deuterium cyanide) laser operated at 195 μm. A modulation frequency of 100 kHz is produced by diffraction from a rotating grating (3600 groves rotating at 28 Hz). The input beams are then transferred by free optical propagation through the basement, passing below the biological shield, into the torus hall. The optics in the torus hall is situated in a large C frame (tower) of $\sim$ 52 tons of weight, independent from the machine, to minimise the influence on vibrations on the phase measurement.

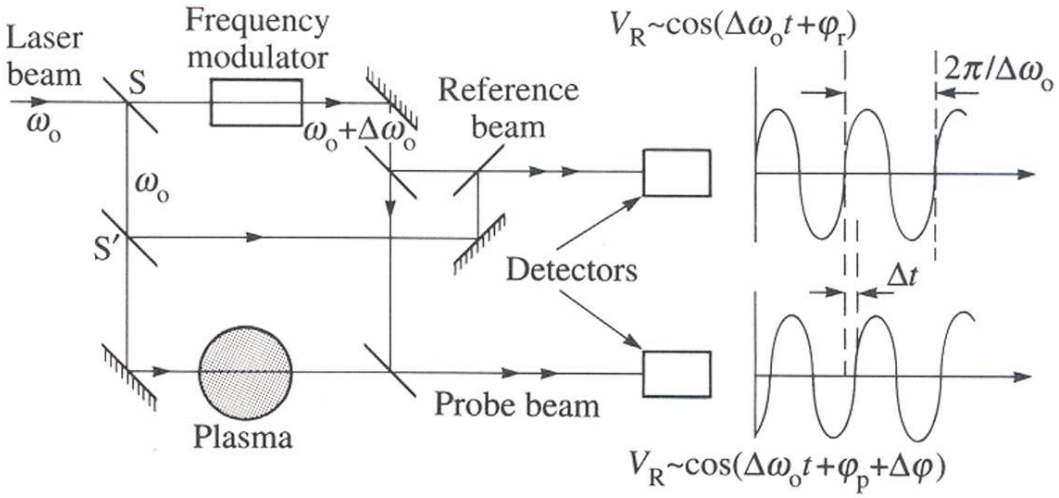

Figure 4.6: Schematic layout of a Mach-Zehnder interferometer [8]. The beams are split into a probing and a reference beam, and are recombined with a frequency shifted beam before reaching the detectors. The beat frequency is chosen to be sufficiently high to allow a good time resolution in the phase measurement, and sufficiently low to be electronically tractable. The phase differences φ_r and φ_p reflect the different pathlengths whereas $\Delta\varphi$ is caused by the refractive effects of the plasma.

The probing beams which arrive in the torus hall are split up into individual channels. A half-wave plate rotates the beam polarisation so that it arrives at the plasma as O-mode wave. One part passes through the plasma and is recombined with the corresponding modulated channels afterwards. The other part is sent back without going through the plasma and recombined with a portion of the modulated beam to constitute the reference beam. On the return path into the diagnostic hall the beams are directed into oversized dielectric waveguides. There, high sensitivity InSb (indium antimonide) He-cooled detectors are used, which allow to perform the the phase shift measurement with an accuracy of 1/20 of a fringe, corresponding to a line-integrated electron density of $5 \times 10^{17}\mathrm{m}^{-2}$. The total distance between laser and detectors is ~ 80 m.
The interferometer data is acquired throughout the discharge with a maximum time resolution of 0.5 ms (faster data for MHD analysis purposes is not used routinely). The data needs to be further validated and corrected for fringe jumps ($\Delta\varphi = 2\pi$). Such fringe jumps can occur when sudden events occur in the plasma, for instance large ELMs or the injection of a pellet. The fringe jump correction is done semi-automatically with the aid of an algorithm.

4.2.5 Soft X-ray cameras

Plasma radiation in the soft X-ray wavelength ($\sim$ 0.1 - 2 nm) can be detected by silicon diodes. The diodes are located in pinhole cameras, viewing the plasma from various angles. They measure the X-ray emission above a threshold energy determined by a thin metallic foil placed in front of the detectors. This way, core or edge radiation can be selected. Each channel yields the line-integrated radiation along the line of sight of the particular diode. Silicon diodes have a very fast time response, typically a fraction of a microsecond. Thus, soft X-ray cameras are well suited for the analysis of fluctuations in the plasma, and are routinely employed for MHD analysis purposes.
In a fusion plasma, there are mainly two sources of soft X-ray radiation: Line-radiation from medium-Z impurities in the plasma core, and continuum radiation from bremsstrahlung. For soft X-ray measurements continuum emission is used. The wavelength range for the measurements is chosen such as to minimise the influence of line-radiation. The soft X-ray flux is sensitive to fluctuations of the electron temperature, electron density and effective charge of the plasma (Z_{eff}). The latter is defined as

$$Z_{\text{eff}} = \frac{\sum_j n_j Z_j^2}{\sum_j n_j Z_j}$$

where the sum goes over all the ion species in the plasma. The (frequency-integrated) flux emitted locally in the plasma scales roughly with $n_e^2 T_e^{1/2} Z_{\text{eff}}$.
On JET several soft X-ray cameras were originally installed, but most of their diodes were damaged by neutrons in past D-T campaigns. This triggered the installation of a pair of radiation hardened soft X-ray cameras [10, 11], which were available for this thesis. The two cameras each contain 17 detector assemblies embedded into a large concrete shield with the detectors viewing the plasma through stainless steel collimators and 250 μm Be windows. The cameras measure radiation in the wavelength range 0.15-2 nm. They are installed at different toroidal locations (octants 4 and 8 of the torus), with same lines of sight in a poloidal cross section, viewing the plasma from the outboard side. The lines of sight are shown in figure 4.7. The fast soft X-ray data is acquired with 250 kHz sampling rate and is available for selected time windows during the discharge.

4.3 Data analysis methods used in this thesis

Signals suitable for the MHD analysis of discharges require a high sampling rate in order to be able to resolve the fluctuations associated with the occurrence of instabilities. Thus, the analysis unavoidably involves processing of large amounts of data. It becomes important to employ efficient means of looking at the data. For this purpose a number of codes for standard MHD analysis of discharges are

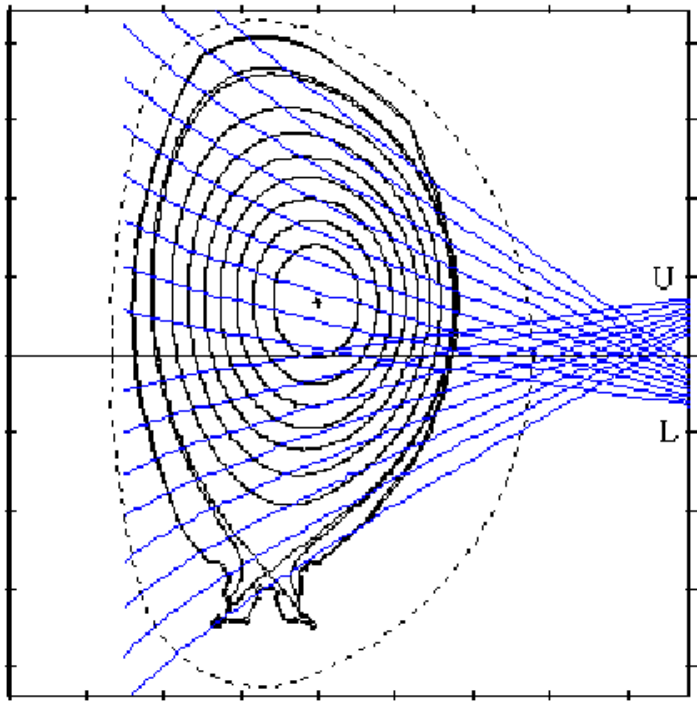

Figure 4.7: Lines of sight of the radiation hardened soft X-ray camera.

available at JET. In addition, an extensive collection of Matlab-based routines has been developed within this thesis, well suited for multipurpose MHD analysis, but also adapted to the specific requirements that have been arising during the thesis. The code, which has been named JETMHD, is still under continuous development and presently spans about 6000 lines of Matlab code. The JETMHD code led to the identification of various phenomena such as the ELM precursors discussed in chapter 5, and most of the material presented in chapters 5 and 6 has been processed with it.
In the following a number of signal processing methods routinely employed in this thesis are outlined.

4.3.1 Spectrograms

Spectrograms are colourmapped images in which every Fourier component of the signal is plotted as a dot in the plane of frequency versus time, and represented by a colour indicating its amplitude. It is convenient to use spectrograms with logarithmic colour scales, as this allows modes spanning many orders of magnitude in amplitude to be displayed. An example of a spectrogram plot can be found in figure 5.2 on page 78.
The original signal is first time-windowed into groups of $n_{\mathrm{FFT}} = 2^N$ samples, where N is a user-determined integer. The optimum value for N depends on the

sampling rate of the signal, e.g. for signals with 250 kHz sampling rate $N = 8$-10 (i.e. 256 to 1024 points per time window) is usually a reasonable choice. Instead of windowing the signal with a box function, it is usually better to use a (bell shaped) Hanning window (this method truncates the data at the beginning and end of the time window in a smoother way). The coefficients of the Hanning windowing function are computed by the following equation

$$w_k = \frac{1}{2}\left[1 - \cos\left(2\pi\frac{k-1}{n_{\mathrm{FFT}}-1}\right)\right] \qquad k = 1, ..., n_{\mathrm{FFT}} \tag{4.1}$$

in which k indicates the index of the sample point in the window. The distance between time windows is $n_{\mathrm{FFT}}/2$ samples, hence there is an overlap. Each window is then fast-fourier-transformed (FFT) to give amplitude as a function of frequency for that particular time interval.
Both the time and the frequency resolution of an FFT-based spectrogram are limited by the "Fourier Uncertainty Principle"

$$\Delta f_{\mathrm{FFT}} \Delta t_{\mathrm{slice}} = 1$$

which is simply a mathematical property of the discrete Fourier transform. Increasing the time resolution of a spectrogram, which is done by decreasing n_{FFT} (i.e. N), comes at the expense of a reduced frequency resolution (a higher Δf_{FFT}). This is because the frequency resolution of the FFT is the sample rate divided by the number of samples in the slice ($\Delta f_{\mathrm{FFT}} = f_{\mathrm{sample}}/n_{\mathrm{FFT}}$).
There are other alternatives to the FFT-based spectrograms, which have been occassionally used within this thesis. Wavelet analysis uses a windowing technique with variable sized regions. It allows the use of long time intervals where more precise low frequency information is needed, and shorter time intervals for high frequency information.

4.3.2 Toroidal mode number determination

It has been mentioned previously that instabilities usually rotate and have helical mode structure. By analysing the relative phase shift of fluctuations picked up by a set of toroidally distributed Mirnov coils, the toroidal mode number n associated with these fluctuations can be deduced.
Starting from the signals measured by the various coils, the signals are first fast-fourier-transformed in a similar way as for the spectrogram. This yields amplitude and phase behaviour as a function of time and frequency for each of the signals. To reduce the computational effort, points for which the Fourier amplitude is below a user-defined threshold ("background noise") are disregarded. Since the phase obtained from the Fourier analysis is in the range from $-\pi$ to $+\pi$, it is necessary to correct for jumps (larger than π) in the relative phase of fluctuations from coil to coil. To that purpose a build-in Matlab function called

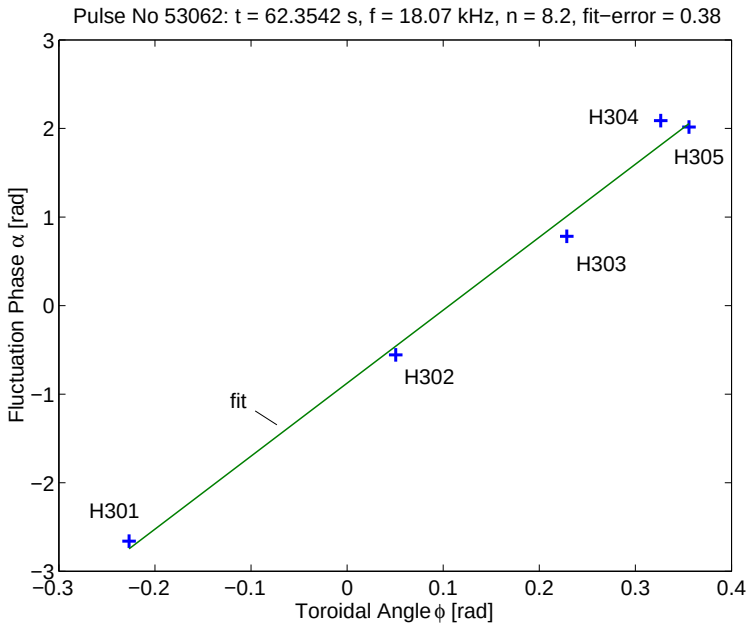

Figure 4.8: Example of a linear fit procedure to obtain the toroidal mode number n. In this case, the nearest integer number to the fit value of 8.2 is 8.

unwrap exists. Given the phases $\alpha_j(t, f)$ of the fluctuations for each time and frequency and the toroidal coordinates ϕ_j of the coils, the toroidal mode number n is in principle given by the "slope":

$$n = \Delta\alpha/\Delta\phi \tag{4.2}$$

Thus, for each time and frequency the corresponding n can be obtained by performing a least squares linear fit of the unwrapped phases α_j versus ϕ_j. As an illustrative example, figure 4.8 shows the result of such a fitting procedure. All the values for t and f are scanned, and the fitting procedure is performed many thousand times until all the points for the plot are computed. To further reduce the noise level of the plots, points are discarded if the fitting error exceeds a certain user-defined threshold, although in practice this option did not prove really necessary. Finally, the n-numbers obtained for each time and frequency are mapped into a colour scheme and plotted versus t and f (without rounding to the nearest integer), in a similar fashion as spectrograms. An example of such a mode number spectrum can be found in figure 5.3 on page 79. In practice, one cannot reliably determine a mode number from a single data point in the space of time and frequency, but all the points corresponding to a given mode generally show up with nearly identical mode numbers, and one can be confident that the mode number is correct.

The range of mode numbers which can be determined is restricted by the limitation that the phase jump $\Delta\alpha$ between probes separated by a toroidal angle $\Delta\phi$

cannot be greater than π. From equation (4.2) the phase jump $\Delta\alpha$ is equivalent to $n\Delta\phi$, so the upper limit for n is given by

$$|n| \leq \pi/|\Delta\phi|$$

Hence, for a given set of coils the maximum n that can be correctly determined is predefined by the largest gap between two coils. For the five coils of the toroidal array available on JET (H301-H305) the largest gap is $\sim 16^\circ$ (between H301 and H302). Thus, this set is suitable for modes with $|n| \leq 11$. A subset of coils with lower $\Delta\phi$ (e.g. H302-H305) can be employed if higher mode numbers need to be resolved, or simply to check the correctness of previous calculations.

4.3.3 Poloidal mode number determination

Although the underlying idea is the same as for toroidal mode numbers, the determination of poloidal mode numbers, m, on the basis of poloidally distributed coils is more complicated because the poloidal symmetry is broken due to the toroidicity of the magnetic flux surfaces. The slope of the magnetic field lines varies poloidally, resulting in a poloidal variation of the wavelength of the mode, which is larger at the outer (low field) side of the torus. Hence, the apparent m number depends on the poloidal angle where the coils are located (so called θ^*-effect [12,13]). For the case of a circular cross section this effect can be described to first order of the inverse aspect ratio by a transformation from θ to θ^*

$$\theta^* = \theta - \left(\beta_p + \frac{l_i}{2} + 1\right)\epsilon \sin\theta$$

where β_p is the poloidal beta, l_i is the internal inductance of the plasma and $\epsilon = r/R_0$ is the inverse aspect ratio. Plasma shaping (elongation, triangularity) and the presence of an X-point impose further difficulties, in particular for modes located close to the plasma boundary. The X-point will distort the poloidal mode structure in such a way that coils picking up magnetic fluctuations around the plasma midplane ($\theta = 0,\ \pi$) will have the tendency to measure a too low m-number.

Only a limited numbers of coils, distributed poloidally around the plasma cross section, are available on JET. For the analysis 4 coils are used, two on the low field side (H304 and H306, which are 6 degrees apart), and two on the high field side (I802 and I803, 50 degrees apart). Equilibrium calculations have shown that on JET the pitch of the field lines at the torus high field side is close to the average pitch of field lines of the magnetic surfaces [14]. Hence, m-numbers determined from coils at the high field side can be taken as an approximation for the true m-number of the modes. The phase difference obtained from the closely spaced coils H304 and H306 at the low field side is used to correct for possible phase jumps in the phase difference for the two coils on the high field side. Due

to aliasing effects the set of coils is not suitable for the analysis of modes with high m numbers. However, for lower m ($\lesssim 6$) the m-number determination has proven reasonably reliable and is routinely used on JET since a number of years.

4.3.4 Coherence analysis

Coherence analysis is a general signal processing technique that can provide further insight into the signal behaviour. It proves to be a very valuable tool in particular for situations in which signals are dominated by noise. In the context of this thesis it is used to obtain information about the radial mode structure of instabilities, specifically about the radial phase behaviour of oscillations and the radial displacement profile $\xi_r(r)$. In principle, the same information could be obtained through straightforward Fourier decomposition. However, the coherence analysis is superior to it in terms of noise reduction. An example of a coherence analysis can be found in figure 5.6 on page 84. Before going into the details of the analysis, it is worth to shortly review some of the signal processing concepts first.

The true *cross-correlation sequence* is a statistical quantity defined as

$$R_{xy}(m) = E[x_{n+m} y_n^*] \tag{4.3}$$

where x_n and y_n are stationary random processes, * stands for the complex conjugate, $-\infty < n < +\infty$, and $E[\,\cdot\,]$ is the expected value operator. In practice, R_{xy} must be estimated, because it is only possible to access a finite segment of the infinite-length random process. A common estimate based on N samples of x_n and y_n is the deterministic cross-correlation sequence (also called time-ambiguity function)

$$\hat{R}_{xy}(m) = \begin{cases} \sum_{n=0}^{N-m-1} x_{n+m} y_m^* & \text{for } \; m \geq 0 \\ \\ \hat{R}_{yx}^*(-m) & \text{for } \; m < 0 \end{cases} \tag{4.4}$$

The *power spectral density*, P_{xx}, of x is defined as

$$P_{xx}(\omega) = \frac{1}{2\pi} \sum_{m=-\infty}^{+\infty} R_{xx}(m)\; e^{-i\omega m} \tag{4.5}$$

where here ω denotes the normalised frequency, $\omega = 2\pi f / f_s$ (f_s is the sampling rate). Thus, $P_{xx}(\omega)$ is related to the autocorrelation sequence of x through the discrete Fourier transform. It can be easily shown that $P_{xx}(\omega)$ is a real quantity. It represents the power content of a signal in an infinitesimal frequency band. In analogy to (4.5), the *cross spectral density* of two signals x and y is given by

$$P_{xy}(\omega) = \frac{1}{2\pi} \sum_{m=-\infty}^{+\infty} R_{xy}(m)\; e^{-i\omega m} \tag{4.6}$$

In general, $P_{xy}(\omega)$ is complex. A related quantity is the magnitude squared *coherence function*, which is defined as

$$C_{xy}(\omega) = \frac{|P_{xy}(\omega)|^2}{P_{xx}(\omega)P_{yy}(\omega)} \tag{4.7}$$

$C_{xy}(\omega)$ is a real number between 0 and 1 and represents a measure for the spectral correlation of fluctuations present in signals x and y.
The routine employed in the context of this thesis calculates the spectral densities P_{xx}, P_{yy} and P_{xy} using Welch's method [15]. The signals are first time-windowed in a similar fashion as for the spectrogram. The signal section to be analysed is then segmented again into eight overlapping sections of equal length. Each of these segments is then windowed with a Hanning window of same length as the segment. The spectral densities (and with them the coherence function) are computed directly from the signal sections with FFT, and the result is then averaged over all eight segments.
As mentioned above, the coherence analysis is used to obtain information about the radial structure of a mode. To this purpose, a preferably clean reference signal (e.g. from the magnetics) is chosen, and the coherence and the cross spectral density of that signal with other signals (e.g. a set of ECE or reflectometer channels) is calculated, for a given time window, at all frequencies. The distribution of the phase of the cross-spectral density (remember that P_{xy} is complex) across the channels is used to obtain information about the radial phase behaviour of the mode oscillations.
For the calculation of the radial displacements it is assumed that all spectra are composed of a constant background and a Gaussian function over the frequency range of interest. The spectrum of the reference signal of the coherence calculation is used to obtain the central position and the width of the Gaussian visible in the frequency range of interest. The spectra of each of the diagnostic channels in the relevant frequency interval is then fitted with a Gaussian of the width and central position of the reference spectrum and a background directly obtained from the power spectrum of the channel. The amplitude A of the fluctuations (e.g. in the case of ECE data, A corresponds to $\Delta T_e(f)$) is then [14]

$$A = 2\sqrt{2\pi}(A_0 - b)s$$

where the factor two is to compensate for the Hanning window function (whose average value is 0.5, see equation (4.1)), A_0 is the peak value of the Gaussian fit, b is the background, and $s = 0.4247 \times$ FWHM (full width half maximum) of the Gaussian fit made to the reference spectrum. Each fit is determined by four parameters: A_0, b, s and the central position f_0. Their standard deviation is used to estimate the error bars for the amplitude. In practice only A_0 and b contribute to the error bars if the reference signal is well chosen. Each oscillation cycle with amplitude A leads to a maximum and a minimum of the local radial

profile of the diagnostic in question. The radial distance between points of equal temperature in the maximum and minimum profiles yields the displacement.

References

[1] Lao L L, John H St, Stambaugh R D, Kellman A G, and Pfeiffer W 1985 *Nucl. Fusion* **25** 1611

[2] O'Brien D P *et al* 1992 *Nucl. Fusion* **32** 1351

[3] Cenacchi G, Taroni A 1988 Rapporto ENEA RT/T1B 88 (5)

[4] Bornatici M, Cano R, de Barbieri O, and Engelmann F 1983 *Nucl. Fusion* **23** 1153

[5] Tribaldos V 2001 EFDA-JET-PR(01) 44

[6] Laviron C, Donné A J H, Manso M E, and Sanchez J 1996 *Plasma Phys. Control. Fusion* **38** 905

[7] Sips A C C and Kramer G J 1993 *Plasma Phys. Control. Fusion* **35** 743

[8] Wesson J A 1997 *Tokamaks* (Clarendon Press: Oxford)

[9] Braithwaite G *et al* 1989 *Rev. Sci. Instrum.* **60** 2825

[10] Gill R D, Alper B, Edwards A W and Dillon S, JET-IR(95)03

[11] Gill R D, Alper B and Edwards A W 1997 JET-R(97)11

[12] Merezhkin V G 1978 *Sov. J. Plasma Phys.* **4** 152

[13] Klueber O *et al* 1991 *Nucl. Fusion* **31** 907

[14] Smeulders P *et al* 1999 *Plasma Phys. Control. Fusion* **41** 1303

[15] Welch P D 1967 *IEEE Trans. Audio Electroacoust.* **AU-15** 70

Chapter 5

Type-I ELM precursor modes in JET

This chapter is a reprint of an article submitted for publication in Nucl. Fusion.

Authors:
C. P. Perez[1,2], H. R. Koslowski[1], G. T. A. Huysmans[3], T. C. Hender[4], P. Smeulders[5], B. Alper[4], E. de la Luna[6], R. J. Hastie[4], L. Meneses[7], M. F. F. Nave[7], V. Parail[4], M. Zerbini[5] and JET-EFDA contributors[a]

[1]Association EURATOM-Forschungszentrum Jülich, Institut für Plasmaphysik, Trilateral Euregio Cluster, D-52425 Jülich, Germany
[2]FOM-Rijnhuizen, Ass. EURATOM-FOM, TEC, PO Box 1207, 3430 BE Nieuwegein, NL
[3]Association Euratom-CEA, Cadarache, F-13108 St. Paul-lez-Durance, France
[4]Euratom/UKAEA Fusion Association, Culham Science Centre, Abingdon, UK
[5]Associazione Euratom-ENEA, Centro Ricerche Frascati, Italy
[6]Laboratorio Nacional de Fusión, Euratom-Ciemat, 28040 Madrid, Spain
[7]Euratom/IST, Instituto Superior Tecnico, Lisbon, Portugal

[a]See annex of J. Pamela et al, "Overview of JET Results", Fusion Energy 2002 (Proc. 19th Int. Conf. Lyon, 2002), IAEA, Vienna (2003).

Abstract. Clear low frequency (typically 5-25 kHz) coherent type-I ELM precursor modes have been identified in JET. They are detected through various diagnostics, especially in the ECE and Mirnov signals, but also on the SXR cameras and the multichannel O-mode edge reflectometer. The modes propagate in the direction of the ion-diamagnetic drift and are usually accompanied by a slight rise in the divertor D_α-emission. The precursors show no radial phase inversions and are localised to a few cm inside the separatrix, in the pedestal region. The time by which the precursor onset precedes the ELM event varies greatly, and ranges from 0.2 ms up to several tens of ms, though the timescale has no effect on the characteristics of the precursors. During their lifetime, the precursor amplitude is often seen to fluctuate, and the frequency and dominant n-number of the precursors can change rapidly, typically within 1 ms. The range of toroidal precursor mode numbers n which have been observed is 1-13. Parametric studies show that n seems to be mainly prescribed by a combination of the electron pedestal pressure and the (normalised) electron pedestal collisionality ν_e^*, with increasing ν_e^* leading to higher n-numbers. Above a certain edge collisionality (roughly $\nu_e^* >$ 1-3) the precursors seem to be absent, indicating that a sufficiently high edge current is important to destabilise the precursors. The low-n precursors are known to be external kinks (also known on JET as Outer Modes), while experimental findings and their comparison with stability calculations suggest that the precursor modes with higher n are not pure external kinks but coupled ballooning-kink modes. Several hundred discharges have been analysed, and, in discharges with low to moderate edge collisionality, the precursors could be detected prior to most type-I ELMs, while prior to type-III ELMs the modes were not encountered. In spite of their regular occurrence, there is no evidence of the

precursor mode growth rate rapidly accelerating before the ELM, indicating that type-I ELMs on JET are not triggered by these modes.

5.1 Introduction

Type-I ELMs [1–3] occur as quasiperiodic particle and heat losses near the plasma edge and are compatible with good confinement at high density. However, the energy losses associated with them are a concern for ITER due to the large transient heat loads expected on the divertor tiles [4,5]. Although their existence has been known for many years, their physics is not well understood, and the search for ELM precursor activity which could shed light onto its origin and control possibilities has been performed in many devices.
In counter-injected discharges in ASDEX-Upgrade low frequency (20 kHz) coherent oscillations starting 1 ms before the ELM have been detected by ECE channels resonant approximately 2 cm inside the separatrix, and by coils picking up oscillations of B_r [6, 7]. Phase shift analysis using 3 toroidally distributed coils yielded n = 5-10 [7]. No similar precursor activity could be observed in co-injected discharges. In a further report, density profile oscillations with 17 kHz frequency in a counter-injected discharge were measured via reflectometry and associated with a type-I ELM precursor [8]. Later on, higher frequency (70-150 kHz) precursors were reported in co-injected NBI discharges [9], detected with a newly installed enhanced Mirnov diagnostic. Up to three modes are observed at a time, and the toroidal mode numbers range from $n = 3$ to 6.
Magnetic oscillations with 70-140 kHz prior to type-I ELMs have been observed in ohmic and ECRH-heated discharges in COMPASS-D [10, 11] and, in the example presented, start at least 0.4 ms before the ELM. They propagate in the direction of the electron diamagnetic drift and are often composed of two beating modes. From the ratio of the plasma rotation to the mode frequencies, toroidal mode numbers $n = 4$ and 5 were concluded.
On DIII-D a general broadband fluctuation level increasing 30-50 ms before type-I ELMs is seen, but no coherent magnetic precursors seem to be observed [12]. Occasionally, some burst-like density fluctuations are seen [13].
On JT-60U coherent density fluctuations near the plasma edge with 10-25 kHz frequency could be measured with reflectometry [14]. They are observed prior to most type-I ELMs and start approximately 200-500 μs before the ELM. The oscillations could not be detected on the magnetics.
In JET low frequency modes ($\sim$15 kHz) preceding giant ELMs[1] have been reported in [15]. They are observed within a few ms of the D_α-spike and have

[1]The term 'giant' has not acquired a standardised meaning in the literature. Following [15] it is used at JET to denote bursts of D_α above a certain amplitude.

$n = 2$ and 4 in the example shown. Longer lived precursors at higher frequency ($f \sim 80$ kHz) and with high toroidal mode numbers (n = 3-12) are also observed [15, 16]. Although in [16] it is not explicitly stated whether the ELMs analysed are type-III or type-I/giant ones, this work is often cited in the context of type-III ELMs. However, Fig. 4 of [16] is devoted to a giant ELM, namely the same as Fig. 8 of [15].
In hot-ion H-mode discharges [17] giant ELMs were generally preceded by so-called Outer Modes [18], although they have not been explicitly labeled as precursors. Having low mode numbers (n mostly 1 or 2) and frequency ($f \sim$ 5-15 kHz), they could be very long-lived, occasionally existing up to hundreds of ms. Outer Modes have been identified as low-n external kinks [19].
Subsequent to the JET references cited above several improvements to diagnostics, data acquisition and MHD analysis codes were made. In this paper we will present and study in detail precursor activity found prior to type-I ELMs in general (not restricted to giant ones) on JET. The term "precursor" is used here in its more general definition to denote modes that systematically precede ELMs, while the term "trigger" is used to denote those modes whose growth rate rapidly accelerates prior to the ELM. ELM triggers are also ELM precursors, but ELM precursors do not have to be necessarily ELM triggers. The outline of this paper is as follows: Section 5.2 is devoted to the experimental observations for a class of lower frequency precursors observed, and the properties of lower and higher-n precursors will be compared in section 5.3. Section 5.4 gives an overview of the ideal MHD activity that, according to modelling calculations, can be expected at the plasma edge, and compares it to the experimental findings. Finally, a discussion of the results will be presented in section 5.5.

5.2 Experimental observations

5.2.1 Magnetic measurements

In the time window of Fig. 5.1 three type-I ELMs and a sawtooth crash occur. The first ELM is preceded by a shorter precursor ($\sim$ 2 ms), shown in the zoom view, while the second and third ELMs are preceded by more longlived precursors ($\sim$ 30 ms), which are difficult to see here. Compared to other MHD activity like internal kinks or NTMs, the precursors are much weaker and often hard to observe directly on the Mirnov signals. Fig. 5.2 shows the corresponding spectrogram, where the three precursors ($f \sim 18$ kHz) are marked by arrows. The first precursor can hardly be seen due to its short life. At their usual frequencies precursors shorter than 1 ms are difficult, or impossible, to discern on spectrograms due to the finite number of sampling points required for the Fourier analysis.
The toroidal mode numbers can be inferred from mode number spectra as shown

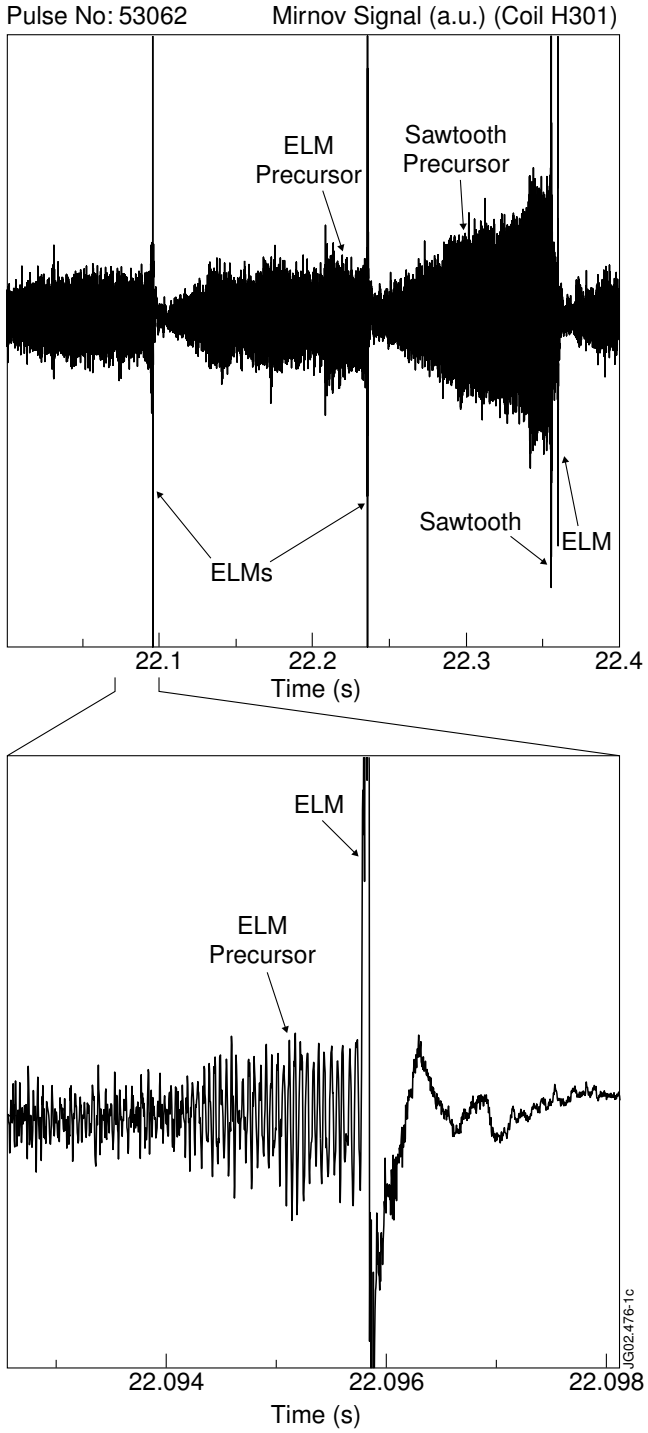

Figure 5.1: Mirnov signals of a coil located at the low field side for discharge 53062. The parameters of this discharge at the relevant time were: $B = 2.7$ T, $I = 2.5$ MA, $P_{\mathrm{NBI}} = 13.2$ MW (co-injected), $\overline{n}_{\mathrm{e}} = 7 \cdot 10^{19}$ m^{-3}, $\kappa = 1.75$, $\delta_{u/l} = 0.36/0.24$.

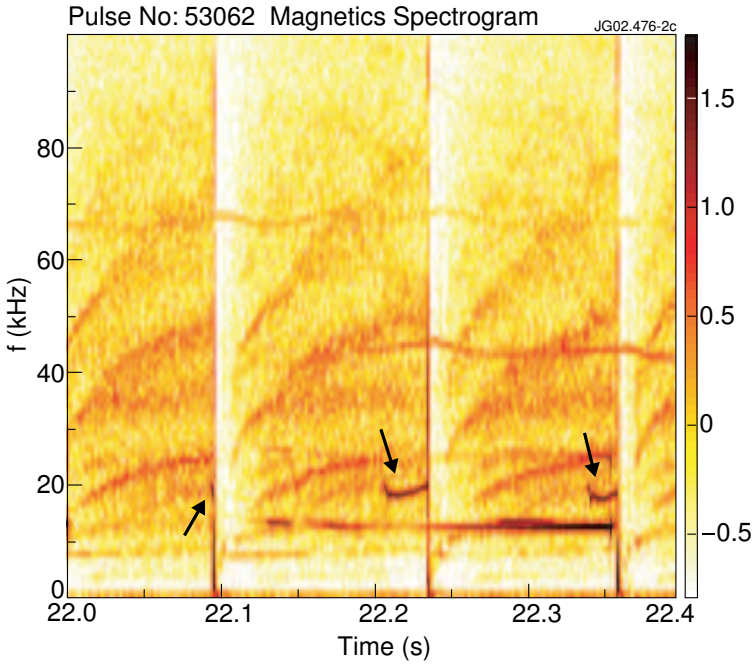

Figure 5.2: Magnetics spectrogram from a coil located on the low field side, with the precursors marked by the arrows. The stronger mode at 13 kHz is the sawtooth precursor. The numbers to the right of the colourscale denote the logarithm ($\log_{10}$) of amplitude, and are given in a.u.

in Fig. 5.3, where the colours denote the toroidal mode numbers n. By making a Fourier decomposition of a toroidal set of Mirnov coils and analysing the phase shift of the fluctuations the n-numbers can be obtained. For the analysis a high resolution array of 5 coils, with toroidal angles $\Delta\phi$ gradually increasing from 1.7 to 15.9 degrees, was used, adequate for mode numbers $n \leq 11$. A subset of the coils with lower $\Delta\phi$ was employed if higher mode numbers needed to be resolved or simply to check the correctness of previous calculations. The coils are positioned close to the plasma boundary, with $r_{\mathrm{coil}}/r_{\mathrm{sep}}$ being roughly 1.2, depending on the plasma shape. It proves very useful for finding hidden activity to plot the mode numbers in a spectrogram-like way due to its twofold filtering: in frequency- and in phase-space. This increases the contrast and makes it possible to discern modes faintly visible on the spectrograms. To reduce the noise level of the plots, points are discarded when the amplitudes are below a user defined threshold or the fitting error of the mode number exceeds a certain amount. Positive and negative mode numbers are detected. Modes with negative n rotate in the opposite direction to modes with positive n. The convention used here is that modes with negative n rotate in the direction of the electron diamagnetic drift. For the three ELMs shown the precursors have $n = +8$, and similar frequencies, despite their different duration. The range of toroidal pre-

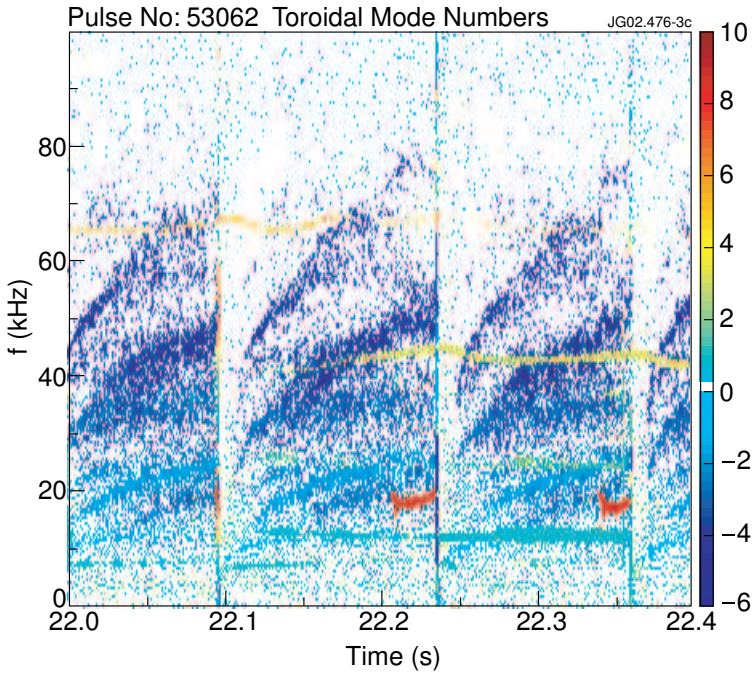

Figure 5.3: Spectrum of toroidal mode numbers n. For the three ELMs shown the precursors have $n = 8$ (red).

cursor mode numbers which have been observed is 1-13. Precursors with $n > 11$ are seen rather seldom, and precursors with $n > 13$ seem not to occur at all. The upper limit of observed precursor n-numbers is most likely physically real and not imposed by a diagnostic limitation. Although the radial damping rate of magnetic perturbations increases with increasing mode numbers, even precursors with very high $n \sim$ 11-13 could still be clearly discerned above the noise level on Mirnov signals. Therefore, it should have been possible to detect eventually occurring precursors with slightly higher $n \gtrsim 13$ on the magnetics if they would have been present. As noted above, the toroidal spacing of the coils used is easily capable of resolving higher toroidal mode numbers, and for example other edge MHD activity with $n =$ 15-20 has been detected.
In addition, one observes in Fig. 5.3 several broader bands of magnetic fluctuation with higher frequency ($f =$ 10-80 kHz) propagating in the direction of the electron diamagnetic drift (negative n), with n typically ranging from -1 to -8. These bands were already studied in [20] and named washboard modes. Washboard modes are plasma edge instabilities, and neither their origin nor their driving force are known. Resistive ballooning modes have been discussed as a possible candidate to explain their origin in [20]. The physics of washboard modes is beyond the scope of this paper, but, without going into much detail, it is worth noting that washboard modes and ELM precursors interact,

with the ELM precursors tending to inhibit the washboard modes. The physical mechanism behind this interaction could not be yet identified. For a detailed description of washboard mode dynamics and their consequences for the plasma edge the reader is referred to [21].
From the above example it could be seen that the time by which the precursor onset precedes the ELM event, and hence the precursor lifetime, varies greatly. The observed precursor lifetimes range from 0.2 ms up to several tens of ms, or even longer. Low n precursors generally start at least 10 or 20 ms prior to the ELM. Some cases have been observed where they start as early as a few hundred ms prior to the ELM. High n precursors tend to be more shortlived. They start typically a few ms up to a few tens of ms before the ELM. Since longlived precursors are easier to study with the diagnostics and have all other characteristics similar to shortlived precursors, use of them will be often made throughout the paper.
The analysis of the poloidal mode numbers m on the basis of poloidally distributed coils is more complicated. Due to the plasma toroidicity the apparent m number depends on the poloidal position of the coils (so called θ^*-effect [22,23]). Plasma shaping (elongation, triangularity) and the presence of an X-point impose further difficulties for modes located close to the plasma boundary. The X-point, in particular, can distort the poloidal mode structure considerably. Poloidal mode numbers determined by coils picking up magnetic fluctuations around the plasma midplane ($\theta = 0,\ \pi$) will then have the tendency to be lower than the real m-number of the mode. Only a limited numbers of coils, distributed poloidally around the plasma cross section, are available on JET. For the analysis 4 coils are used, two on the low field side (6 degrees apart), and two on the high field side (50 degrees apart). Due to aliasing effects the set of coils is not suitable for the analysis of modes with high m numbers, but for lower m ($\lesssim 6$) it has proved reasonably reliable for modes such as NTMs [24]. The procedure used for the analysis is described in more detail in Appendix B of [20]. For the ELM precursors with the lowest n ($n = 1$) the poloidal mode number analysis gives reproducible results, as summarised in Table 5.1. For each discharge one to three ELM precursors have been analysed. The resulting m-numbers were not found to change significantly within each discharge. The m-numbers obtained are comparable to, or slightly larger than, q_{95}, and thus correspond to rational surfaces located close to the plasma boundary.

5.2.2 Mode location and structure

The radial location of the precursors can be most easily determined through ECE measurements. JET's ECE system consists of 48 heterodyne radiometers sampled with 250 kHz, measuring slightly below the plasma midplane. The spacing between resonant measurement radii is typically only 1 or 2 cm. The precursors

Pulse no.	n-number	m-number	q_{95}
42578	1	4.3-4.8	3.8
42840	1	4.0-5.2	3.9
42870	1	3.4-3.8	3.8
43011	1	4.3-5.0	3.8
43021	1	3.5-4.0	3.4
43603	1	3.8-4.3	3.3
52010	1	3.3-3.8	2.9

Table 5.1: Values for the poloidal mode numbers m of ELM precursors with $n = 1$, obtained from the analysis of the phase shifts of fluctuations measured by four poloidally distributed Mirnov coils. The true m numbers of the modes must be integer numbers. Also given for each discharge is the safety factor at 95% of the poloidal flux, q_{95}, calculated by EFIT.

always occur near the separatrix, in the pedestal region. Fig. 5.4 shows a set of edge ECE signals for our previous example, and Fig. 5.5 shows the respective ECE profile and the location of the separatrix, with an uncertainty of approximately 1 cm, as calculated by the EFIT equilibrium code. The channels at $a - 5.0$ cm and $a - 3.9$ cm measure near the top of the pedestal (a = separatrix radius). The oscillations are most clearly seen 2.6 cm inside the separatrix, well inside the optically thick region, enhanced by the large temperature gradients in the pedestal. The temperature oscillations of the two longlived precursors prior to the second and the third ELM grow within 2 ms and then saturate in amplitude until 2 and 0.7 ms before the ELM, respectively. Then they begin to grow again, albeit with growth rates that are much smaller than in the first growth phase. The precursor prior to the first ELM is interrupted by the ELM already during the initial growth phase of the oscillations. In all three cases the temperature oscillations grow only roughly linearly in time when approaching the crash.

Concerning ECE channels further outward towards the separatrix one has to be cautious. When the density becomes too low, the plasma does not behave as a black body, and the radiation then detected at a given frequency can have contributions from different plasma regions (shine-through effect). The interpretation of the signal using a local model is then impossible. This shows up in the ECE profile, where the level of emission picked up rises again artificially (dotted part of the profile). Another complicating fact is that while it is difficult to locate the origin of the shine-through radiation picked up, the amount of shine-through itself is additionally modulated by the density oscillations caused locally by the mode, which reflectometry confirms to be present. The optical thickness τ has been evaluated in the cold plasma approximation (the formulas are given in [25],

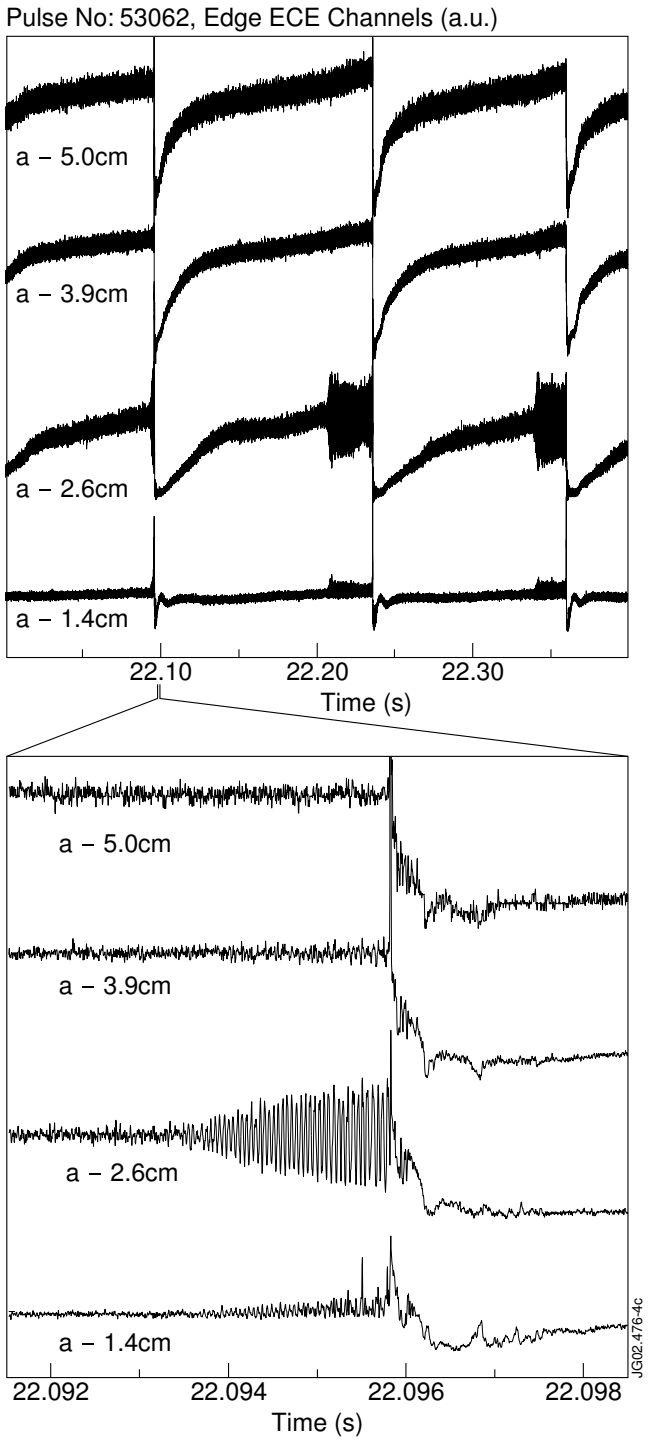

Figure 5.4: Edge ECE signals together with the distance of the measurement radii to the separatrix as calculated by EFIT. The second picture shows a zoom of the shorter precursor prior to the first ELM.

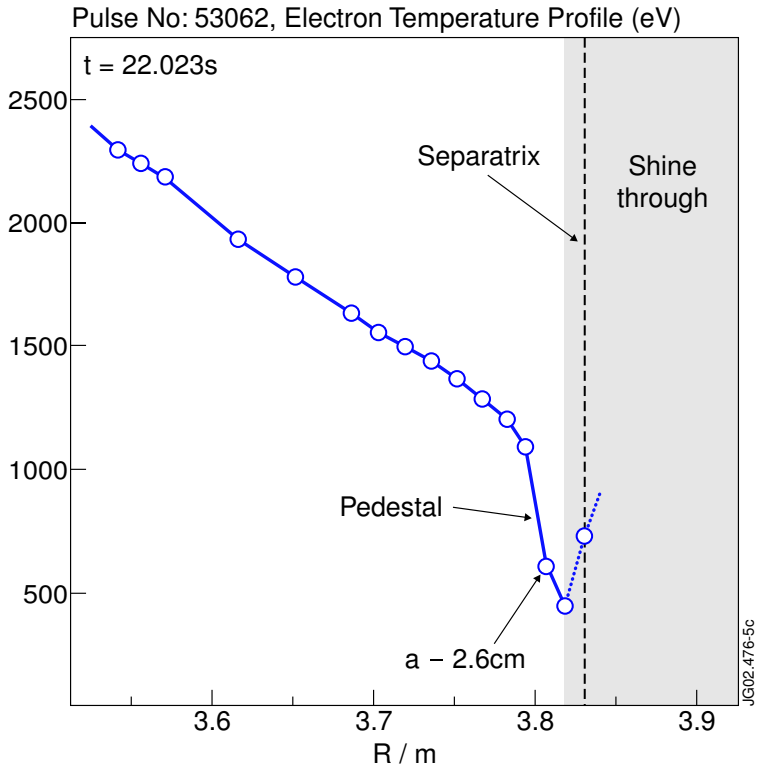

Figure 5.5: Electron temperature profile as measured by the ECE. The arrow marks the channel where the signal oscillations are most prominent on Fig. 5.4, supported by the large temperature gradients in the pedestal. The shine-through effect impedes a full coverage of the measurements out to the separatrix.

Tab. IV) for the channels resonant at $a-2.6$ cm and $a-1.4$ cm. The values obtained for τ strongly depend on the assumed shape of the edge density profile. At $a-2.6$ cm $\tau =$ 4-11, while at $a-1.4$ cm $\tau =$ 1.3-3.9. For optical thickness $\tau > 2$ is required. The marginal channel at $a-1.4$ cm is thus dubious and should be disregarded. Hence, only ECE data from channels measuring at optically thick radii is taken into account.

Fig. 5.6 shows results from the coherence analysis of a Mirnov signal with the edge ECE signals. The colour in the first two plots depicts the value of the coherence and the phase of the cross spectral density, respectively, as a function of frequency and distance to the separatrix. The coherence value increases towards the edge, and the phase shows no inversions across the radii, suggesting a kink-like mode, although this data could be produced as well by a magnetic island located between the last optically thick ECE channel and the separatrix. The values of the radial displacement shown in Fig. 5.6 are found to increase rather sharply at the edge, with displacements on the order of 1 cm. One can further see that for our $n = 8$ precursor the mode extent is not limited to $a-2.6$ cm,

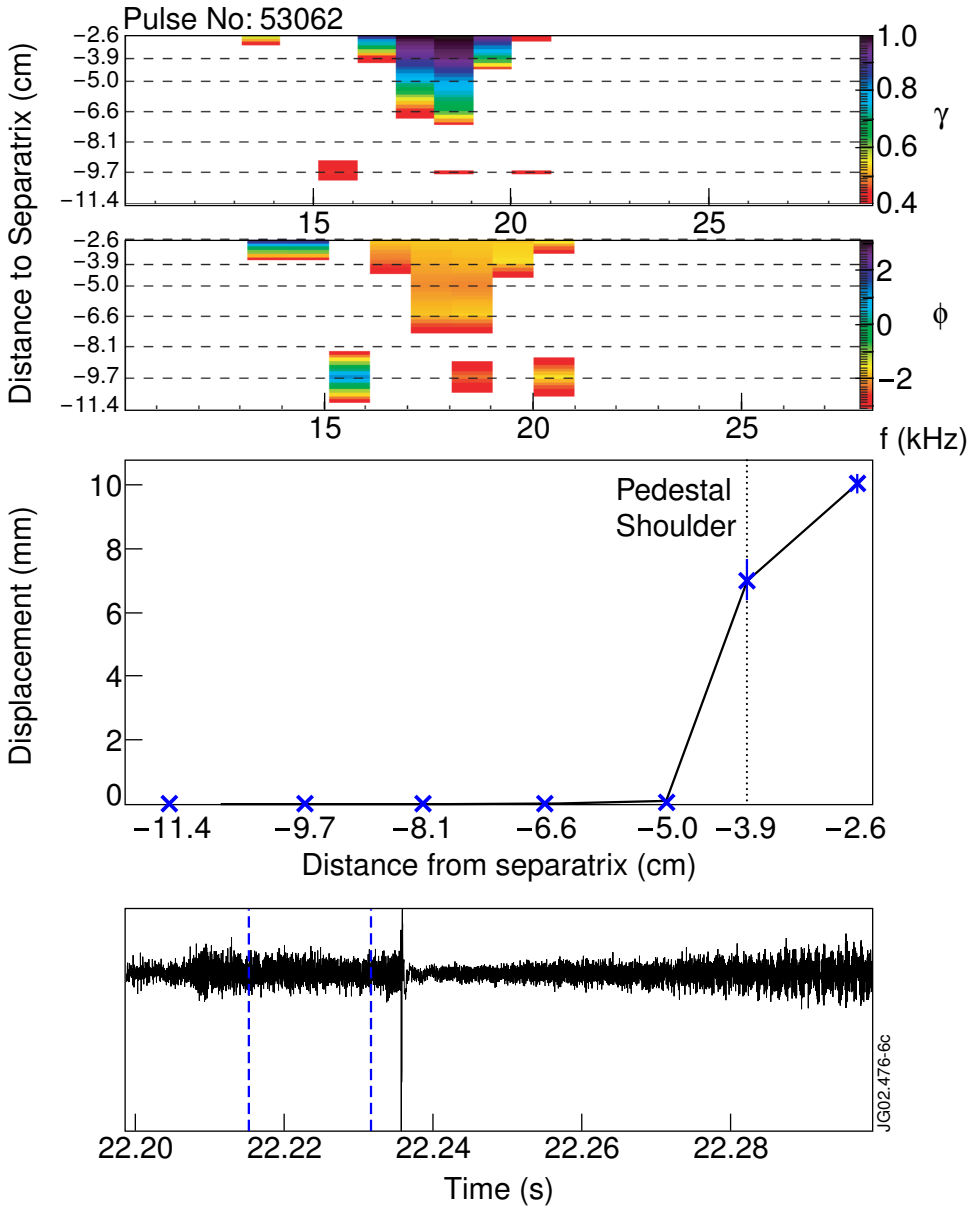

Figure 5.6: Coherence analysis of a Mirnov coil with the edge ECE channels. The first two plots give the values of the coherence and of the phase of the cross-spectral density, respectively, as a function of frequency and distance to the separatrix. The phase shows no variations with radius, suggesting a kink-like mode. The third window shows the magnitude of the radial mode displacement as a function of radius, and the fourth one shows the the Mirnov signal with the time interval used for the coherence analysis (within the dashed blue lines).

where the oscillations were clearly visible in Fig. 5.4. Large displacements also occur one channel further inwards, measuring at the pedestal shoulder, where the modest temperature gradient made them more difficult to observe directly on the ECE signal. The method used to obtain the displacement from the coherence analysis is described in appendix C of [20]. In general, the displacements observed typically range from 1 mm up to 1.5 cm.
The mode location is further verified by an edge reflectometer. JET's O-mode reflectometer system consists of 10 channels with cut-off densities ranging from 6.0 down to $0.43 \cdot 10^{19}$ m^{-3}, viewing the plasma from the low field side, near the plasma midplane. In general the modes are seen on all channels or a subset of channels with lower cut-off densities, depending on the discharge density. The fact that the modes are seen on the channels with low cut-off densities, measuring at pedestal radii that normally include radii where the ECE suffers from shine-through, indicates that the precursors indeed extend from about the pedestal shoulder, as seen from ECE measurements, until at least fairly close to the separatrix. Fig. 5.7 shows the fringe-jump corrected traces for an $n = 8$ precursor together with the distance of their reflecting layers to the separatrix. Lacking a possibility to measure fast density profiles at the edge, the cut-off radii have been estimated by taking the line-averaged density of the edge interferometer cord to be the density at the top of the pedestal, and then linearly extrapolating to zero density at the separatrix. Allowing for a finite density in the SOL would move the radii of the channels with lowest cut-off density further outwards, possibly outside the separatrix. The oscillations show no phase inversions between channels, confirming that the mode has a kink-like radial structure, i.e. twisting parity, and is not a magnetic island.
With the inserted filters very little information could be obtained from the SXR cameras due to their low response at the plasma boundary and the line-averaging. Only strong enough precursors could be faintly detected through spectrograms of channels looking towards the plasma edge, consistent with a mode localised in the plasma periphery. For a camera viewing the plasma laterally from the low field side, comparison of channels looking towards the top and bottom of the plasma (tangentially towards the same flux surfaces) yielded no evident up-down amplitude asymmetry.
Finally, the precursor occurrence is normally accompanied by a slight increase of D_α-emission (Fig. 5.8). The increased D_α could arise from a small increase in particle and/or energy transport across the pedestal associated with the precursors.

5.2.3 Further properties

The precursors are variable in the sense that they might grow and shrink repeatedly before the ELM or change their dominant n-numbers and frequency rapidly,

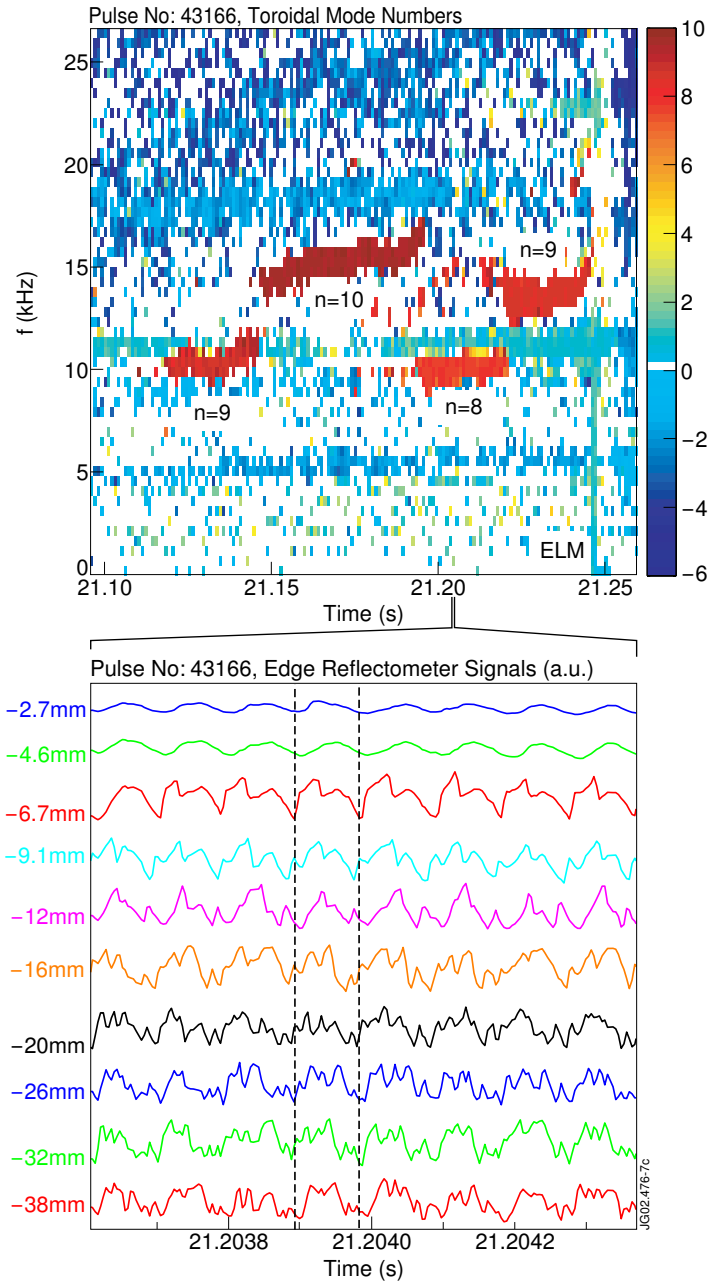

Figure 5.7: Toroidal mode numbers showing a sequence of precursors preceding an ELM, and traces of the 10 edge reflectometer channels showing the oscillations corresponding to the $n = 8$-precursor. Together with the traces, the estimated radii of the reflecting layers relative to the separatrix radius are given. The cut-off densities range from $0.43 \cdot 10^{19}$ m^{-3} (uppermost channel) to $6.0 \cdot 10^{19}$ m^{-3} (lowermost channel). No phase inversions are observed across the radii. The dashed lines are to guide the eye.

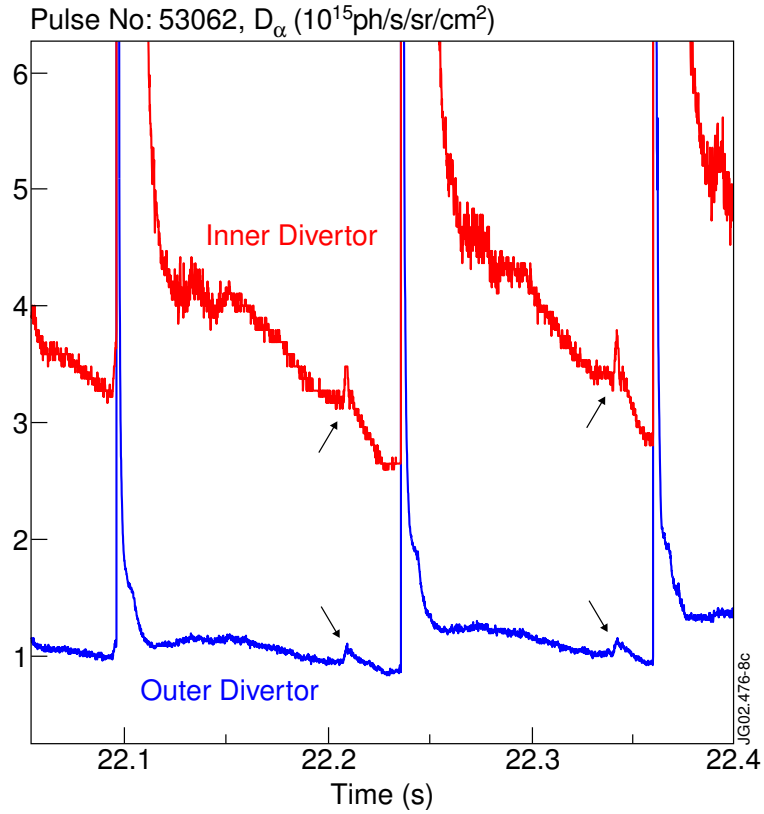

Figure 5.8: Inner and outer divertor D_α-signals for the example of Fig. 5.2. The arrows point at the time of the precursor onset.

at first sight without an apparent cause, that is, with no major changes in the main plasma parameters. Fig. 5.9 shows an example for the change in amplitude, where the n-spectrum and ECE signals show long intermittent $n = 7$ (orange) precursors at 10-15 kHz prior to two type-I ELMs at 21.1 s and 21.34 s. Between 21.0-21.1 s and 21.2-21.35 s the plasma current increased marginally from 2.49 to 2.53 MA, recovering the current lost by the preceding ELM, but whether this is really responsible for the mode behaviour in this particular case remains unclear. One can see that this behaviour is restricted to the plasma edge, the core MHD activity (e.g. a sawtooth precursor at 12 kHz and a 4/3 mode around 32 kHz) remains unperturbed. At ~ 45 kHz one can observe a further mode with similar frequency behaviour and higher $n \geq 10$ (for modes with higher mode numbers than given in the scale the colour of the mode saturates at the highest colour of the scale). A separate analysis with a reduced set of coils to resolve higher mode numbers yielded $n = 11$-13.
Fig. 5.10 shows an example in which the dominant precursor mode numbers change spontaneously within approximately 500 μs: starting with $n = 9$ (15 kHz), the dominant precursor becomes $n = 7$ (8 kHz) and finally $n = 5$ ($\sim$1

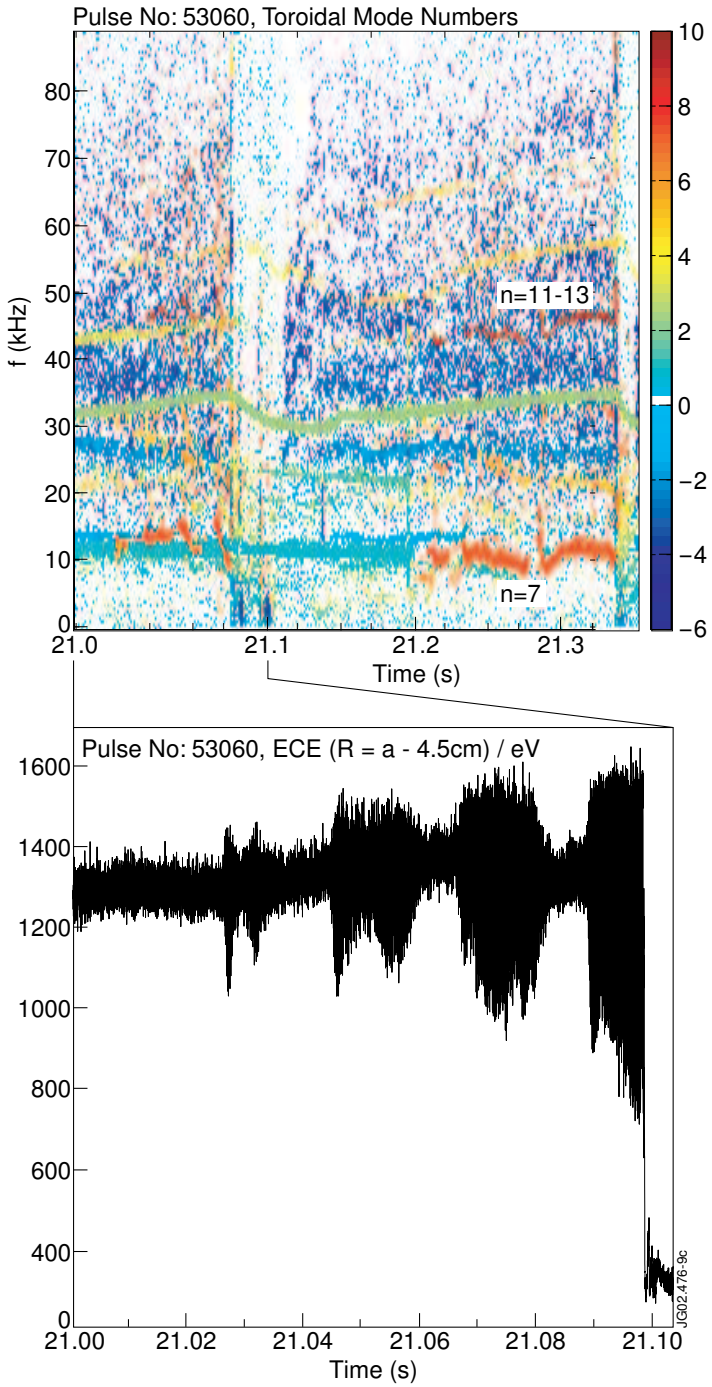

Figure 5.9: Toroidal mode numbers and ECE emission 4.5 cm inside the separatrix (near the pedestal top) showing intermittent $n = 7$ (orange coloured) precursor modes at 10-15 kHz prior to two type-I ELMs at roughly 21.1 s and 21.34 s, respectively.

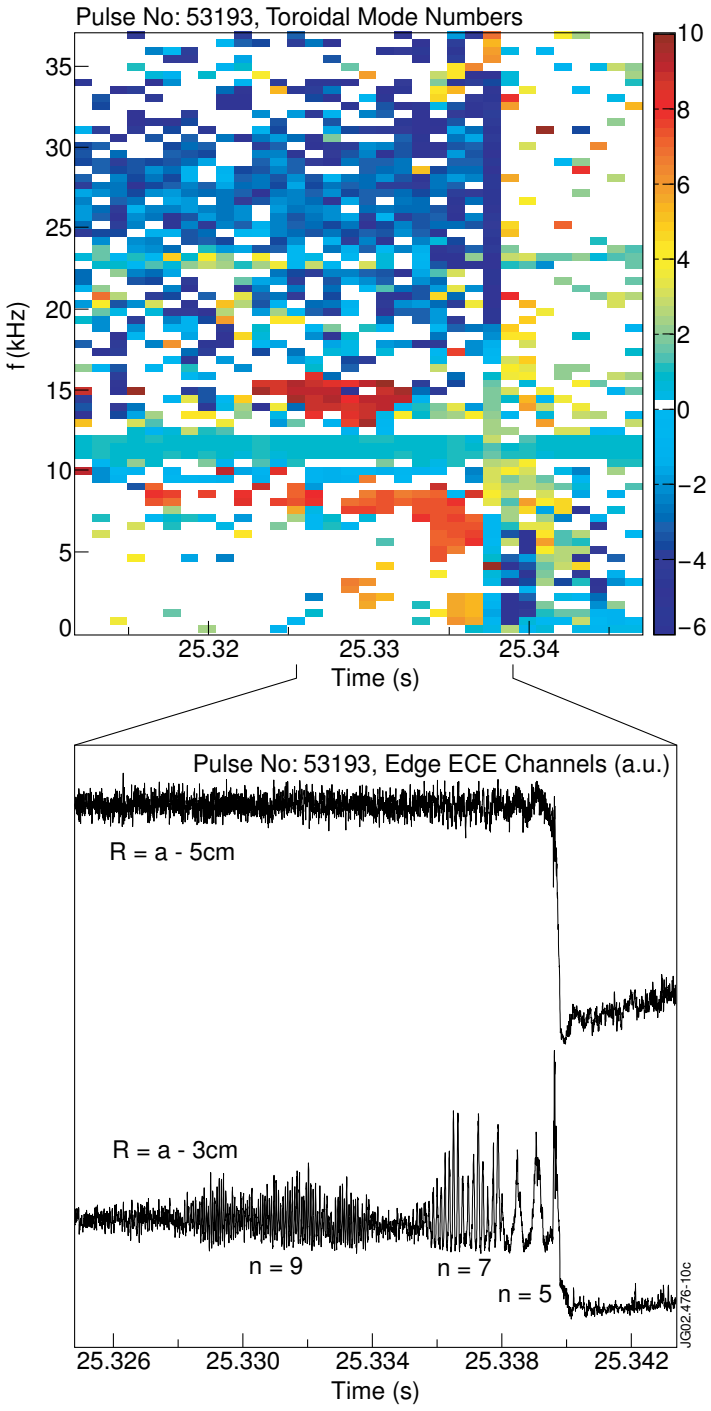

Figure 5.10: Toroidal mode numbers and ECE emission 5 cm (near the pedestal top) and 3 cm (region of steep gradients) inside the separatrix, respectively, showing a rapid change of dominant precursors. The continuous mode at 12 kHz is a sawtooth precursor.

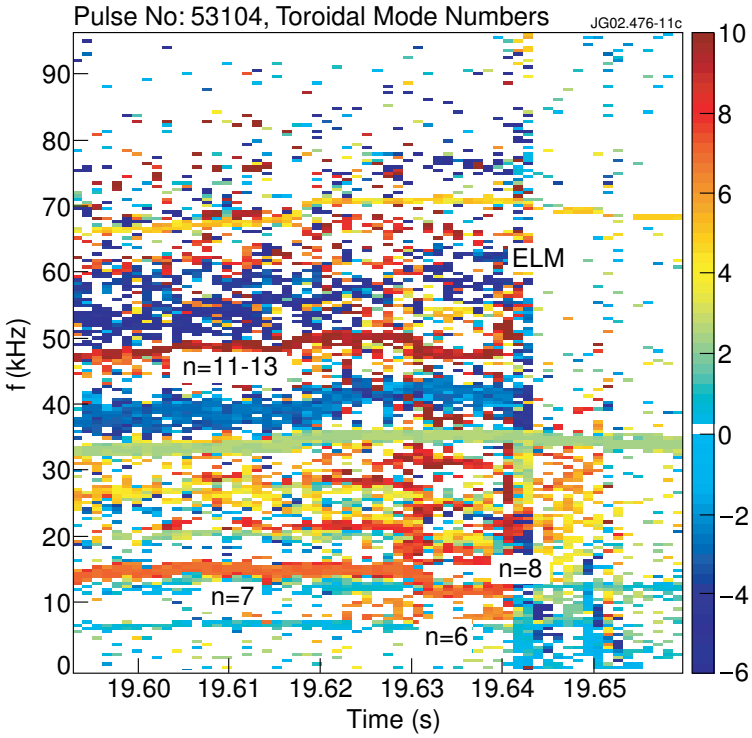

Figure 5.11: Toroidal mode numbers for an example showing multiple precursors. Also visible is a continuous 4/3 mode around 34 kHz triggered at an earlier time.

kHz). In spite of being observed at similar radii, the observed precursor frequencies are not proportional to their n-numbers. Considering the limited spatial resolution of the ECE measurements, the most likely explanation is that the various precursors differ slightly in their mode location and structure, and that this might indeed play a role in the final propagation frequency in a plasma region where changes in gradients and/or rotation velocities are expected to occur on a very short scale length.

Sometimes it happens that multiple precursors precede an ELM. An example is shown in Fig. 5.11 where a whole range of modes could be detected. One can distinguish precursors with $n = 6$ ($\sim$ 9 kHz), $n = 7$ (the very longlived mode around $\sim$ 13 kHz), $n = 8$ ($\sim$ 18 kHz) and at sligthly higher frequencies further modes with $n = 9$ and 10. Around 50 kHz one sees a further very long lasting mode with unusually high mode number and frequency, for which a separate analysis with a reduced set of coils yielded $n = 11$-13. Further analysis revealed that the $n = 7$ mode dominates over a long time, but becomes weaker shortly before the ELM. Simultaneously, the $n = 8$ mode becomes dominant until finally the ELM occurs. The other modes turn out to be much weaker.

In general, the observations described above suggest that there is a whole pool

of mode numbers available to the ELM precursors, which can be explained by the closeness of rational surfaces due to the high magnetic shear near the separatrix. It seems that some minor local parameter modifications in the plasma periphery are sufficient to stabilise or destabilise individual modes and to change their frequency or the most unstable mode numbers.
It is difficult to say whether the precursors interact or not. Several cases like the one above have been observed where the weakening of one precursor was followed by the appearance or growth of another one, as if the modes were competing amongst themselves trying to inhibit each other. Alternatively, this could again be explained by spontaneous minor radial shifts of the mode rational surfaces, always possible as the current magnitude and distribution are not ideally constant, with respect to the radii with largest driving forces, namely pressure and/or current gradients. On the other hand, cases have been found where at least two precursors with comparable amplitude coexist with no signs of interaction. In any case, the present data does not suggest that ELMs originate from a nonlinear coupling or mutual reinforcement of this kind of precursors.

5.3 Comparison of low-n and high-n modes

In the previous section it has been mentioned that the precursor mode numbers cover a wide range from n = 1-13. Precursors with low n = 1-3 were regularly observed in so-called hot-ion H-mode discharges [17], and are seen in some conventional ELMy H-mode discharges as well. Hot-ion H-modes are characterised by very high ion temperatures achieved by applying NBI heating to a low density target. The low n modes occurring in them were not explicitly labeled as ELM precursors, and have been named Outer Modes (OMs) [18] due to their localisation at the plasma boundary. The situation is that not all OMs ended with an ELM, but ELMs were generally preceded by OMs. By analysing the phase and amplitude behaviour of the oscillations detected on multiple SXR channels and comparing them to modelling results, OMs have been identified as low-n external kinks [19]. Although there is a priori no sharp boundary in the transition from low to high n-numbers that would suggest the higher n precursors to be of a different nature; strictly speaking only the low n-modes are experimentally known to be external kinks. This makes a comparison of low-n with intermediate and higher-n precursors particularly interesting. It was not possible, however, to repeat the analysis procedure of [19] for higher-n precursors. Many of the SXR diodes have suffered radiation damage in the D-T campaign, and the precursor oscillations in the remaining SXR channels were too faint (in contrast to the OM cases used by that time, which benefited from very high edge temperatures).
The characteristic rise in the level of D_α-emission has been often used in the past as a characteristic feature to identify the occurrence of OMs. This D_α-rise is qualitatively similar to that observed for higher-n precursors, already shown

in Fig. 5.8.
As an example for low-n precursors, two giant ELMs with their respective OMs are depicted in Fig. 5.12, including a Mirnov signal and its respective spectrogram, as well as the spectrum of toroidal mode numbers. The precursors are composed of a dominant $n = 1$ component with up to ten or twelve harmonics, which is usually regarded as a sign of high (poloidal or toroidal) localisation. It has been observed that with increasing precursor n-numbers the number of harmonics decreases systematically. For instance, precursors with dominant $n = 2$ are usually composed of four or five harmonics, $n = 4$ precursors have mostly an $n = 8$ harmonic, and precursors with $n \geq 5$ usually do not show additional harmonics. Linked to this, the signal oscillations associated with lower-n precursors are, compared to higher-n precursors, much less sinusoidal.
Fig. 5.13 shows the radial displacement profile of an $n = 1$ precursor, together with the position of the pedestal shoulder, obtained with the same procedure as for the $n = 8$ precursor in Fig. 5.6. The remarkable difference compared to the $n = 8$ precursor is that the mode width of the $n = 1$ precursor does not extend as far as the pedestal shoulder, or even further into the plasma, but that the large displacements only occur within the pedestal radii, that is, further outwards. This could be due to the limited resolution of the ECE diagnostic, but since this pattern occurred systematically in several other cases, it seems that low-n modes have a narrower extent with respect to the width of the transport barrier compared to higher-n modes.
Fig. 5.14 shows Fourier spectra of signals from a low field side and a high field side Mirnov coil for the case of a low n precursor (a) and a high n precursor (b). For each discharge the distance of the two coils to the separatrix on the low and on the high field side is comparable ($\sim$ 16 cm in (a), $\sim$ 21 cm in (b)). For the main component of the $n = 1$ precursor the ratio of measured inboard/outboard amplitudes is small, about 1.75. For the $n = 8$ precursor this ratio is very high, roughly 30. This initially suggested that precursors with low $n = 1$ or 2 have no strong ballooning character, as is expected for external kinks, while with increasing n-numbers the ballooning character of the modes increases. There is however an effect that needs to be considered in interpreting the data and imposes an artificial inboard/outboard asymmetry of the magnetically measured signal amplitudes even for modes that do not have ballooning character: In the cylindrical approximation the mode-induced magnetic fluctuations radially decay with $(r_{\mathrm{mode}}/r_{\mathrm{coil}})^m$, where m is the poloidal mode number of the mode. Within this approximation, the radial decay of the fluctuations is therefore equally strong on the low and the high field side. If the mode itself does not have ballooning character, then coils on the low and high field side pick-up fluctuations of equal amplitude. In toroidal geometry, however, the poloidal structure of modes is distorted compared to the cylindrical case: The local poloidal wavenumber k_θ of the mode is higher on the high than on the low field side (e.g. tearing mode's O- and

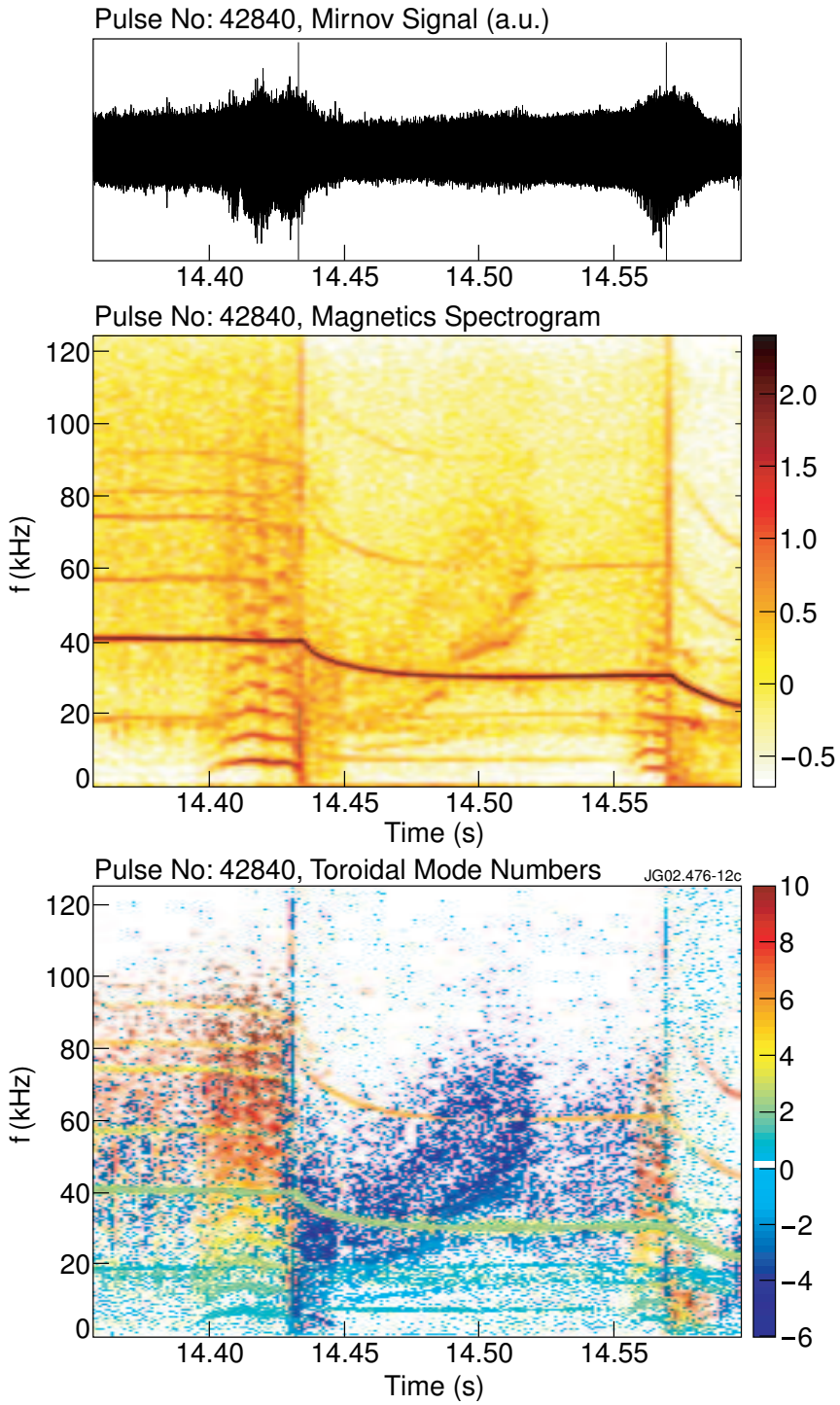

Figure 5.12: Mirnov signal of a low field side coil, the corresponding spectrogram, and the spectrum of toroidal mode numbers showing two external kinks. The continuous mode with initially 40 kHz is a 4/3-mode. Like the higher-n precursors, external kinks propagate in the direction of the ion diamagnetic drift.

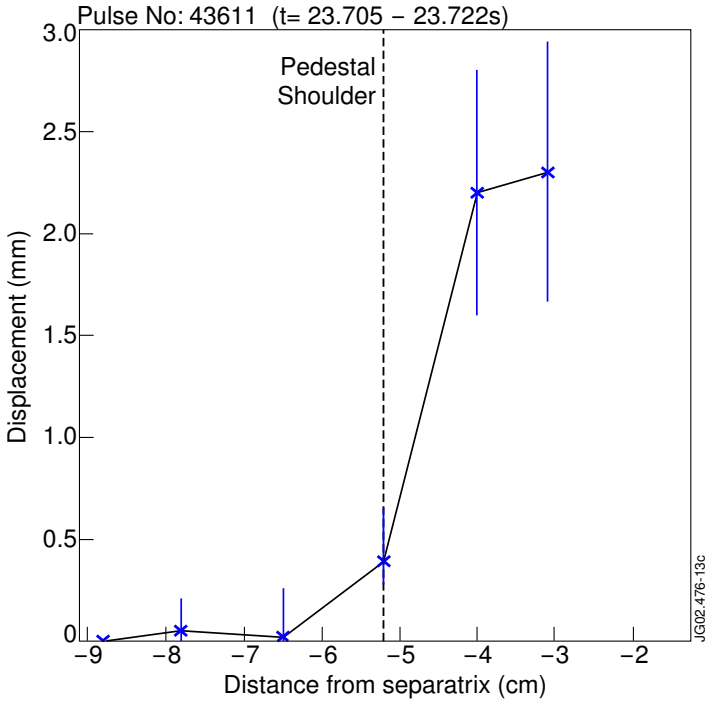

Figure 5.13: Radial displacement profile of an $n = 1$ precursor together with position of the pedestal shoulder. Relative to the width of the transport barrier, lower n modes are narrower than higher n modes.

X-points are not distributed poloidally equidistant, but closer to each other on the high field side). The result is that the mode-induced magnetic fluctuations on the high field side are subject to a stronger radial decay due to the higher "local m" compared to the fluctuations on the low field side. The differing radial decay unavoidably introduces an artificial inboard/outboard asymmetry of the magnetically measured mode amplitudes. For modes with low m-numbers the effect is not important because the ratio $(r_{\mathrm{mode}}/r_{\mathrm{coil}})$ is usually close to one in JET. This is further corroborated by the behaviour of the harmonics of the $n = 1$ precursor in Fig. 5.14a: Although the lower n components show nearly no difference in amplitude on the low and high field side, the difference in inboard/outboard amplitudes gradually increases with the harmonics' mode numbers, and becomes very pronounced for the higher harmonics. The effect makes it very difficult to check for the ballooning character of modes through direct comparison of low and high field side Mirnov signals.
A rough estimate can be made by following a similar technique than used in [26]. One assumes a field aligned perturbation with $\vec{k} \cdot \vec{B} = 0$, and obtains for the ratio

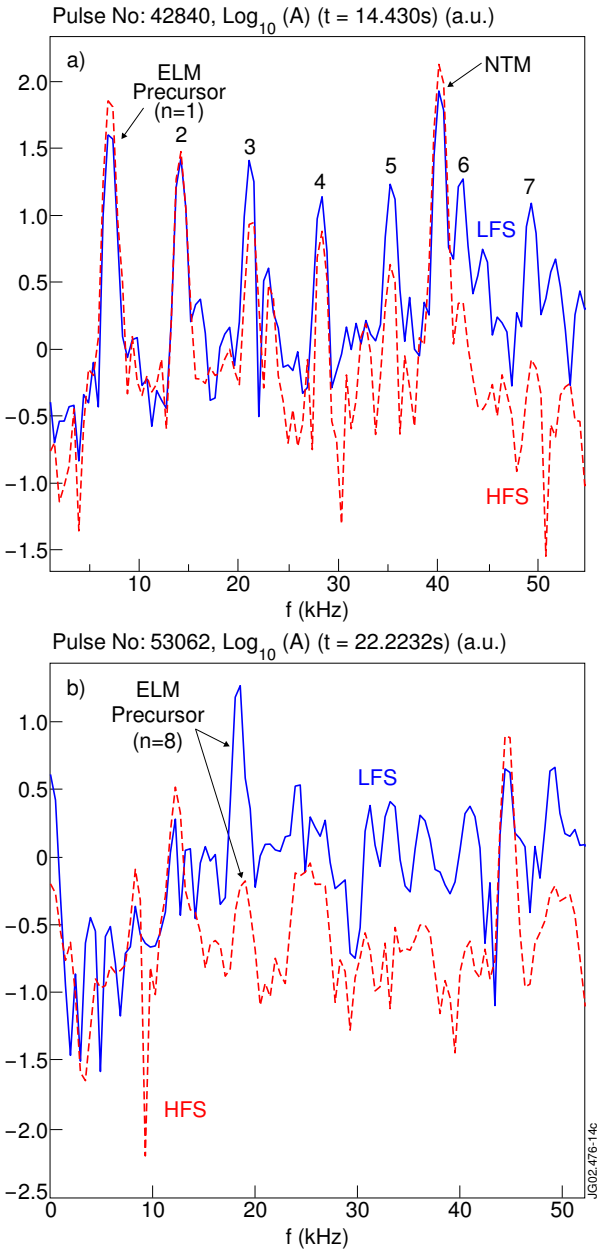

Figure 5.14: Logarithmic Fourier spectra of signals of a low and a high field side Mirnov coil with comparable distance to the separatrix a.) for one of the $n = 1$ precursors of Fig. 5.12 (where the numbers given denote the n numbers of the harmonics of the precursor), and b.) for one of the $n = 8$ precursors of Fig. 5.2. For the $n = 8$ precursor the ratio of measured amplitudes on the low and high field side is roughly 30, while for the fundamental component of the $n = 1$ precursor this ratio is only ~ 1.75. In spite of this low asymmetry, for the harmonics of the $n = 1$ precursor the measured inboard/outboard amplitude asymmetry gradually increases with increasing harmonics' mode numbers.

of poloidal wavenumbers of a mode the following expression

$$\frac{k_{\theta_2}}{k_{\theta_1}} = \frac{B_{\theta_1}}{B_{\theta_2}} \left(\frac{R_1}{R_2}\right)^2$$

Using EFIT a ratio of wavenumbers on the high/low field side of ~ 3.4 is estimated for the case of Fig. 5.14b, which, for high enough m, can indeed lead to signal amplitude asymmetries comparable to the ones measured.
In order to verify the above considerations, modelling calculations have been performed with the MISHKA code [27]. The calculations assess the MHD mode propagation in the vacuum region using real JET geometry, and taking into account the coordinates of the Mirnov coils. The JET vessel is considered to be ideally conducting, and the discharge shape is obtained from EFIT. Low and high-n cases have been studied. The poloidal distortion of the modes is found to cause a different radial decay on the low and on the high field side that agrees quantitatively very well with the above considerations. So, in contrast to what has been presumed in [28], and lacking an accurate enough estimate of the poloidal mode number m of the precursors, it has to be concluded that the magnetic data does not clarify whether the high n modes really have ballooning character or not. The observed difference in inboard/outboard signal amplitudes could well originate from the effect discussed above. It has to be emphasized that the above considerations are of general relevance, and should be taken into account whenever magnetic fluctuations picked up on the low and high field side want to be compared.
Initial studies to determine parametric dependences of the precursor mode numbers on local quantities have been performed. The precursor mode numbers are found to be mainly prescribed by the edge densities and temperatures. Fig. 5.15a shows their distribution in n_e-T_e-space. The line-averaged electron density has been measured through interferometry using a vertical cord that views the plasma edge on the low field side, while the value for T_e is taken at the pedestal shoulder and measured via ECE. For the study of parametric scalings data from 56 discharges has been used. The discharges cover a wide range in parameter space, with B = 2.4-3.9 T, I = 2.0-4.0 MA, q_{95} = 2.85-5.2, δ = 0.22-0.47, and P_{NBI} = 8-17 MW (sometimes also combined with ICRH). Each point in the plot corresponds to an ELM precursor. If several precursors occurred prior to an ELM, the dominant one has been selected, while in cases with a fast succession of precursors the first one has been taken (this convention has been adopted to exclude possible nonlinear effects arising from the preceding precursor). Alternatively, one may plot the mode numbers versus the pedestal pressure and the (normalised) electron collisionality ν_e^* (Fig. 5.15b), where $\nu_e^* = 0.012 n_{e20} Z_{\mathrm{eff}} q_{95} R/(\epsilon^{3/2} T_{e\mathrm{keV}}^2)$, taking $Z_{\mathrm{eff}} = 2$. There is a gradual transition from low to high n-numbers with increasing pedestal collisionality. The pedestal collisionality determines the amount of bootstrap current for given

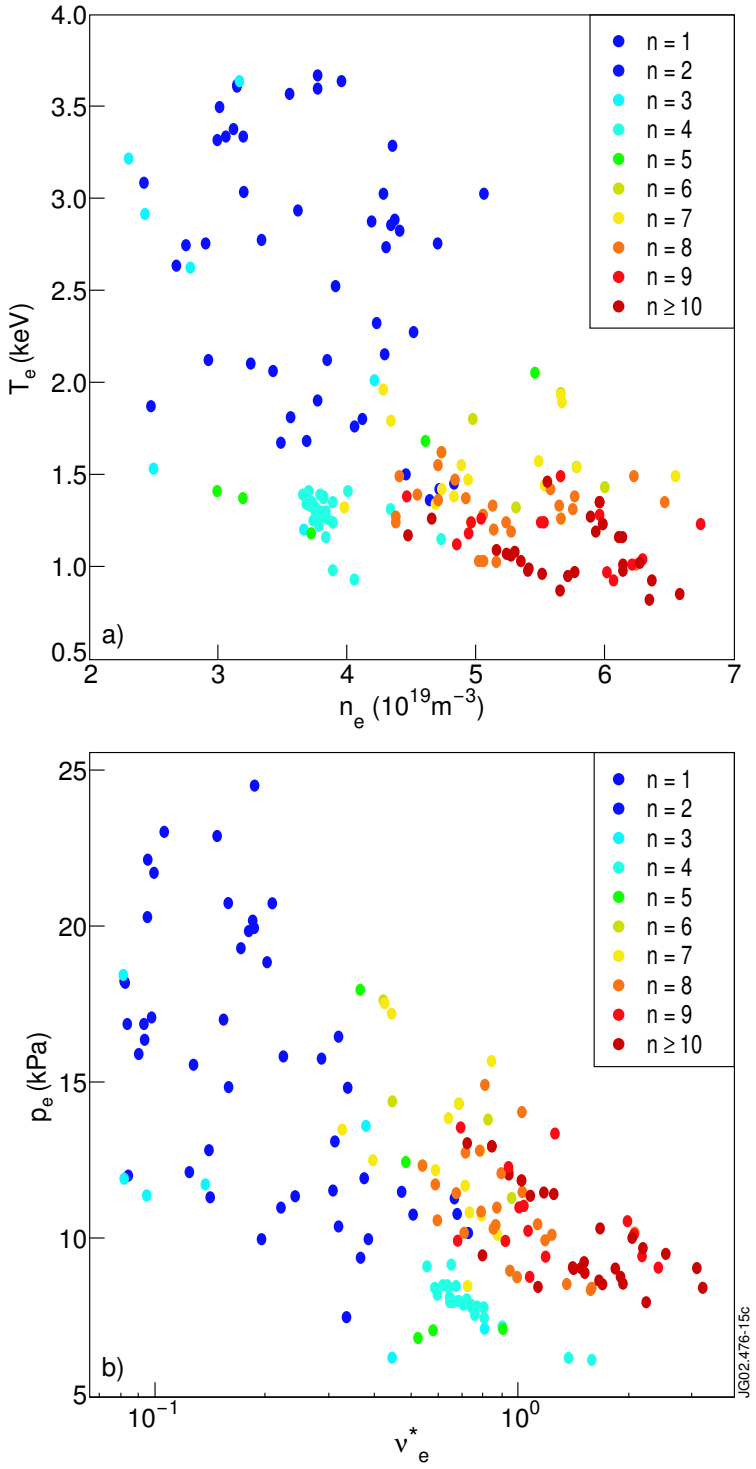

Figure 5.15: Precursor n-numbers as a function of a.) electron temperature near the pedestal top and edge line-averaged density, and b.) electron pedestal pressure and normalised electron pedestal collisionality. The data shown includes precursors of 1 ms to 150 ms of duration.

pedestal gradients [29], with increasing collisionality leading to reduced bootstrap current. This data suggests the mode numbers to be determined by some interplay of the pressure gradient and the edge current driving force. One can see in Fig. 5.15b that keeping the pedestal pressure fixed and decreasing the collisionality (increasing edge current) leads to lower mode numbers, while increasing the edge pressure keeping the edge current fixed (which implies simultaneously raising the collisionality) raises the mode numbers. In both cases the transition from low to high n-numbers occurs in a relatively narrow region of parameter space. For low enough collisionality (high enough current) only low mode numbers were observed, independently of the pressure. On the other hand, in discharges with sufficiently high edge collisionality (roughly $\nu_e^* >$ 1-3, depending on the discharge configuration) the precursors seem to be absent, indicating that a sufficiently high edge current is important to destabilise the precursors. The observed parameter dependence cannot be explained by considering only pure external kinks/peeling modes. Further types of instabilities need to be included.
It is worth comparing the experimentally observed parameter dependence with theoretical predictions. Some recent work has been performed on the exploration of the relationship between the calculated unstable toroidal mode number of edge instabilities and the edge density, edge collisionality and bootstrap current [30–32]. The ELITE code [33], in conjunction with the low n stability code GATO [34], has been used. The work highlights the importance of the edge current density for the edge MHD stability. In [30], inclusion of current in studies of the pedestal leads to a separate dependence of MHD stability on density and temperature, rather than just pressure, because of the strong collisional dependence of the bootstrap current. This is in agreement with the experimental results presented here. The stability calculations have shown that pedestal currents play a dual role in the MHD stability, stabilising high toroidal mode number ballooning modes through reduction of the edge magnetic shear, while at the same time providing drive for intermediate to low n peeling modes. The result is that coupled peeling-ballooning modes at intermediate n are often the limiting instability. Similar trends have been obtained in [31, 32]. In [31], a decrease in bootstrap current leads to an increase in the n-numbers of the unstable coupled peeling-ballooning modes. In [32], a set of discharge equilibria with varying density is studied. At low density, the edge bootstrap current stabilises the higher n peeling-ballooning modes, which allows the lower n modes to dominate the instability. At high density, and collisionality, the higher n modes are no longer stabilised and become dominant before the lower n modes can grow. These trends are consistent with the experimentally observed parameter dependence presented here.
The pressure-current dependence indicated by the experimental data might open the possibility to change the precursor mode numbers actively by in-shot current ramps. Furthermore, it is worth noting that the onset of OMs could be delayed

through a slow current ramp down, thus decreasing the edge current, once the H-mode phase was established [35].
The data shown in Fig. 5.15 includes precursors of 1 ms to 150 ms of duration. A separate treatment of shortlived (< 5 ms) and longlived (> 5 ms) precursors yielded no evident difference in their respective edge density, edge temperature and edge collisionality. Hence, the time by which the precursor onset precedes the ELM seems not to be related to those parameters.
To date no evident dependence of the precursor mode numbers on the plasma triangularity could be identified. Further parametric studies are anticipated.

5.4 Modelling results

To gain insight into the stability limits of the plasma boundary in H-mode regime in JET extensive numerical simulations have been performed. As starting point for the calculations the JETTO code is used [36], whose equilibrium module takes into account the H-mode transport barrier. It calculates the edge magnetic surfaces self-consistently with the edge pressure gradient and the edge current density, including the bootstrap current contribution. The formulas employed to calculate the bootstrap current can be found in [29]. The pedestal width is a free parameter chosen to match the experimentally observed pressure at the pedestal top. Ideal stability limits are then calculated with the HELENA [37] and MISHKA-1 [27] codes by multiplying the edge pressure gradient and the edge current independently with a constant, keeping the total current and energy content of the plasma fixed. Diamagnetic effects and resistivity were not taken into account for the calculations presented here. The higher order (cubic) finite elements used in all codes allow accurate equilibrium/stability calculations from $n = 0$ up to very high toroidal mode numbers ($n \leq 50$). For each equilibrium the stability of $n = 1$, 2, 3, 4, 6, 8, 10, 12,... modes have been calculated, considering the JET vacuum vessel to be ideally conducting.
The instabilities found can be classified into three categories: ballooning modes (the most unstable ones having typically high $n > 10$), kink (peeling) modes (mostly low $n < 6$) and ballooning-kink modes (normally with medium n-numbers around 5 to 15). Due to their overlap, n-numbers on their own are in principle only of limited usefulness to classify the modes. The classification relies more on the driving forces and different mode structures as described below. Ballooning modes are driven by the pressure gradient, $\alpha = -\mu_0 p' q^2 / B_0^2 \epsilon$, and stabilised by shear, whereas kink (peeling) modes are driven by the edge current density and stabilised by pressure. Kink-ballooning modes are driven by both the pressure gradient and the edge current density.
Fig. 5.16 shows calculations for an ELMy H-mode discharge, where the stability limits for the different mode types are displayed. The coloured areas show the stability limits of infinite-n ballooning modes calculated by HELENA at different

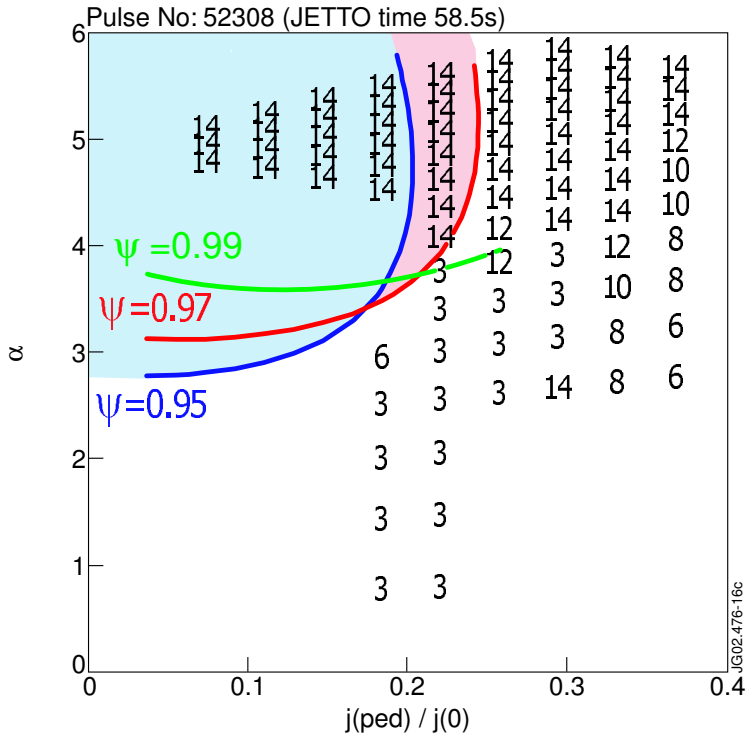

Figure 5.16: Stability limits for n = 1-14-modes (numbers) and for $n = \infty$ ballooning modes (coloured areas) for an ELMy-H discharge, as a function of the ballooning parameter α and the normalised edge current density.

values of the normalised poloidal flux function near the edge (ψ = 0.95-0.99). The numbers displayed in the plot have been calculated by MISHKA, and represent the n-numbers of the most unstable finite-n modes up to $n = 14$ at the respective α and edge current values. While there is some scattering in the distribution of the most unstable mode numbers, the general trend that is reproducibly encountered in the discharges analysed is to obtain high n numbers at high α, where the ballooning modes are expected, while at low α and finite edge current low n modes become destabilised. These correspond to kink modes. Intermediate n modes are often encountered in the proximity of both the kink and the ballooning stability limit, and in most cases belong to coupled peeling-ballooning modes. The variation in mode number near $\alpha = 3$ in Fig. 5.16 reflects the fact that high and low n growth rates become very similar in that region.
In practice, the observed mode number of the precursor will depend on the trajectory of the discharge in α and in pedestal current, and where it first crosses an instability boundary. Modes becoming unstable far beyond the instability boundaries are not likely to be encountered in the experiment anymore. Quantitative comparisons of modelling predictions with the mode numbers observed in the experiment are difficult due to limitations in the determination of edge

quantities such as the edge current density. They would further require detailed computations for each different case, which is beyond the scope of this paper. Here the aim is to make qualitative comparisons between theory and the observed precursors.
As mentioned above, the mode structures of the three types of instability differ significantly. Fig. 5.17a shows plasma cross sections with the poloidal mode structures of an $n = 20$ ballooning, an $n = 12$ ballooning-kink and an $n = 3$ kink instability, respectively. The ballooning mode shows the expected large asymmetry of the mode amplitude on the high and low field side, and has a relatively broad radial extent. The $n = 3$ kink has a comparable inboard/outboard mode structure, a much narrower extent, particularly around the midplane, and shows, in contrast to the ballooning mode, large and broad mode displacements concentrated around the X-point. The ballooning-kink mode shows a mixture of these properties, with a much larger amplitude on the low than on the high field side, broad radial mode extent and distinct displacements around the X-point.
Also in Fig. 5.17 the respective midplane radial displacement profiles are shown. The vertical line around $\sqrt{\psi} = 0.97$ denotes the position of the pedestal shoulder, which is held invariant as the edge current and pressure are scanned. Thus, the extent of ballooning and ballooning-kink modes is comparable to the width of the transport barrier, while the $n = 3$ kink is narrower. This is consistent with the experimental results presented in section 5.3. The kink-mode displacement increases sharply towards the separatrix, while the ballooning displacement peaks well inside it. Ballooning mode peak amplitudes occur at the position of maximum pressure gradient. Both ballooning and ballooning-kink modes are composed of several m-components, whereas the kink-mode shows only a small number of them.
As described in section 5.3, the experimental measurements confirm that lower-n precursors have a narrower radial extent compared to the higher-n precursors. This is consistent with the lower-n precursors being external kinks, and also suggests that the higher-n precursors are not pure external kinks but according to their mode width either peeling-ballooning or pure ballooning modes. In addition, the observed precursor n-numbers are mostly below $n = 10$, which according to modelling is rather too low for pure ideal ballooning modes. Hence, modelling results are consistent with the low-n precursors being ideal external kinks, while higher-n precursors are most likely ideal peeling-ballooning modes.

5.5 Summary and discussion

The properties of a class of type-I ELM precursors that is commonly observed in JET in ELMy-H discharges with coinjected NBI have been studied in considerable detail. Their characteristic features comprise: low frequency, mostly below 25 kHz; typical onset a few ms to a few tens of ms before the ELM crash; prop-

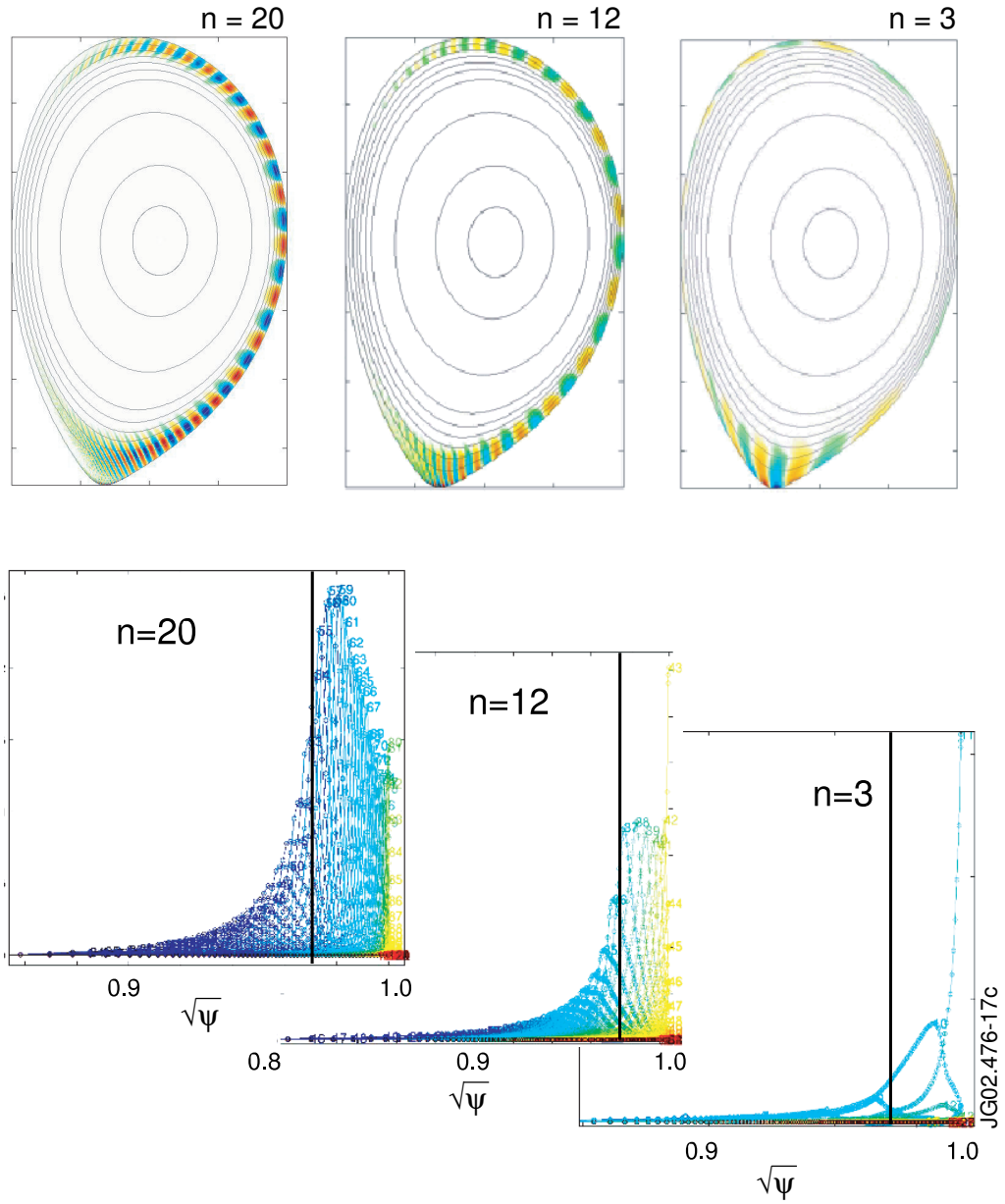

Figure 5.17: Poloidal structure of the radial displacements of an n=20 ballooning, an n=12 coupled ballooning-kink and an n=3 kink instability together with their midplane radial displacement profiles. Each curve corresponds to a poloidal component with its respective poloidal mode number m. The vertical lines denote the position of the pedestal shoulder.

agation in the direction of the ion diamagnetic drift; localisation in the pedestal region extending to the separatrix or beyond with no radial phase inversion; and a slight increase of the D_α-emission accompanying their occurrence. Radial mode displacements from 1 mm up to ~ 1.5 cm have been observed.
Due to the closeness of rational surfaces near the separatrix combined with the short scale length on which quantities like pressure gradient, edge current density, plasma rotation or influence of neutrals change radially, one can expect each mode to have a narrow instability window that may be easily disturbed. The observations made of multiple precursors at similar radii, sometimes changing their toroidal mode numbers and frequency with no obvious reason, suggest that this is indeed the case.
A range of mode numbers $n = 1$-13 has been observed, with the low-n precursors known to be ideal external kinks. A thorough comparison of low- and high-n precursors has been performed both in experiment and through modelling calculations and suggests the moderate-n precursors are coupled peeling-ballooning modes (and not pure ballooning modes, which occur at higher n). Pure peeling modes are precluded by the observation of the mode width, which is too broad for peeling modes, and because of the observed dependence of mode number on n_e and T_e (cf. Fig. 5.15). It rather seems that the precursor n-numbers are determined by some interplay of both the pressure gradient and the edge current density. Due to the absence of radial phase inversions tearing modes have to be excluded.
If the precursors are involved at all in the ELM cycle, they seem not to be the actual trigger for the ELM. This is concluded from the observation that the precursor oscillations do not grow exponentially into the ELM crash but mostly rather linearly. In fact, there is no evidence of the precursor mode growth rate rapidly accelerating before the ELM, and cases were shown where the precursor amplitude even remains nearly saturated. A further point that suggests that the ELM precursors do not trigger the ELMs has been previously given in [35]: The technique of current rampdown used to optimise the performance of hot-ion H-mode discharges was found to delay the onset of the low-n precursors (OMs) while making the ELMs appear earlier. ELMs were still preceded by the OMs in the current rampdown discharges, but the duration of the OMs was reduced compared to the discharges without current rampdown. This implies that the ELM trigger behaved differently to the OMs during the current rampdown, indicating that ELM precursor and ELM trigger are two separate phenomena. This and the large variation in the time by which the precursor appearance precedes the ELM could be explained in terms of the ELM event resulting from a combination of two instabilities. Within this picture a precursor mode starts once the stability limit for the first instability is encountered, but the ELM is not triggered until the stability limit for the second instability is reached. The model of the peeling-ballooning-cycle for type-I ELMs [38] points very much in

that direction. However, if one assumes ELMs to be finally triggered by a combination of kink- and ideal balloning-modes, at least in the particular case of discharges with low-n precursors the kink-limit is obviously reached *before* the ideal ballooning limit. This is in disagreement with the order of events predicted in the peeling-ballooning cycle originally proposed in [38]. A generalisation of the peeling-ballooning model with ELM cycles for which the kink/peeling boundary is encountered first has been recently proposed in [30].
On the other hand, the precursors seem to be absent in discharges with sufficiently high electron edge collisionality (strong gas puffed discharges) for which $\nu_e^* >$ 1-3 (depending on the discharge configuration), and also optimised shear discharges were reported where they could not be seen [39], raising the question whether the precursors are really linked to the ELM event. The absence of precursors in high collisionality discharges is not believed to be related to a diagnostic limitation. Although in many of these cases the ECE data are not available (making it difficult to find shortlived precursors, in particular), sufficiently longlived precursors should be still detectable through the magnetics. However, they have not been detected in spite of the considerable number of high density discharges analysed. This is in contrast to what is observed in discharges with low to moderate collisionality. Gas scans of discharges have been analysed in which the precursors still had relatively low n = 5-6 for a number of discharges at moderate fuelling rates, prior to their disappearance at the next highest density. The lack of precursors at high collisionality (low edge current) would be again consistent with their identity as ideal kink- or coupled ballooning-kink modes, and not ideal ballooning modes. A hypothesis that is supported by the overall data presented here is that the ideal ballooning modes, and not ideal kink- or coupled ballooning-kink modes, could provide the trigger for type-I ELMs. In this respect, certain theoretical works [40, 41] predict a general explosive feature of the ideal ballooning instability ("detonation") emerging from non-linear effects through the development of fine-scale substructures ("fingers"). In any case, the importance of the ELM precursors studied here relies in that they provide a valuable source of information to improve the understanding of ELM-cycles, and their further study certainly opens the possibility to validate, or refute, present ELM models.
The precursor phenomenon seems not to be restricted to JET. The precursors show similarities with the ones reported in [6–8, 14], particularly their low frequency and typical duration in the ms range, as well as the mode numbers reported in [6, 7].
A significant feature of ELMy H-modes in JET is the universally observed washboard modes [20]. The properties of these modes, which seem to significantly interact with the ELM precursors, will be discussed in a future paper [21].

Acknowledgements

This work has been performed under the European Fusion Development Agreement. One author (C. P. P.) wants to acknowledge the financial support of the Dutch Research Organisation NWO.

References

[1] Zohm, H., Plasma Phys. Control. Fusion **38** (1996) 105.

[2] Connor, J.W., Plasma Phys. Control. Fusion **40** (1998) 191.

[3] Connor, J.W., Plasma Phys. Control. Fusion **40** (1998) 531.

[4] Leonard, A. W., et al, J. Nucl. Mater. **266-269** (1999) 109.

[5] Janeschitz, G., J. Nucl. Mater. **290-293** (2001) 1.

[6] Suttrop, W., et al, Plasma Phys. Control. Fusion **38** (1996) 1407.

[7] Kass, T., et al, Proc. 24th EPS Conf. on Controlled Fusion and Plasma Physics (Berchtesgaden), vol. 21A, ed M. Schittenhelm et al (Geneva: EPS) part IV, p. 1521 (1997).

[8] Manso, M., et al, Plasma Phys. Control. Fusion **40** (1998) 747.

[9] Maraschek, M., et al, Proc. 25th EPS Conf. on Controlled Fusion and Plasma Physics (Praha), vol. 22C (1998), 492.

[10] Buttery, R. J., et al, Proc. 21th EPS Conf. on Controlled Fusion and Plasma Physics (Bournemouth), vol. 19C, part III, p. 273 (1995).

[11] Colton, A. L., et al, Plasma Phys. Control. Fusion **38** (1996) 1359.

[12] Zohm, H., et al, Nucl. Fusion **35** (1995) 543.

[13] Doyle, E. J., et al, Phys. Fluids B **3** (1991) 2300.

[14] Oyama, N., et al, Plasma Phys. Control. Fusion **43** (2001), 717.

[15] Nave, M. F. F., et al, JET Report JET-P(95)03.
Nave, M. F. F., et al, International Conference on Plasma Physics ICPP 1994 (Foz do Iguacu, Brazil 1994) AIP Conference Proceedings 345, American Institute of Physics 1995, p. 58.

[16] Ali-Arshad, S., et al, Proc. 19th EPS Conf. on Controlled Fusion and Plasma Physics (Innsbruck), vol 16C, part I, p. 227 (1992).

[17] JET Team (presented by Jones, T.T.C.), Plasma Phys. Control. Fusion **37** (1995) A359.

[18] Nave, M. F. F., et al, Nucl. Fusion **37** (1997) 809.

[19] Huysmans, G. T. A., Hender, T. and Alper, B., Nucl. Fusion **38** (1998) 179.

[20] Smeulders, P., et al, Plasma Phys. Control. Fusion **41** (1999) 1303.

[21] Perez, C. P., et al, 'Washboard Modes as ELM-related events in JET', submitted to Plasma Phys. Control. Fusion

[22] Merezhkin, V. G., Sov. J. Plasma Phys. **4** (1978) 152.

[23] Klueber, O., et al, Nucl. Fusion **31** (1991) 907.

[24] Buttery, R. J., et al, Nucl. Fusion **43** (2003) 69.

[25] Bornatici, M., Cano, R., de Barbieri, O. and Engelmann, F., Nucl. Fusion **23** (1983) 1153.

[26] Snipes, J. A., et al, Proc. 29th EPS Conf. on Controlled Fusion and Plasma Physics (Montreux), P1.057 (2002).

[27] Mikhailovskii, A. B., et al, Plasma Phys. Rep. **23** (1997) 844.

[28] Perez, C. P., et al, Proc. 29th EPS Conf. on Controlled Fusion and Plasma Physics (Montreux), P1.023 (2002).

[29] Sauter, O. and Angioni, C., Phys. Plasmas **6** (1999) 2834.

[30] Snyder, P. B., et al, Phys. Plasmas **9** (2002) 2037.

[31] Mossessian, D. A., et al, Plasma Phys. Control. Fusion **44** (2002) 423.

[32] Leonard, A. W., et al, Phys. Plasmas **10** (2003) 1765.

[33] Wilson, H. R., Snyder, P. B., Huysmans, G. T. A., and Miller, R. L., Phys. Plasmas **9** (2002) 1277.

[34] Bernard, L. C., Helton F. J. and Moore, R. W., Comput. Phys. Commun. **24** (1981) 377.

[35] Nave, M. F. F., et al, Nucl. Fusion **39** (1999) 1567.

[36] Cenacchi, G., Taroni, A., Rapporto ENEA RT/T1B 88 (5) 1988.

[37] Huysmans, G. T. A., et al, Proc. CP90 Conf. on Comp. Physics, ed. A. Tanner (World Scientific Singapore 1991), p. 371.

[38] Connor, J. W., Hastie, R. J. and Wilson, H. R., Phys. Plasmas **5** (1998) 2687.

[39] Alper, B., et al, Proc. 29th EPS Conf. on Controlled Fusion and Plasma Physics (Montreux), P1.025 (2002).

[40] Hurricane, O. A., Fong B. H. and Cowley, S. C., Phys. Plasmas **4** (1997) 3565.

[41] Fong, B. H., "Metastable and explosive properties of ballooning modes in laboratory and space plasmas", University of Princeton (1999), PhD thesis, available at http://www.asp.ucar.edu/∼bhlfong/thesis.pdf

Chapter 6

Washboard modes as ELM-related events in JET

This chapter is a reprint of an article published in Plasma Phys. Control. Fusion **46** (2004) 61-87.

Authors:
C P Perez[1,2], H R Koslowski[1], T C Hender[3], P Smeulders[4], A Loarte[5], P J Lomas[3], G Saibene[5], R Sartori[5], M Becoulet[6], T Eich[7], R J Hastie [3], G T A Huysmans[6], S Jachmich[1], A Rogister[1], F C Schüller[2] and JET EFDA contributors[a]

[1] Association EURATOM-Forschungszentrum Jülich, Institut für Plasmaphysik, Trilateral Euregio Cluster, D-52425 Jülich, Germany
[2] FOM-Rijnhuizen, Ass. EURATOM-FOM, TEC, PO Box 1207, 3430 BE Nieuwegein, NL
[3] EURATOM/UKAEA Fusion Association, Culham Science Centre, Abingdon, OX14 3DB, UK
[4] Associazione EURATOM-ENEA sulla Fusione, Centro Ricerche Frascati, C.P. 65, 00044-Frascati (Rome), Italy
[5] EFDA-CSU, Max-Planck-Institut für Plasmaphysik, Garching D-85748, Germany
[6] Association EURATOM-CEA, Cadarache, F-13108 St. Paul-lez-Durance, France
[7] Max-Planck-Institut für Plasmaphysik, EURATOM Assoziation, Garching D-85748, Germany

[a]See annex of J. Pamela et al, "Overview of JET Results", Fusion Energy 2002 (Proc. 19th Int. Conf. Lyon, 2002), IAEA, Vienna (2003).

Abstract. Washboard (WB) modes [Smeulders P *et al* 1999 *Plasma Phys. Control. Fusion* **41** 1303] are a very common edge instability regularly observed in the H-mode regime in JET. They are detected as (normally several) bands of continuously fluctuating magnetic activity rotating in the direction of the electron diamagnetic drift with typical frequencies in the range of 10-90 kHz. The time evolution of the WB mode frequency is found to follow qualitatively the evolution of the electron temperature measured near the pedestal top, probably due to the strong diamagnetic drift associated with the large pedestal gradients. Evidence for their involvement in the pedestal and ELM dynamics will be presented. Increasing WB mode amplitude is correlated with an increase in the time between consecutive type-I ELMs. In situations in which a sudden increase (decrease) of the WB activity is observed, the build-up of the pedestal temperature (and, linked to this, also of the pedestal pressure) of the electrons is seen to become slower (faster). This is a strong indication that the WB mode activity has a regulating effect on the pedestal, and that it is responsible for an enhanced transport of energy across the separatrix. The occurrence of a class of type-I ELM precursor modes commonly observed in JET in discharges with low to moderate collisionality ($\nu_e^* < 2$, roughly) [Perez C P *et al*, EFDA-JET Preprint EFD-P(02)11] is found to be associated with a weakening of the WB

modes. The underlying mechanism for this interaction has not been yet identified. In contrast to low triangularity discharges, WB activity is found to increase with gas puffing at high triangularity. This can provide an explanation for the regime recently identified on JET that has been called mixed type-I/type-II ELM regime [Saibene G *et al* 2002 *Plasma Phys. Control. Fusion* **44** 1769]. A modified version of the peeling-ballooning cycle for type-I ELMs on JET, that takes into account the WB mode phenomenon and is consistent with the experimental observations, is proposed.

6.1 Introduction

The energy losses associated with type-I ELMs [1–3] are a serious concern for ITER due to the possibly unacceptable transient heat loads expected on the divertor tiles [4, 5]. The understanding of type-I ELMs, in particular their origin and the underlying processes governing their dynamics, is still incomplete. From the MHD point of view, research is increasingly focussing on the role of the most promising ideal instabilities, namely (finite-n) ballooning and kink-(peeling) modes, and more recently also on coupled ballooning-kink modes, leading to the proposition of a so called peeling-ballooning cycle for type-I ELMs [6].
Washboard (WB) modes are a very robust phenomenon commonly observed in JET H-mode discharges, and are not thought to belong to one of the above mentioned instabilities. Since their discovery [7], rather little attention has been paid to them, either theoretically or experimentally. So far they have not been regarded as an ELM-relevant instability. However, in this paper evidence for their involvement in the pedestal and ELM dynamics will be presented.
The paper is organised as follows. In section 6.2 an overview of WB properties is given, recalling earlier findings from [7] where appropriate. Section 6.3 is devoted to the observation of an exclusive interaction between the WB modes and a class of type-I ELM precursor modes, commonly observed at JET in discharges with low to moderate collisionality. The relationship between the WB modes and a regime recently identified on JET, that has been called mixed type-I/type-II ELM regime, is discussed in section 6.4. Building on these findings, a modified version of the peeling-ballooning cycle for type-I ELMs, that takes into account the physics of WB modes, will be proposed in section 6.5. Finally, a summary and a discussion of the results are given.

6.2 WB properties

Figure 6.1 shows a spectrum of toroidal mode numbers for an example ELMy H-mode, where the colours denote the toroidal mode numbers n. The n-numbers

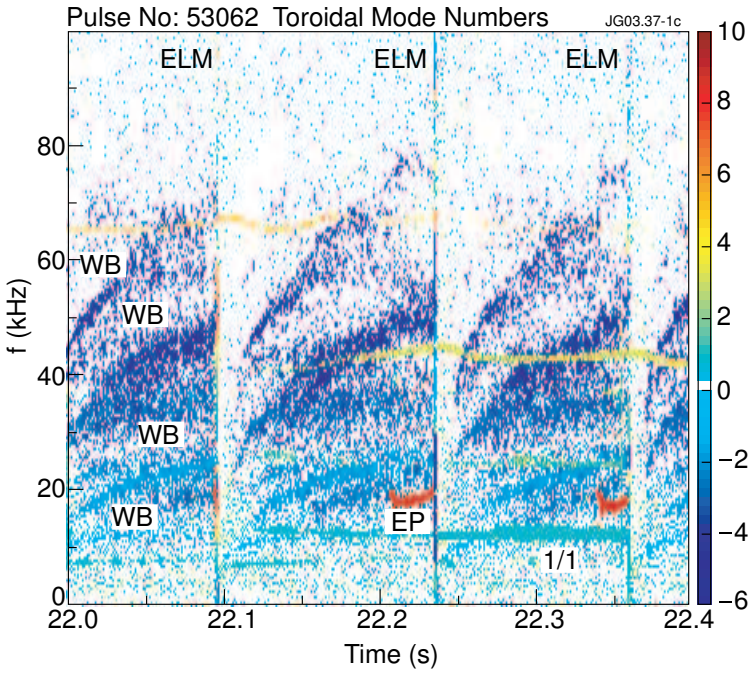

Figure 6.1: Spectrum of toroidal mode numbers n. Three type-I ELMs occur at 22.096 s, 22.24 s and 22.36 s. The red coloured modes ($n = +8$) are type-I ELM precursors [8]. The WB modes are the multiple blue coloured broader bands propagating in the direction of the electron-diamagnetic drift (negative n-numbers).

are obtained by making a time-windowed Fourier decomposition of the signals of a toroidal set of Mirnov coils and analysing the relative phase shift of the fluctuations. Depending on the data acquisition the signals have either 250 kHz or 1 MHz sampling rate. For the analysis a high resolution array of 5 coils, with toroidal angles $\Delta\phi$ gradually increasing from 1.7 to 15.9 degrees, has been used, adequate for mode numbers $n \leq 11$. A subset of the coils with lower $\Delta\phi$ was employed if higher mode numbers needed to be resolved or simply to check the correctness of previous calculations. To reduce the noise level of the plots, points are discarded when the amplitudes are below a user defined threshold or the fitting error of the mode number exceeds a certain amount. Toroidal mode number spectra are convenient for discriminating the various types of MHD activity present. Due to its twofold filtering (in frequency- and in phase-space), they are very useful for finding activity that is often only faintly visible on the magnetic spectrograms (like the WB modes), and will be often used throughout this paper. Positive and negative mode numbers are detected. Modes with negative n rotate in the opposite direction (toroidally or poloidally) to modes with positive n. The convention used here is that modes with negative n rotate in the

direction of the electron diamagnetic drift. Three type-I ELMs occur at 22.096 s, 22.24 s and 22.36 s. In between them one can observe several (blue coloured) bands of activity with frequencies ranging from $\sim$ 10-80 kHz propagating in the direction of the electron diamagnetic drift. These are the WB modes. They have typically mode numbers in the range $n = -1$ to -8.
In between ELMs, WB modes have a quite characteristic frequency evolution. Normally both the WB frequency and the spectral extent are initially low when reappearing after an ELM, and tend to increase gradually until interrupted by the next ELM. In longer ELM-free phases, in particular, the WB frequency reaches a steady value. In time-frequency plots the WB bands then sometimes resemble the periodic ridges of an old-fashioned washboard (from which their name originates). Generally, the WB frequency evolution is affected by the level of gas fuelling (as will be discussed later). In the example of figure 6.1 no fuelling is applied.
In figure 6.1, the red coloured modes ($n = +8$) around 20 kHz are so called type-I ELM precursor modes [8]. Both the ELM precursor modes and WB modes are observed at pedestal radii. In contrast to the WB modes, the ELM precursors are observed to propagate in the direction of the ion diamagnetic drift. This indicates that WB modes belong to a different class of instabilities than the ELM precursor modes. In general, the range of ELM precursor n numbers which have been observed is 1-13. Precursors with low $n \sim$ 1-3 are known to be external kinks (also known on JET as Outer Modes [9, 10]), while experimental findings and their comparison with stability calculations suggest that the precursor modes with higher n are not pure external kinks but coupled kink-ballooning modes. The precursor modes are regularly detected in discharges with low to moderate (normalised) electron pedestal collisionality (up to $\nu_e^* \sim 2$, roughly). At higher collisionality the modes seem to be absent, indicating that a sufficiently high edge current is important to destabilise the precursors. Longlived precursors are often seen to grow and shrink repeatedly during their lifetime, and can change their dominant n-numbers rapidly. Detailed studies of the type-I ELM precursors have been presented elsewhere [8]. We shall return to them later.
The analysis of the poloidal mode numbers m on the basis of poloidally distributed coils is more complicated. Due to the plasma toroidicity the apparent m number depends on the poloidal angle where the coils are located (so called θ^*-effect [11, 12]). Plasma shaping (elongation, triangularity) and the presence of an X-point impose further difficulties for modes located close to the plasma boundary. The X-point, in particular, can distort the poloidal mode structure considerably. Poloidal mode numbers determined by coils picking up magnetic fluctuations around the plasma midplane ($\theta = 0, \pi$) will then have the tendency to be lower than the real m-number of the mode. Only a limited numbers of coils, distributed poloidally around the plasma cross section, are available on JET. For the analysis 4 coils are used, two on the low field side (6 degrees apart), and two

Pulse no.	n-number	m-number	q_{95}
42840	-1	-4.0 to -4.5	3.8
50846	-1	-3.0 to -3.5	3.3
52308	-1	-3.2 to -3.7	3.2
53062	-1	-4.0 to -5.0	3.6
53299	-1	-3.2 to -3.7	3.2

Table 6.1: Poloidal mode numbers m for WB bands with $n = -1$, obtained through the analysis of the phase shifts of the fluctuations measured by four poloidally distributed Mirnov coils. Also given for each discharge is the safety factor at 95% of the poloidal flux, q_{95}, calculated by EFIT.

on the high field side (50 degrees apart). Due to aliasing effects the set of coils is not suitable for the analysis of modes with high m numbers, but for lower m ($\lesssim 6$) it has proved reasonably reliable for modes such as NTMs [13]. The procedure used for the analysis is described in more detail in Appendix B of [7]. For the WB bands with the lowest n ($n = -1$) the poloidal mode number analysis gives reproducible results, as summarised in table 6.1. For each discharge 2-3 fast acquisition time windows have been analysed. Within each discharge the resulting m-numbers were not found to change significantly. The m-numbers obtained are comparable to, or slightly larger than, q_{95}, and thus correspond to rational surfaces located close to the plasma boundary.
Figure 6.2 shows previous results of a coherence analysis for a hot-ion H-mode discharge [14] with particularly distinct WB modes (see also figure 6.8). The coherence analysis uses a reference Mirnov signal and channels of the JET edge reflectometer [15,16] with cut-off densities ranging from 0.43 to 4.13×10^{19} m^{-3}. The upper plots give the values of the coherence and phase of the cross-spectral density, respectively, as a function of major radius R and frequency f. The dashed lines denote the measuring radii of the reflectometer channels estimated on the basis of a density profile obtained with the core LIDAR [17]. In general, the resolution of the core LIDAR is about 12 cm and not sufficient to resolve properly the pedestal but tends to overestimate its width. Therefore, the cut-off radii of the reflectometer channels are probably even closer to the separatrix, which EFIT predicts to be at $R = 3.86$ m (with an uncertainty of ~ 1 cm) for this case. It is difficult to give on this basis an accurate estimate of the radial extent of WB modes with respect to the width of the transport barrier, but it is certain that the WB modes are located at the plasma edge, occuring at least at pedestal radii but possibly extending further inwards into the plasma [7]. One can further see from figure 6.2 that WB modes show kink-like radial displacements with no radial phase inversions ("twisting parity"), hence they are not magnetic islands.

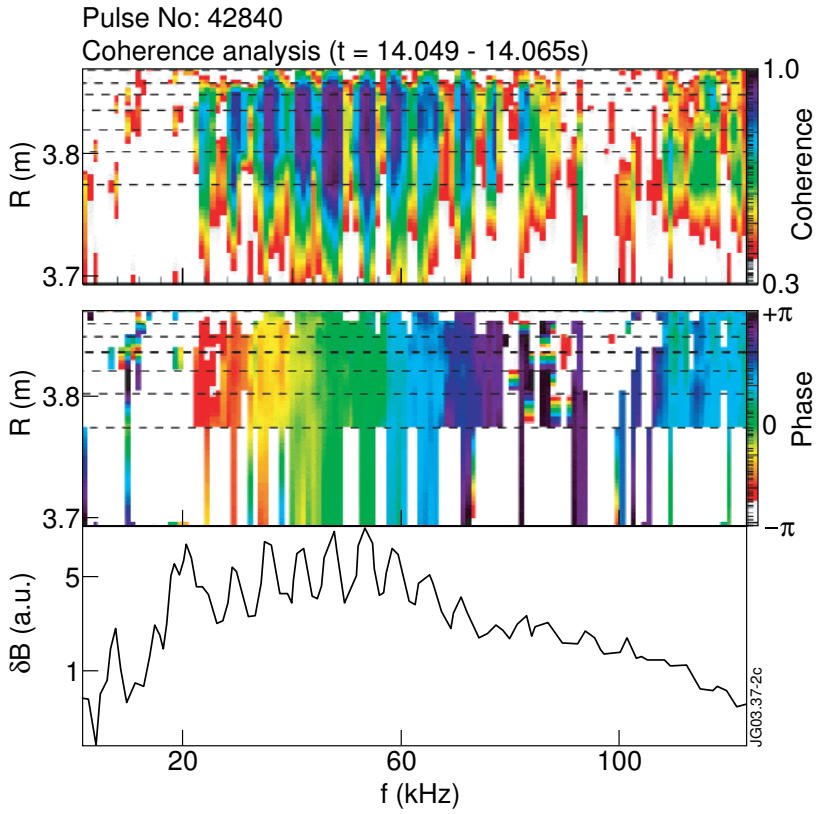

Figure 6.2: Coherence and phase spectra as a function of frequency and major radius R for a set of multiple WB bands (taken from [7]). The separatrix as calculated by EFIT is at $R = 3.86$ m. The colour scales are shown at the right of each plot. The dashed lines denote the measuring radii of the reflectometer channels. The WB bands occur at $\sim$ 20-75 kHz. The third plot shows the power spectrum of the reference Mirnov signal, where the individual WB bands are clearly visible.

The amplitude of WB modes is not constant but appears to be continuously fluctuating. This can be generally observed in spectrograms or n-number spectra like figure 6.1, where the individual WB bands are seen to be composed of intermittent pulsations rather than a continuous mode. The time scale of this fluctuations could not be accurately determined, but it seems to be comparable to the time resolution of the Fourier analysis. The amplitude fluctuations are also likely to be the cause for the relative broadness of the individual WB bands in terms of frequency. From the spectral width of the WB bands the WB amplitude is estimated to fluctuate with a typical repetition rate of 1-3 kHz. The possibility that the frequency spread of each WB band originates from a set of WB modes with same n but located at slightly different edge radii is not supported. Changes in the WB mode phase across the reflectometer channels

should then be observed in figure 6.2, which is not the case.
The displacements associated with the WB modes are small. For individual WB bands density displacements in the sub-mm range have been previously obtained from the analysis of edge reflectometer data [7]. ECE measurements are of limited use for the study of WB modes, because the noise of the ECE channels turns out to be at least of the same order as the WB induced fluctuations, and because only measurements from the inner part of the pedestal are available (further outwards towards the separatrix the plasma loses its optical thickness). Assuming that the real noise of the ECE channels is given by the thermal noise, which is determined by the pre- and postdetection bandwidth, for the optically thick radii an upper bound for the WB induced displacements of roughly 1 mm is obtained, which is compatible with the reflectometry results. The small magnitude of the displacements is in contrast to the observed relative broad radial extent of the WB modes, which according to the data seems to be at least of the order of several cm.
Since WB modes rotate opposite to the core toroidal plasma rotation, the often observed gradual increase of the WB frequency between ELMs cannot be explained in terms of toroidal plasma acceleration. This would require a reversal of the toroidal rotation velocity v_ϕ at the transport barrier, with the reversed v_ϕ having to reach values in excess of 200 km/s to reproduce the measured WB frequencies. This implies an edge rotation which is comparable to the core rotation, but in the opposite direction, for which there is no evidence.
Experimentally, it has been repeatedly observed that a close relationship exists between the evolution of the WB frequency and the evolution of the edge electron temperature measured by ECE channels resonant close to the pedestal top (T_e^{ped}). For the discharges analysed here an array of 48 ECE heterodyne radiometer channels was available, viewing the plasma horizontally from the low field side, slightly below the plasma midplane. The channels have a spatial resolution of typically $\sim$ 1-2 cm. ECE data with a frequency response of 1 kHz is available throughout the discharge, while for selected time windows fast ECE data with 250 kHz sampling rate is available as well. Figure 6.3 gives a comparative plot for the frequency evolution of WB bands and the evolution of T_e^{ped}, showing a good qualitative agreement in the evolution of both quantities. This suggests that the observed WB frequency behaviour originates from the increasing diamagnetic drift associated with the gradual pedestal recovery between ELMs. A further example is shown in figure 6.10, which shows that, unlike the edge temperature, the edge density does not affect the WB frequency noticeably. The following relation holds for the electron diamagnetic frequency:

$$f_{*e}(r,t) \sim \frac{p_e'}{n_e} = \frac{n_e'}{n_e} T_e + T_e' \tag{6.1}$$

Due to diagnostic limitations, neither the gradients of the edge density and edge temperature, nor their evolution in time are determined to a sufficient accuracy

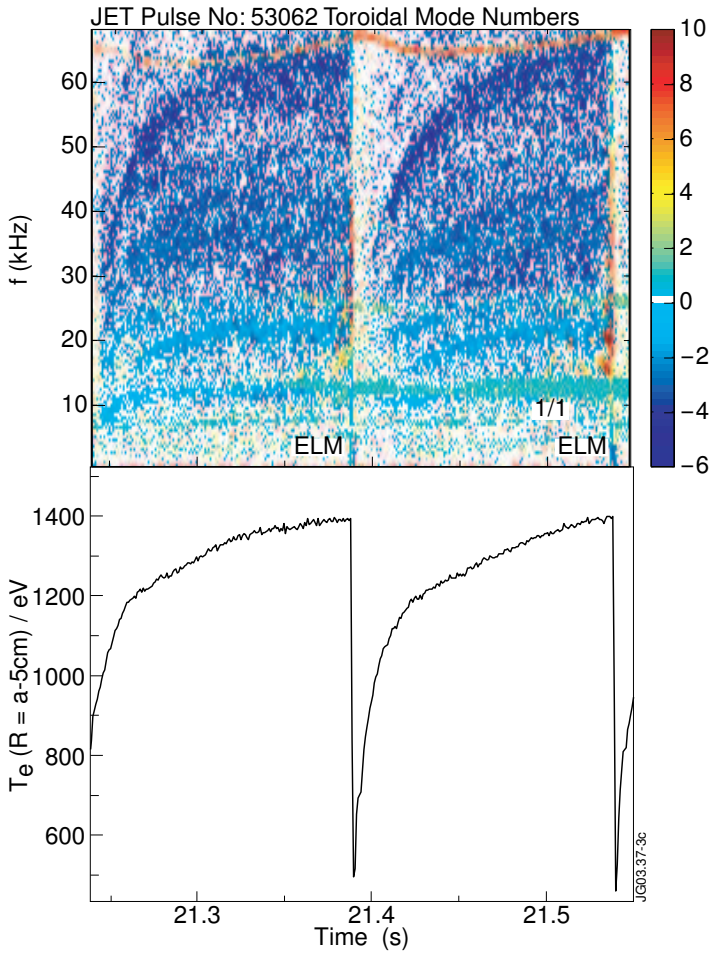

Figure 6.3: (a) Spectrum of toroidal mode numbers showing the WB frequency evolution and (b) electron temperature at the pedestal shoulder measured by means of ECE showing a close relationship between both quantities. In (a) the green coloured mode (labelled 1/1) around 13 kHz is a sawtooth precursor.

to allow for a quantitative comparison of the edge diamagnetic drift with the WB mode frequency evolution. Since the density-related contribution appears simultaneously on the numerator and the denominator of the first term of equation (6.1), and since for given radii both n_e and n_e' increase during the pedestal recovery, the density dependence of the diamagnetic drift is likely to be weak compared to the temperature dependence. However, improved edge measurements are required to confirm this.

It cannot be excluded that a spin-up of the poloidal plasma rotation (v_θ) at the edge could also contribute to the observed WB frequency behaviour, but the measurement of v_θ is difficult. Neoclassical theory predicts the poloidal rotation of the main ion species to be coupled to the ion temperature gradient [18, 19],

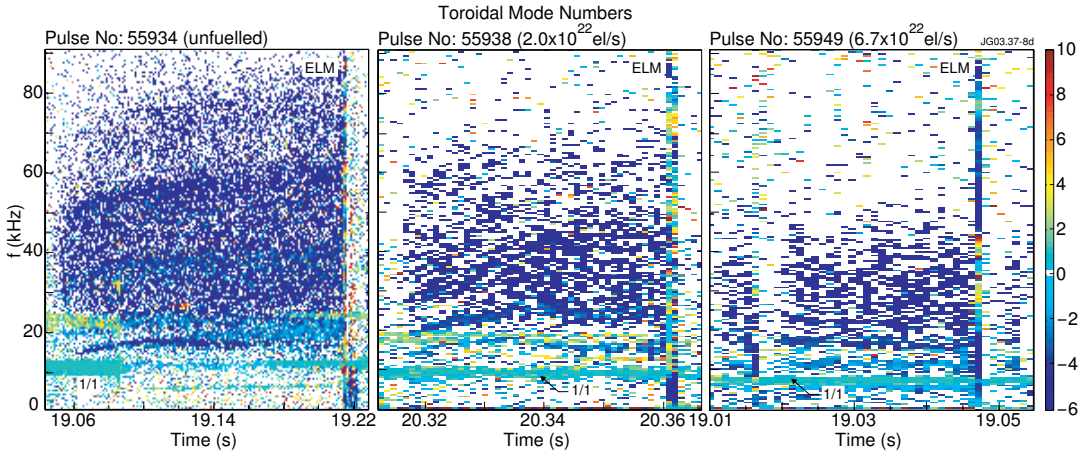

Figure 6.4: WB modes in a gas puff scan (at low triangularity). Each plot depicts a single ELM period. With increasing gas fuelling (from left to right) the spectral distribution of WB modes becomes narrower and evolves towards lower frequencies. This frequency behaviour is consistent with the gradually lowered edge temperature due to the gas puffing. At high gas rates the WB bands usually tend to occur only around 10-40 kHz. The green-coloured modes around 10 kHz are sawtooth precursors.

and therefore v_θ could evolve in time in a similar manner as the ion diamagnetic drift. The sign of v_θ depends on the ion collisionality. For the range of collisionalities relevant here ($0.05 \lesssim \nu_i^* \lesssim 5$), the poloidal rotation is predicted to be in the direction of the electron diamagnetic drift.

The frequency of the WB modes is influenced by the level of gas fuelling. Figure 6.4 shows a set of discharges with different gas fuelling levels. With increasing gas puff the spectral distribution of WB modes becomes narrower and evolves towards lower frequencies. This behaviour is consistent with the gradually lowered edge temperature. When fuelling levels are low, the individual WB bands are usually well separated in frequency and thus clearly discernable in spectrograms (see also figures 6.1 and 6.3). With increasing fuelling the WB band frequencies tend to become closer to each other, and, at sufficiently high fuelling rates, they can merge into a broader band of WB activity where the individual WB bands composing it are difficult to discern anymore. At high gas rates the WB activity typically occurs only around 10-40 kHz. The time evolution of the edge electron temperature between ELMs does also change with fuelling. The temperature drop per ELM decreases with increasing edge density, and it is sometimes observed that T_e saturates already at an early stage of the ELM period. In that case the WB frequency does not change much, or even remains constant, between the ELMs.

WB modes have never been observed in L-mode, but it is difficult to exclude

their existence definitely. Due to the absence of a strong edge gradient and its associated diamagnetic drift, very low WB rotation frequecies can be expected, and this would impose inherent difficulties on the detection of the WB modes. So far WB modes have only been observed in situations where a sufficiently developed H-mode pedestal is present. In particular, in ELM-free or type-I ELMy H-mode the WB modes are basically always encountered. In situations where the pedestal is present but less pronounced, like in the phase shortly after a type-I ELM, or typically also in type-III ELM regime, WB modes are often not detected. This suggests that the presence of an H-mode barrier is a necessary (but not a sufficient) condition to destabilize the WB modes.
Figure 6.5 shows a magnetic spectrogram for a standard type-I ELMy-H discharge, fuelled with $2.3 \cdot 10^{22}$ el/s, showing a time window comprising six type-I ELMs. The colourmap of the spectrogram is chosen to change colour only in a narrow range of amplitudes around that of the WB modes. The spectrogram has further been corrected for the frequency dependence of the magnetically measured mode amplitudes. The numbers to the right of the colourscale of the spectrogram denote the $\log_{10}$ of amplitude. Also shown are the traces of the electron temperature near the pedestal top, measured through ECE, and the line-averaged edge density, measured by a Far Infra-Red (FIR) interferometer [20]. Due to the geometric layout of the interferometer cord used (it views the plasma vertically on the low field side, cutting the midplane approximately 10 cm inside the separatrix), the line averaged density measured by this cord is effectively a good surrogate measurement for the density near the pedestal top. The bottom plot in the figure shows the inner and outer divertor D_α signals. The time between two consecutive ELMs Δt_{ELM} varies greatly from ELM to ELM. The spectrogram also shows that different levels of WB activity are observed in each inter-ELM period. This is further exemplified in figure 6.6a, where the time averaged power spectrum of the inter-ELM activity prior to the fourth ($\Delta t_{\mathrm{ELM}} = 62$ ms) and the sixth ($\Delta t_{\mathrm{ELM}} = 24$ ms) ELM are compared. Prior to the fourth ELM higher WB activity is observed. For each ELM-interval the level of WB activity can be quantified by averaging the individual power spectra over time, and integrating the resulting averaged power spectrum over the frequency range of the WB modes. In Figure 6.6b the result of such an analysis is shown, plotted against Δt_{ELM}. The analysis has been performed over the whole stationary phase of the discharge, and each circle in the plot corresponds to one inter-ELM period. The WB amplitude and the time Δt_{ELM} are clearly correlated. The causality of events is however unclear: It is not clear whether the WB modes reach higher amplitudes in the longer inter-ELM intervals simply because the ELM interrupts their growth at a later time, or whether strong WB mode activity is responsible for an extension of the ELM period. The diamonds shown in figure 6.6b denote the energy loss per ELM (ΔW_{ELM}), recorded during the fast acquisition time window of the diamagnetic loop. The energy loss per

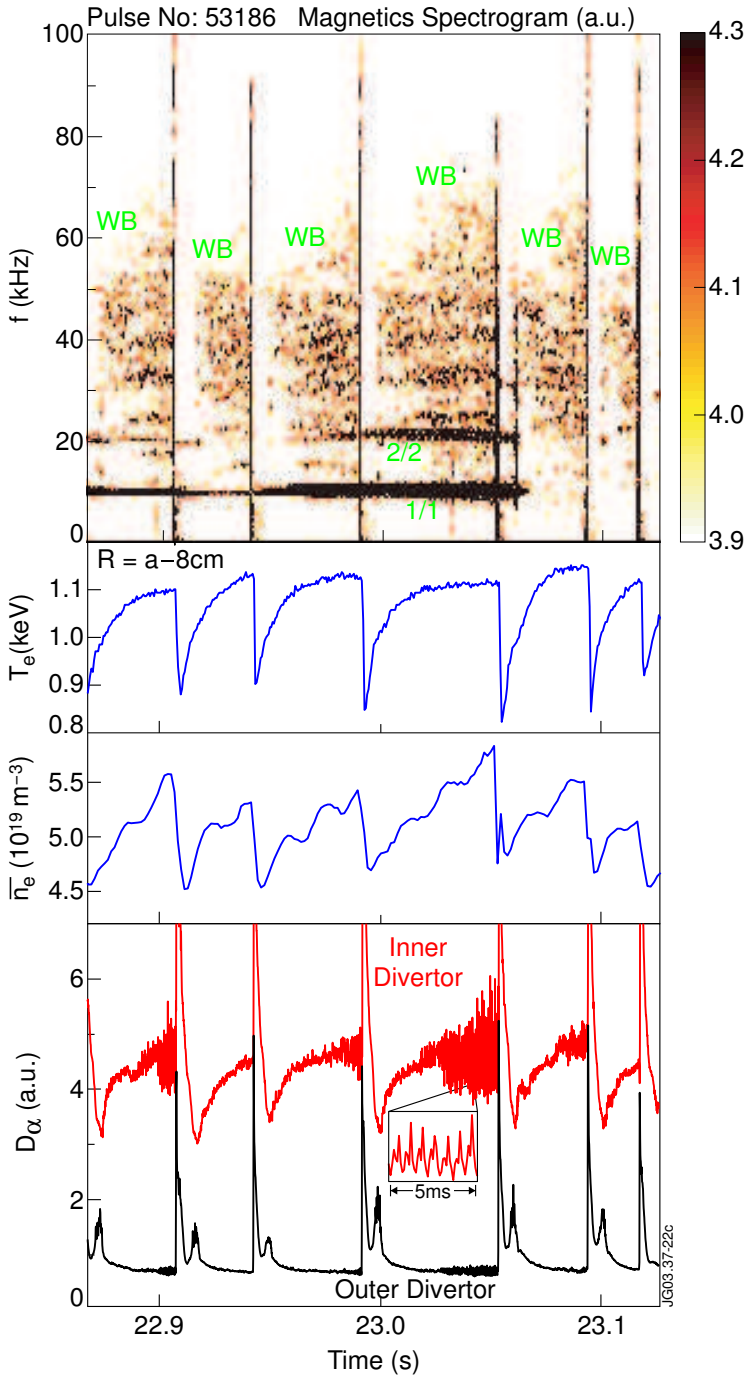

Figure 6.5: Magnetics spectrogram for a time interval with different levels of WB activity between ELMs, together with the trace of an ECE channel resonant near pedestal top, and the line-averaged edge density (measured by an FIR interferometer). The bottom plot shows the corresponding divertor D_α signals for the inner and the outer divertor. The numbers given in the colourbar of the spectrogram are a.u.

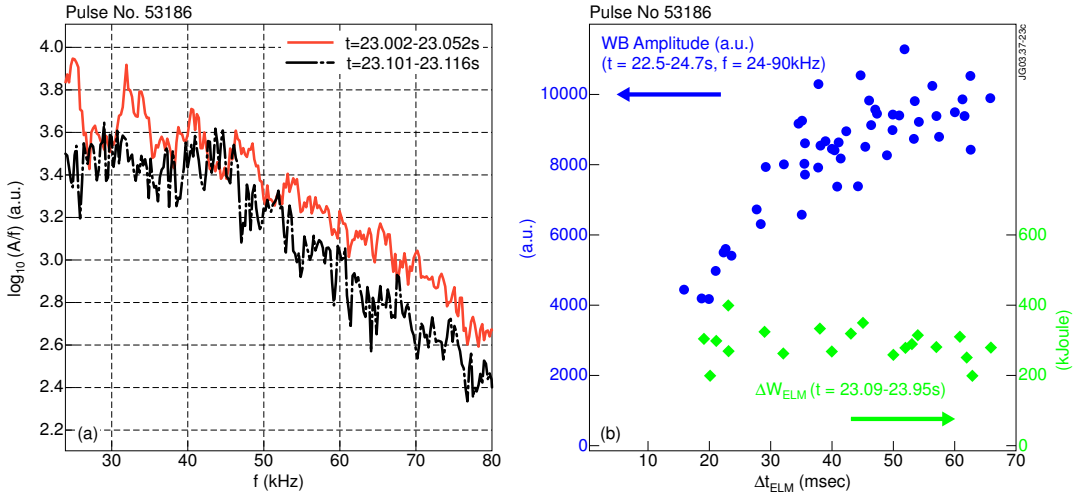

Figure 6.6: (a) Comparative plot of the time-averaged power spectra (at WB frequencies) for the ELM-intervals prior to the fourth ELM (solid curve) and the sixth ELM (dash-dotted curve) of figure 6.5, showing a larger overall level of WB mode activity in the former case. (b) Time-averaged, frequency-integrated WB amplitude (circles) versus the time Δt_{ELM} between two consecutive ELMs, for the same discharge. The analysis has been performed during the stationary phase of the discharge (from 22.5 to 24.7 s). Each circle corresponds to an ELM period. The WB amplitude has been integrated from 24 to 90 kHz, thus avoiding the core MHD activity (mainly 1/1 and 2/2 modes), which happens at lower frequencies. Increasing WB amplitude correlates with increasing Δt_{ELM}. Also shown is the energy loss per ELM ΔW_{ELM} (diamonds), determined during the fast acquisition window of the diamagnetic loop (from 23.09 - 23.95 s). ΔW_{ELM} does not increase with Δt_{ELM}.

ELM is not seen to vary with Δt_{ELM}, which implies that the variation in Δt_{ELM} must have a different cause. Also the input power P_{heat} and the radiated power P_{rad} keep constant over the time interval analysed (15.5 and 7 MW, respectively). Divertor diagnostics have been examined to gain further insight. In the bottom part of figure 6.5 the inner and outer divertor D_α signals are shown. A fast spiky activity is observed between the ELMs, which is more pronounced on the inner than on the outer divertor signal. The same activity is observed on the signals of the divertor probes located near the strike points (not shown here). The activity is composed of small bursts with a repetition rate of a few kHz. As has been noted above, the WB amplitude has been estimated to fluctuate on a similar time scale. However, it has not been possible to establish from the data whether the observed activity does indeed originate from the WB modes. While there are many discharges where the magnitude of the fast inter-ELM D_α-activity is observed to correlate well with the WB mode amplitude, other

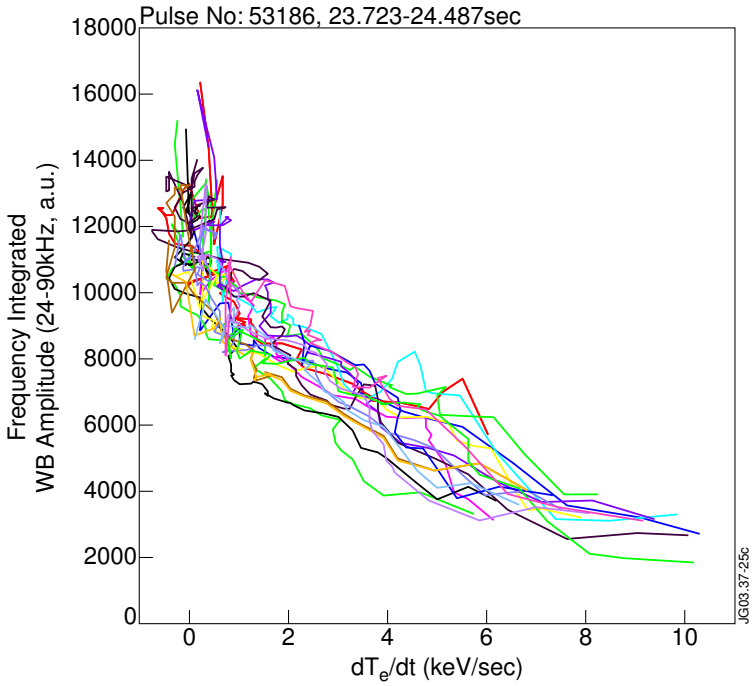

Figure 6.7: Time traces for 19 consecutive inter-ELM periods during the stationary phase of discharge 53186 (cf. figure 6.5), showing the evolution of the time derivative of the edge electron temperature measured near the pedestal top (determined via ECE) relative to the level of WB activity (integrated over frequency from 24-90 kHz). Each curve illustrates the time evolution of the two quantities during one inter-ELM period. The ELM period starts in the lower right part of the plot (low WB amplitude, high dT_e/dt), and evolves towards the upper left corner (high WB amplitude, low dT_e/dt). The curves follow a narrow band in configuration space, independently of the ELM period, indicating a correlation between the WB amplitude and the rate of pedestal electron temperature increase.

discharges have been found were this correlation is less convincing. The analysis is further hampered by the strong dependence of the diagnostics' response on the divertor conditions.

Figure 6.7 shows the time traces for 19 consecutive inter-ELM periods during the stationary phase of discharge 53186, showing the evolution of the time derivative of the edge electron temperature measured near the pedestal top (determined via ECE) relative to the level of WB activity (integrated over frequency from 24-90 kHz). Each curve illustrates the time evolution of the two quantities during one inter-ELM period. The ELM period starts in the lower right part of the plot (low WB amplitude, high dT_e/dt), and evolves towards the upper left corner (high WB amplitude, low dT_e/dt). The curves follow a narrow band in config-

uration space, independently of the ELM period, indicating the existence of a correlation between the WB amplitude and the rate of pedestal electron temperature increase. The analogous analysis for the time-derivative of the edge density (relative to the WB mode amplitude) is hampered by an oscillation with approximately 50 Hz present on the interferometer signal. The oscillation is regularly encountered on this signal, although with varying degree of accentuation, and is not believed to be real. Its origin is not fully understood yet. The oscillation is clearly recognisable in the density trace shown in figure 6.5. Without this oscillation, it can be discerned from figure 6.5 that, unlike for the edge temperature, the rate of increase of edge density does not change greatly throughout an ELM period (this is most clearly seen in the ELM period prior to the fourth ELM). This implies that the edge density cannot (or at least not largely) be affected by the WB mode amplitude. Thus, in contrast to the edge electron temperature, no correlation is found between the WB mode amplitude and the time derivative of the edge density.

The strongest evidence obtained so far for the active involvement of WB modes in the plasma edge dynamics comes from discharges in which sharp distinct transitions in WB mode amplitude are encountered. Figure 6.8 shows the time evolution of the WB mode activity during the ELM-free high-performance phase of a hot-ion H-mode discharge. A magnetic spectrogram (a) and the corresponding spectrum of n-numbers (b) is shown, together with the time traces of the core (c) and edge (d) electron temperature evolution measured by means of ECE. The bottom plot (e) shows the line-averaged edge density measured by the interferometer. In the example shown three distinct phases can be discerned: During the first phase (up to $t = 14$ s) the WB modes grow slowly, keeping modest overall amplitude. The edge temperature grows steadily during this phase. At $t = 14$ s a sudden increase in the level of WB activity is observed (second phase), and the growth of the edge electron temperature stops sharply. During this phase, T_e at the pedestal maintains a constant value until $t = 14.33$ s. At $t = 14.33$ s, the arrival of an abnormally large sawtooth crash heat pulse at the plasma edge causes a sudden increase in the edge electron temperature, and, for reasons that will be further discussed in the conclusions, the WB mode activity subsequently nearly disappears. From then on the edge electron temperature begins to rise again steadily. Examples like this demonstrate that the WB modes have a regulating effect on the increase of edge temperature. The effect seems not to be restricted to the pedestal top. In discharges with good ECE coverage of the pedestal radii, the effect has been also observed on ECE channels measuring further outwards in the pedestal region of steep gradients. The only plausible explanation is that WB modes are responsible for a continuous loss of energy into the scrape off layer between ELMs. The existence of a link between the WB mode amplitude and the rate of edge pedestal build-up could be established in numerous discharges. Some further examples will be shown in the next section.

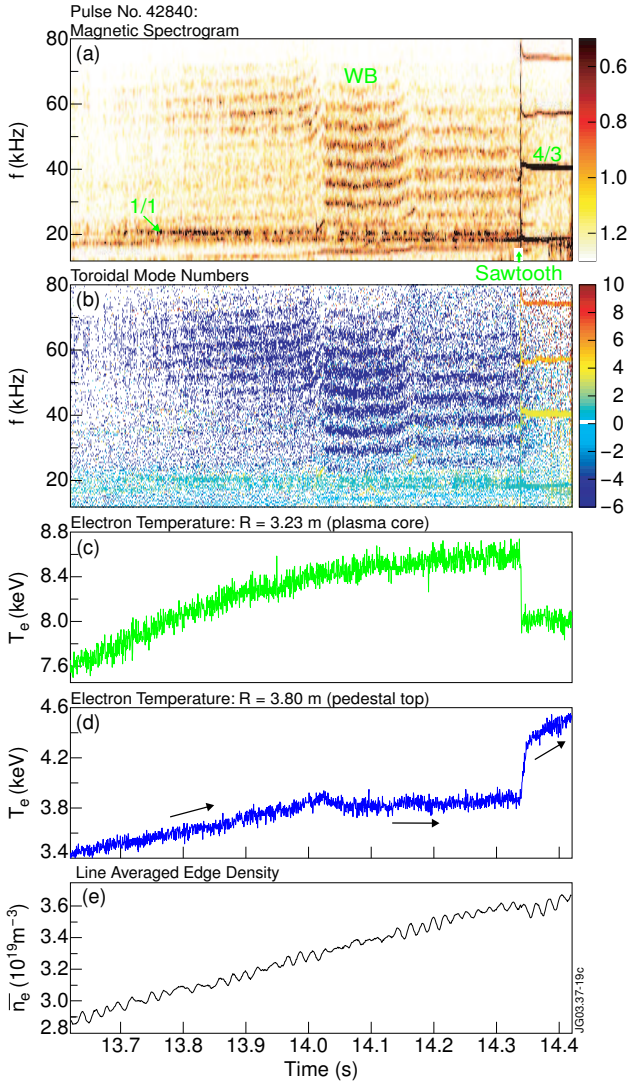

Figure 6.8: Magnetic spectrogram (a) and spectrum of toroidal mode numbers (b) showing the time evolution of the WB mode activity during the ELM-free high-performance phase of a hot-ion H-mode discharge. The other figures give the time evolution of the electron temperature in the plasma core (c), near the pedestal shoulder (d), as well as the line-averaged edge density (e). Three phases can be discerned: During the first phase (up to $t = 14$ s) the WB modes grow slowly, keeping modest amplitude. The edge temperature grows steadily during this phase. At $t = 14$ s a sudden increase in the level of WB activity is observed (second phase), and the growth of the edge electron temperature stops sharply. During this phase, T_e at the pedestal maintains a constant value until $t = 14.33$ s. At $t = 14.33$ s, the arrival of a sawtooth crash heat pulse causes a sudden increase in the edge electron temperature. After the sawtooth crash, the WB mode activity nearly disappears, and the edge electron temperature rises again steadily. The sawtooth crash also triggers core MHD activity (e.g. a 4/3 mode).

6.3 WB modes and type-I ELM precursors

Some of the features of the type-I ELM precursor modes have been outlined in the previous section (the reader is refered to [8] for more details). It has been mentioned that longlived precursors are often seen to grow and shrink repeatedly before an ELM. Such a case is shown in figure 6.9, where, in addition to the WB modes (again in blue), a yellow coloured ($n = +4$) type-I ELM precursor occurs around 15 kHz. The precursor starts long time before the ELM crash, which happens at 21.68 s. Closer examination (zoom view of figure 6.9) reveals that the precursor is continuously appearing and disappearing again. The remarkable feature is, however, that at times where the precursor occurs the WB activity is seen to vanish. This is illustrated in the bottom plot of figure 6.9, where the time-evolution of the frequency-integrated amplitude for both the ELM precursor mode and the WB modes are shown. It is evident that the amplitude of the WB modes is in counter-phase to the amplitude of the ELM precursor mode. An exclusive interaction between the two modes must exist. The physical grounds for this interaction have not been yet identified. In general, the order of events observed is that after an ELM crash first the WB modes reappear, and later on usually one or more type-I ELM precursors set in. Coinciding with the onset of the ELM precursor modes, some of the WB bands (or, as in figure 6.9, all of them) are seen to become weaker. The possibility that a weakening of the WB modes allows the ELM precursors to grow can be excluded by discharges in which the WB modes do weaken but the ELM precursors do not immediately start to grow (see e.g. figure 6.8). Thus, the causality appears to be that the growth of ELM precursor modes weakens the WB modes, and not the reverse.
Sometimes not all the WB bands become inhibited. The frequency of the remaining WB activity is then often observed to increase with the precursor onset. This is best discerned if the WB frequency has reached a steady value prior to the precursor appearance, and an example is shown in figure 6.10. On the spectrum of toroidal mode numbers two diffuse WB bands can be recognised around $\sim$36 and 45-50 kHz (labelled with WB1 and WB2, respectively). Both WB bands keep roughly constant frequency until the onset of ELM precursors at 16.88 s (the dark-red coloured modes at 5-10 kHz, $n = 9$-10). WB2 is inhibited by their occurrence, as shown in the bottom plot of the figure. The amplitude shown in that plot has been obtained by integrating, at each time step of the Fourier analysis, over an 8 kHz wide frequency band whose frequency tracks the frequency of WB2. If, in the bottom plot, one regards the level right after the ELM crash as the WB-free background, then the precursor has led to a drop in amplitude of about 70%. A similar analysis has been carried out for the amplitude of WB1 (not shown here). It is obscured by the 3/3 component of the internal kink, which oscillates in amplitude and coincides with the frequency of WB1, but it is believed that the amplitude of WB1 has not been greatly affected by the ELM

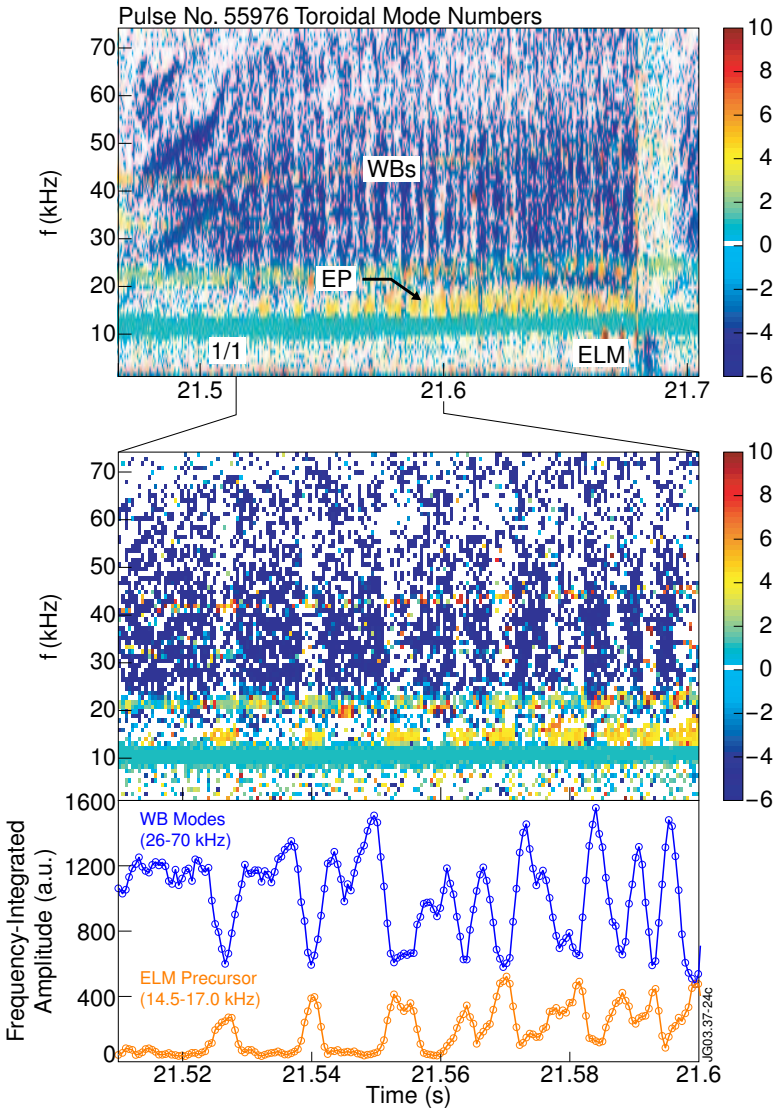

Figure 6.9: Spectrum of toroidal mode numbers for an inter-ELM period, and a zoom view, showing the WB modes (in blue) and a yellow coloured ($n = +4$) type-I ELM precursor mode around 15 kHz. The precursor mode starts long time before the type-I ELM (which happens at 21.68 s). The continuously present green-coloured mode at 10 kHz is a sawtooth precursor. In the bottom plot the corresponding time-evolution of the power spectra (frequency-integrated over the range of frequencies relevant for each mode) for both the ELM precursor mode and the WB modes are shown. The circles on the curves correspond to one time-slice of the Fourier analysis. To smoothen the curves, the values obtained for each time-slice have been averaged with the values for the previous and the next time slice. The amplitude of the WB modes is in counter-phase to the amplitude of the ELM precursor mode.

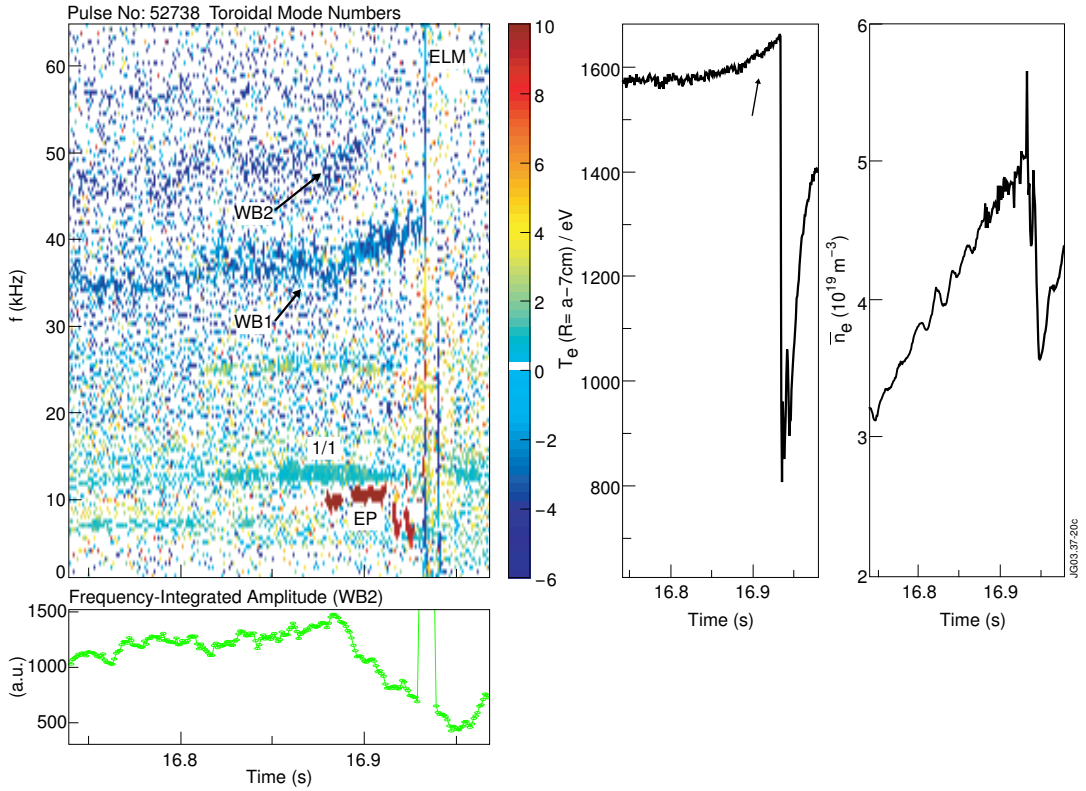

Figure 6.10: (a) Spectrum of toroidal mode numbers highlighting two diffuse WB bands: one around 36 kHz (labeled with WB1), in light blue, and a further even more diffuse WB band at 45-50 kHz, labeled with WB2. Both WB bands keep roughly constant frequency until the onset of ELM precursors at 16.88 s (the dark-red coloured modes (n = 9-10) at 5-10 kHz). WB2 is inhibited by their occurrence, as shown in the bottom plot. The ELM precursors further trigger an increase in the frequency of the remaining WB band WB1 until interrupted by the ELM at 16.93 s. (b) Corresponding traces of electron temperature measured near the pedestal top, and of the line-averaged edge density. The temperature evolution resembles the WB frequency, and begins to increase at precursor onset (this is highlighted by the arrow). In contrast, the density build-up remains seemingly unaffected.

precursors. One can clearly see that the ELM precursors trigger an increase in the frequency of WB1 until interrupted by the ELM at 16.93 s. It is worth recalling from section 6.2 that a relationship exists between the WB frequency and the electron temperature evolution measured near the pedestal top. Together with the mode number spectrum the corresponding traces of the edge electron temperature and the line-averaged edge density are shown, obtained through ECE and interferometry, respectively. The electron temperature evolution resembles the WB frequency, and, in particular, it begins to rise (this is highlighted by the arrow) with the ELM precursor appearance. The temperature increase does not originate from a simultaneous decrease in pedestal density. Instead, the density continues to increase and seems not be be greatly affected. Hence, the onset of type-I ELM precursors has indirectly led, through a WB mode weakening, to an acceleration of the build-up of the electron pedestal pressure; though the mechanism for this remains unclear. Due to diagnostic limitations no comparable data is available to study the temperature evolution of the ion species. It is however expected that collisional energy exchange with the electrons will result in a similar behaviour for the ions.
From figure 6.10 one can discern that the edge electron pressure has been constantly increasing prior to the onset of the ELM precursor, through the increasing edge density. Clearly, the pressure observed prior to the ELM onset would have been also reached in the absence of ELM precursors, though at a slightly later time. Therefore, it is expected that the ELM would have been triggered in any case, also in the absence of ELM precursors. The real value of this kind of examples lies in valuable information that they provide about the operational point of the pedestal in terms of edge current density and edge pressure gradient, and its actual position relative to the kink- and ballooning-stability boundaries. This will be further addressed in section 6.5.
It has to be underlined that this pattern of events (ELM precursor occurrence and a reduction in the WB mode amplitude, and a further increase in the edge electron temperature) is not restricted to the above example but is a robust phenomenon that has been observed repeatedly in JET discharges. Figure 6.11 shows the magnetics spectrogram and ECE signals corresponding to the spectrum of n-numbers used for the introductory example of figure 6.1. As seen on the spectrogram, the longlived ($\sim$25 ms) precursor around 18 kHz prior to the second ELM inhibits a WB band at 25 kHz (the same happens prior to the third ELM, though the 2/2 mode makes it more difficult to see). Again, the amplitude of the other WB bands seems not to be greatly affected by the ELM precursor. This could be an indication that a WB band has to meet some kind of "resonance condition" in order that the inhibition by the ELM precursor can take effect, but the data analysed so far is not yet conclusive in this respect. The precursor oscillations are detected on the fast ECE channel measuring 2 cms inside the separatrix (in the pedestal region of strong gradients), while on the channel

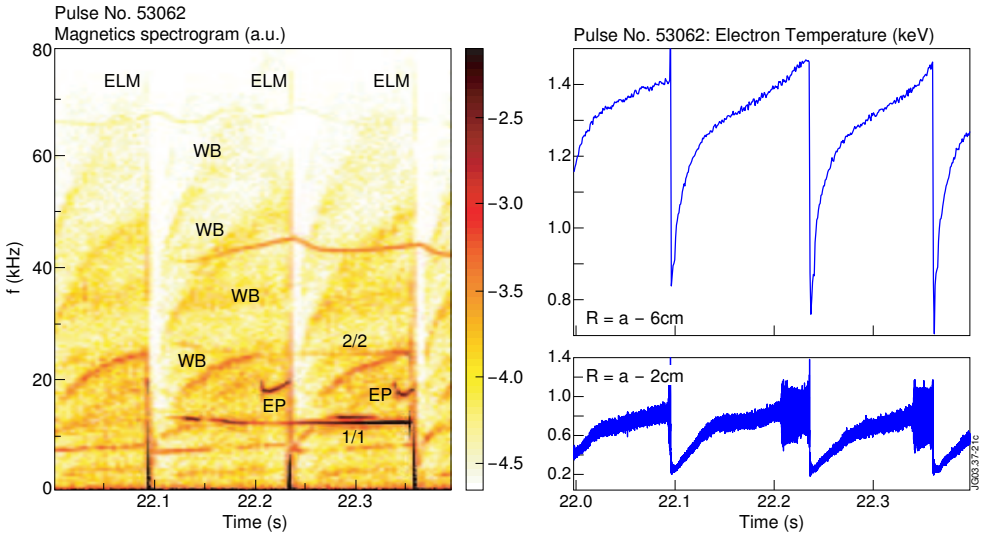

Figure 6.11: Magnetic spectrogram from a coil located on the low field side, corresponding to the introductory example shown in figure 6.1. The longlived ELM precursor (EP) around 18 kHz prior to the second type-I ELM inhibits the WB band at $\sim$ 25 kHz. (The same happens prior to the third type-I ELM, though the 2/2 mode makes it more difficult to see.) Shown on the right are the signals from two ECE channels: one resonant 6 cm inside the separatrix (near the pedestal shoulder, top plot) and one resonant 2 cm inside the separatrix (in the pedestal region of steep gradients, bottom plot). The latter signal is sampled at 250 kHz. The precursor oscillations are detected on the channel resonant 2 cm inside the separatrix. On the channel measuring 6 cm inside the separatrix a slight but still discernable increase in the build-up of the edge electron temperature is observed in the presence of the ELM precursors. Prior to the first ELM a much shorter lived ($\sim$ 1.5 ms) precursor existed. Due to its shortness that precursor could not affect the evolution of the pedestal build-up significantly.

measuring 6 cm inside the separatrix (near the pedestal top) one can observe a slight but still discernable increase in the slope of the edge electron temperature build-up when the precursors are active. Prior to the first ELM a much shorter lived ($\sim$ 1.5 ms) precursor existed. Due to its shortness that precursor could not affect the evolution of the pedestal build-up significantly. The case of shortlived precursors, which is quite often observed, will be further addressed in section 6.5.

A general consequence of the above observations is that, due to their complex interplay with the WB modes, the onset of ELM precursor modes does commonly not lead to an overall pedestal (and thus confinement) degradation, but rather to an improvement of the pedestal. This finding is certainly counter-intuitive and

unexpected. After the onset of ELM precursor modes, the resulting evolution of the pedestal will be a trade-off between the decrease in transport associated with the observed suppression of WB modes, and any increase in transport associated with the ELM precursor modes themselves. The commonly observed accelerated build-up of the pedestal pressure implies a greater particle and energy transport associated with the WB modes. In situations in which the WB modes were absent, the onset of ELM precursor modes has not resulted in an accelerated pedestal build-up, and could even lead to a pedestal degradation.
ELM precursors are not the only possible source of WB mode suppression. WB weakening due to an abnormally large sawtooth heat pulse has been already shown in figure 6.8. Some further cases have been found in which the WB modes become stabilised "spontaneously" in the middle of an inter-ELM period with no identified cause, and, in particular, with no precursors having been detected.

6.4 WB modes and type-II ELMs

The "normal" ELM frequency behaviour observed in low triangularity discharges is that the type-I ELM frequency increases with increasing level of gas puffing. Three effects contribute to this behaviour: First, the pressure at the top of the pedestal p_{ped}, and therefore the energy content of the pedestal, which is given by $3/2 \times p_{\mathrm{ped}} \times V_p$ (where V_p is the total plasma volume) [21], is observed to decrease with increasing density. Therefore, at fixed input power, less time is needed for the pedestal to reach the observed critical pressure. Second, the energy loss per ELM relative to the pedestal energy content is observed to decrease with increasing density. Third, the recovery of pedestal density between ELMs is observed to become faster with fuelling (the simplest explanation is the increased gas fuelling itself, but changes in inter-ELM transport might play a role as well).
Discharges at high triangularity ($\delta \sim 0.5$) show a clear deviation from the standard ELM behaviour, with the ELM frequency decreasing for the higher fuelling rates [22–24], as shown in figure 6.12. In spite of the lowered ELM frequency, the energy loss per ELM does not increase in these cases [22]. Instead, simple power balance considerations demonstrate that the lowered ELM frequency originates from enhanced inter-ELM losses [25]. The anomalous ELM frequency behaviour is accompanied by broadband MHD activity around 30 kHz propagating in the direction of the electron diamagnetic drift, and a grassy signature on the inter-ELM divertor D_α [26]. The similarity of the observations with the type-II ELM regime observed in ASDEX-U [27] suggested the identification of the anomalous ELM regime observed at JET as a mixed type-I/type-II ELM regime [25].
Figure 6.13 shows the parameter evolution of a typical JET discharge with mixed type-I/type-II ELM regime. The presence of a mixed ELM regime during the gas puff phase is recognisable through the lowered type-I ELM frequency compared to after fuelling switch off. Figure 6.14 gives an overview of the MHD activity,

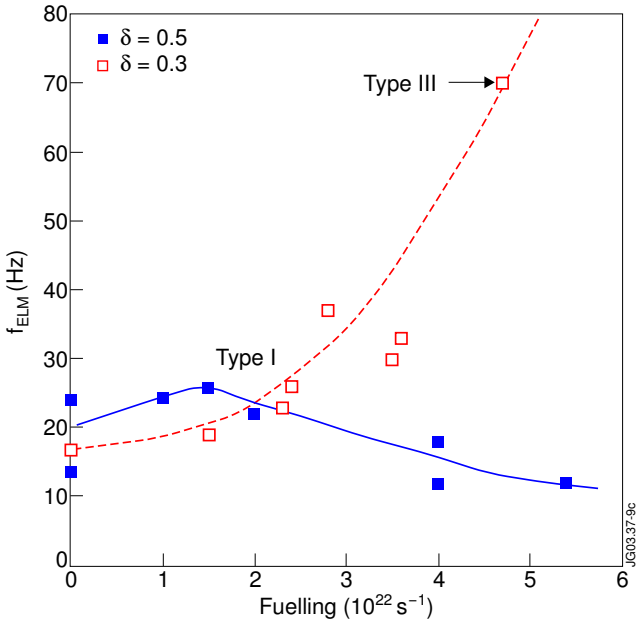

Figure 6.12: Behaviour of ELM frequency with increasing levels of gas fuelling for two scans performed at low ($\delta = 0.3$) and high ($\delta = 0.5$) plasma triangularity, respectively (from [24]). For discharges at high triangularity the ELM frequency decreases for sufficiently high fuelling rates, showing a clear deviation from the standard ELM frequency behaviour. This observation led to the identification of a new regime on JET that has been called mixed type-I/type-II ELM regime.

and in particular of the WB activity, observed at times with and without the gas fuelling. (The gas puff has been switched off at $\sim$ 22.5s.) The WB mode frequencies behave in the expected way, as described in section 6.2: During the gas puff the WB modes tend to keep constant frequency between ELMs and occur only around 10-40 kHz. After switching off the fuelling the WB bands evolve towards higher frequencies, covering a wider spectral range. The enhanced activity seen at 10-40 kHz during the gas puff phase has been associated with the type-I/type-II ELM regime occurrence [26]. It is evident that these are WB modes.
Figure 6.15 shows magnetics spectrograms for two pairs of discharges with different fuelling rates at low and high triangularity, respectively. In order to allow for comparison, the mapping of amplitudes to colours is the same for each pair of discharges. In the case of low triangularity (figure 6.15(a),(b); 2.4 T, 2.4 MA, 15 MW NBI), gas puffing weakens the WB activity, while in high triangularity discharges (figure 6.15(c),(d); 2.7 T, 2.5 MA, 15 MW NBI) the WB activity is clearly enhanced with gas fuelling. The enhancement of WB modes through gas fuelling at high triangularity, and the increase of inter-ELM losses that this is expected to cause, can therefore provide an explanation for the ELM frequency anomaly and the occurrence of the so called mixed type-I/type-II ELM regime

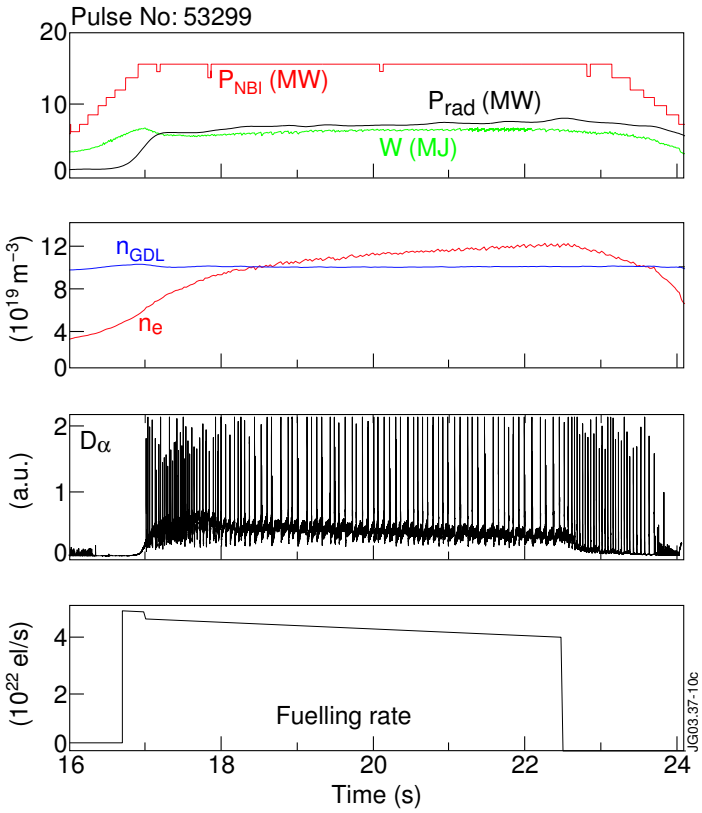

Figure 6.13: Parameter evolution of a typical JET discharge (2.7 T, 2.5 MA, $\delta \sim 0.5$) with mixed type-I/type-II ELM regime. Shown are (a) the NBI power, the plasma energy content W and the radiated power $P_{\rm rad}$, (b) the line averaged density together with the Greenwald density limit, (c) the divertor D_α signal, where the large spikes are due to type-I ELMs, and (d) the gas fuelling rate. The presence of a mixed ELM regime during the gas puff phase is recognisable through the lowered type-I ELM frequency while gas fuelling is on.

at JET.
WB modes provide the enhanced turbulence identified in the references [25, 26] as a characteristic signature of the mixed type-I/type-II ELM regimes on JET, but it has to be emphasized again that WB modes are also present in regimes regarded as pure type-I ELM regimes. It has been shown in the previous sections that WB modes influence the pedestal dynamics also in the latter regime.

6.5 WB modes and the peeling-ballooning cycle

The peeling-ballooning cycle [6] represents a model for type-I ELMs that has gained wide acceptance and constitutes a promising candidate for the under-

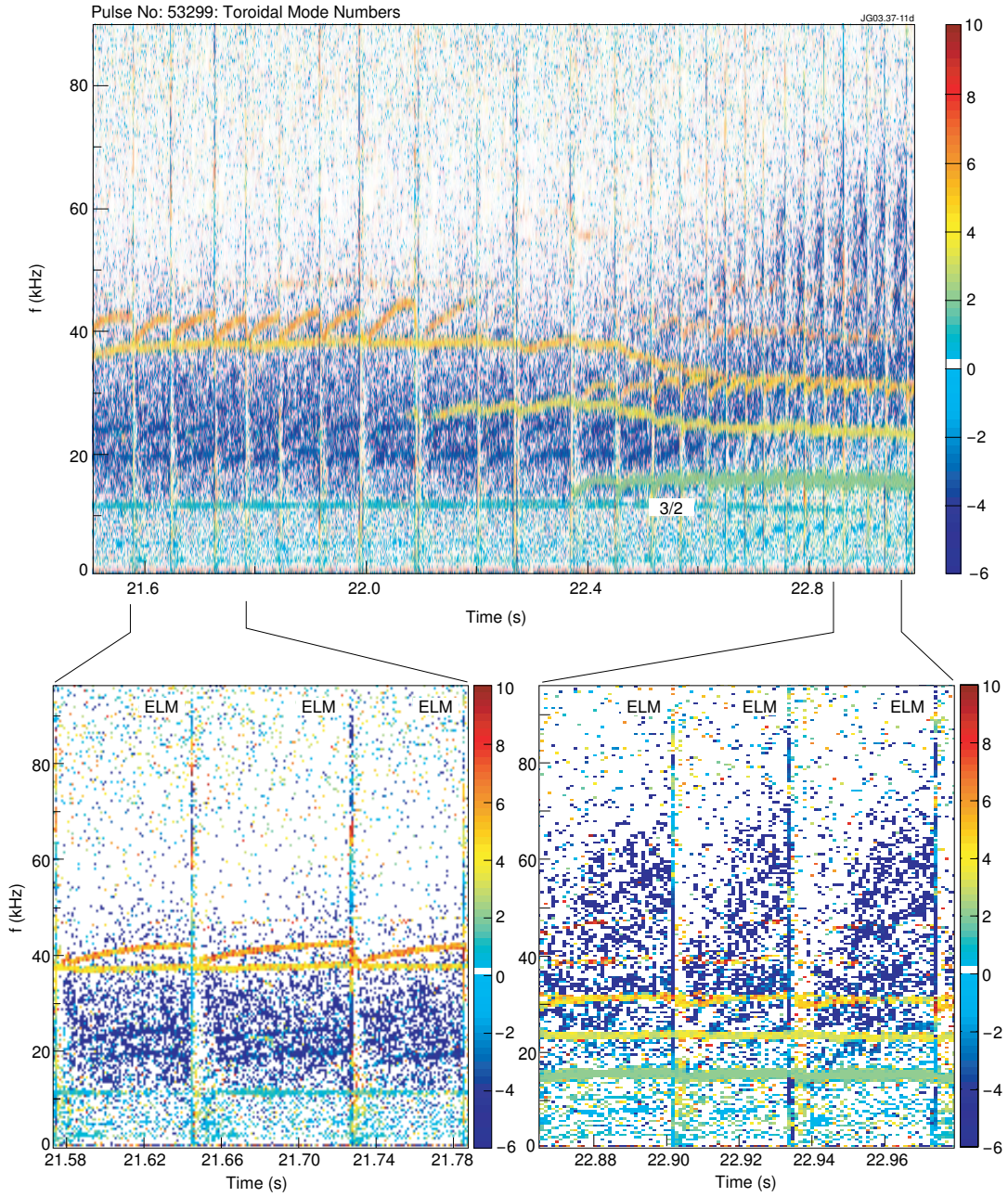

Figure 6.14: Spectrum of toroidal mode numbers for the same discharge as figure 6.13, taking closer looks into the WB activity (in blue) in mixed type-I/type-II ELM regime (during gas puffing) and in type-I ELM regime (gradually recovered after switching off the gas fuelling at $\sim$ 22.5s), respectively.

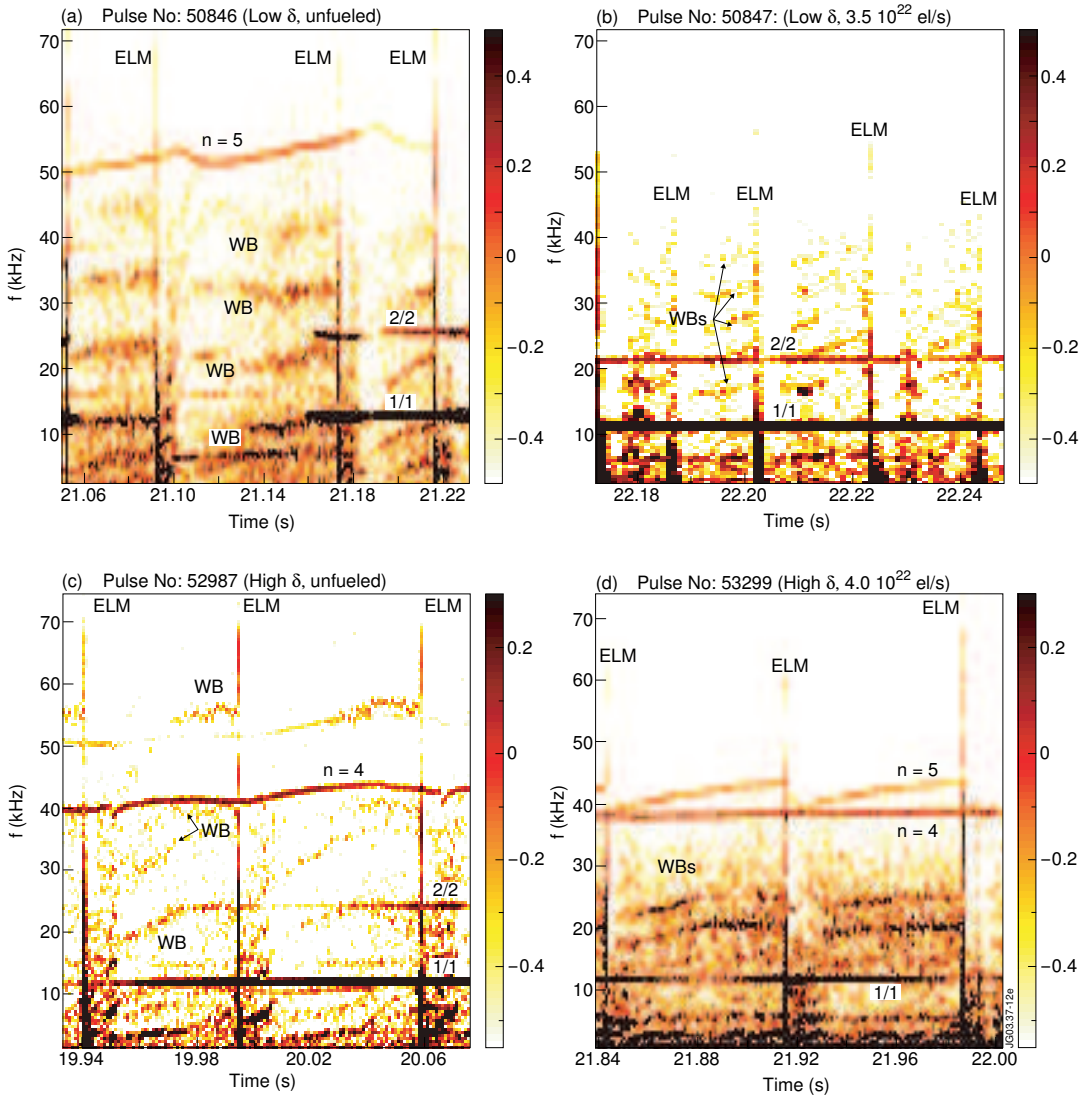

Figure 6.15: Magnetics spectrograms for two pairs of low ($\delta \sim 0.3$) and high triangularity ($\delta \sim 0.5$) discharges with and without strong gas fuelling. At low triangularity WB modes become weaker with fuelling, whereas at high triangularity it is the opposite case. The colourmap for the amplitudes has been kept fixed for each pair to allow for comparison. The numbers to the right of the colourscales denote the logarithm ($\log_{10}$) of amplitude, and are given in a.u.

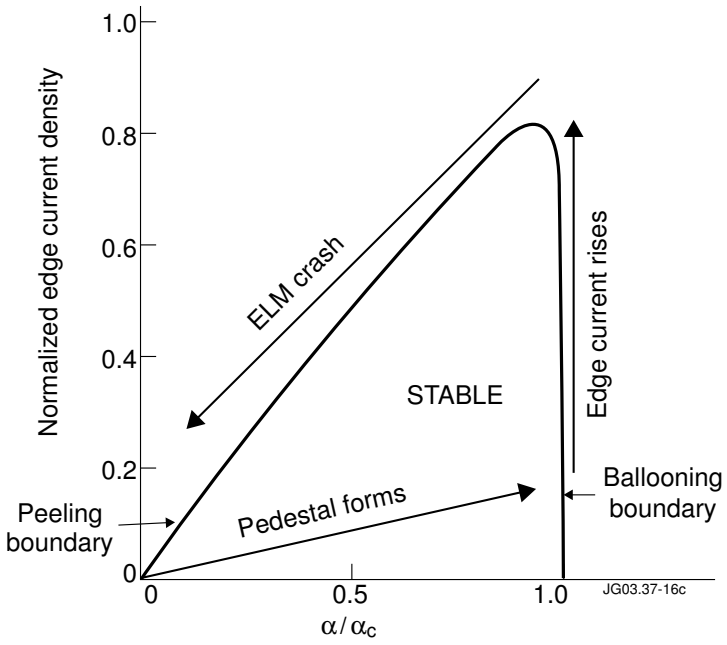

Figure 6.16: Stability diagram for coupled peeling-ballooning modes in the space of normalised edge current and ballooning stability parameter showing the order of events predicted by the conventional peeling-ballooning cycle (from [3]). Just after the previous ELM crash the plasma edge resides in a state of low pressure and low edge current (lower left corner in diagram). Heating builds up the pedestal pressure gradient on a relatively fast time scale until the ideal ballooning limit is reached, where it is limited. With the edge current gradually building up on a slower (resistive) timescale, the pedestal state moves towards the upper right corner of the stability diagram. The ELM is finally triggered when the peeling stability boundary is crossed, where the onset of peeling (or coupled peeling-ballooning) modes causes a further degradation in confinement and therefore a further destabilization of the modes.

standing of ELMs. It is worth briefly reviewing the order of events predicted by this cycle, which is conceptually depicted in figure 6.16: Just after the previous ELM crash the plasma edge resides in a state of low pressure and low edge current (lower left corner in diagram). Heating builds up the pedestal pressure gradient on a relatively fast time scale until the ideal ballooning limit is reached, where, according to the model, it is held. The peeling-ballooning model assumes that the ideal ballooning instability is a benign instability that does not induce a violent event but rather limits the operational space in a smooth way. In a further step, with the edge current gradually building up on a slower (resistive) timescale, the pedestal state moves towards the upper right corner of the stability diagram. The ELM is finally triggered when the peeling stability boundary is

crossed, where the onset of peeling (or coupled peeling-ballooning) modes causes a further degradation in confinement and therefore a further destabilization of the modes.
It is worth mentioning that the model of the peeling-balloning cycle has been recently expanded by *Snyder et al* [28] to include further ELM-types. Within that model, the new ELM-types (type-II ELMs, low density type-III ELMs) are described by cycles with alternative trajectories in the edge current/edge pressure stability diagram.
Comparison with the experimental observations for type-I ELMs made on JET shows some disagreement with the predictions of the peeling-ballooning cycle:
At sufficiently low edge collisionality ($\nu_e^* \lesssim 0.3$) type-I ELMs are regularly preceded by external kinks (low-n ELM precursors). The kink modes start typically 10-100 ms before the ELM [8]. Hence, in that case the kink stability limit is reached well in advance of the ELM event. In addition, the precursor growth rate is generally not seen to increase significantly prior to the ELM. This suggests that the external kinks do not finally trigger the ELM.
Similarly, the kink-limit is probably reached well before the type-I ELM, also when higher n precursors are observed. They commonly precede ELMs in discharges with low to moderate edge electron collisionality (roughly $0.3 \lesssim \nu_e^* \lesssim 2$), but are no longer observed in discharges with strong gas puffing, where according to modelling results the high edge collisionality leads to a significant reduction of the edge current and keeps the pedestal away from the kink-limit [29]. Hence, higher-n precursors do probably become destabilised at the kink limit, or near the top right corner in the stability triangle (which is consistent with peeling-ballooning modes, as proposed in [8]). Higher-n precursors are again observed to start well before the ELM ($\sim$ 1-50 ms). No rapid increase in their growth rate prior to the ELM is observed, which suggests that they do not trigger it.
The peeling-ballooning model does not take into account the physics of WB modes, which have been shown to play an important role in the pedestal dynamics. Therefore, a modified version of the peeling-ballooning cycle that takes them into account and is consistent with the experimental observations presented here is proposed. The individual steps are conceptually depicted in figure 6.17, where the WB unstable region has been shaded. Its precise shape is not known but from the observation that WB modes reappear soon after the previous ELM crash, it must concluded that they can become unstable at relatively low pedestal pressure (far below the ideal ballooning limit), and low edge current density. Starting in step 1 from a state of low pressure gradient and low edge current after the previous ELM crash, the pedestal pressure initially builds up unperturbed. Then, with the onset of WB modes and the associated increase in inter-ELM losses, the pressure build-up is slowed down, allowing the edge current to build up on a comparative timescale until the kink stability limit is reached. In step 2, ELM precursors become destabilised at the kink-limit (the ELM itself is not triggered

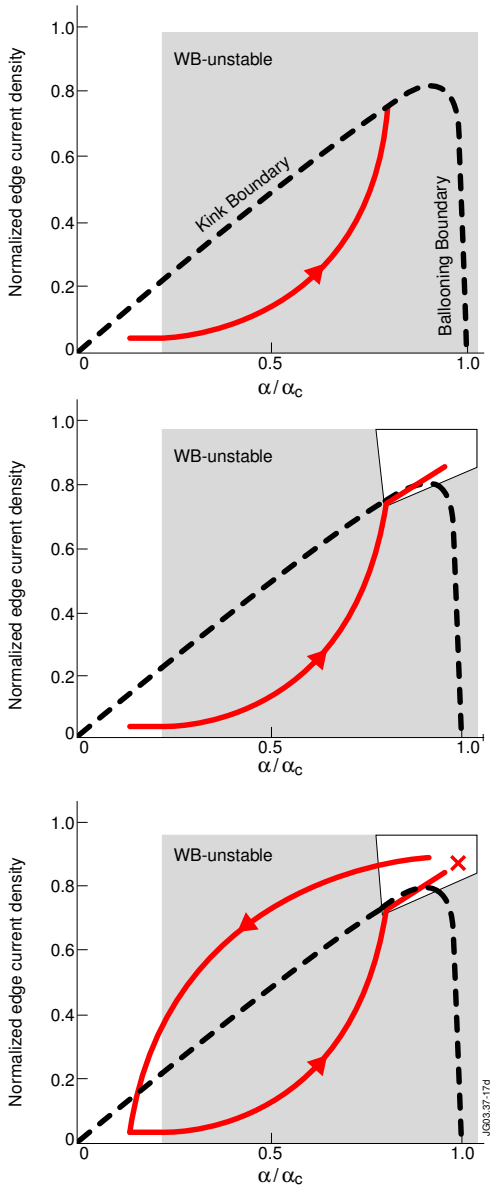

Figure 6.17: Individual steps of a modified peeling-ballooning cycle that takes into account the WB mode observations: (a) After the previous ELM crash the pedestal pressure initially builds up unperturbed, but, with the onset of WB modes and the associated increase in inter-ELM losses, the pressure build-up is slowed down, allowing for the edge current to build up on a comparative timescale until the kink-limit is reached. (b) ELM precursors become destabilised at the kink-limit, and their interaction with WB modes weakens or stabilises the WB modes, allowing for a further build-up of the pedestal pressure along or near the kink-limit. (c) The ELM is finally triggered at the ideal ballooning limit, which is now assumed to impose a hard limit.

at this stage, because experimentally the ELM precursors are not seen to trigger the ELM). The weakening of WB modes associated with the occurrence of the ELM precursors allows for a further build-up of the pedestal pressure along or near the kink-limit. The pedestal may shortly move again into the kink-stable region, where the precursors become stabilised, but with the reappearance of WB modes the kink-limit will be reached soon again, leading to the observation of intermittently existing precursors (as in figure 6.9). If the pressure build-up occurs entirely within the kink-unstable region, the precursors will be continuously present. At this stage the mode numbers of the most unstable precursor modes will eventually change during the pedestal evolution, leading to the occurrence of a sequence of precursors with different mode numbers or the existence of more than one precursor mode at a time (this has been reported in [8]). The ELM is finally triggered when the pedestal reaches the ideal ballooning limit (step 3), which, in contrast to the conventional model for the peeling-ballooning cycle, is now assumed to impose a hard limit. In this respect, certain theoretical works [30, 31] predict a general explosive feature of the ideal ballooning instability ("detonation") emerging from non-linear effects through the development of fine-scale substructures ("fingers"). After the crash the cycle repeats again starting from a state of low pressure/low current. Notice that, unlike in the conventional peeling-ballooning cycle, the starting point for the new cycle is not to be located at the kink-stability boundary, because the end of the crash is determined by processes related to the nonlinear ballooning and not to the kink-instability. According to this new peeling-ballooning cycle, the ELM precursors (kink or peeling-ballooning modes) observed on JET certainly play an important role in the cycle but are not directly involved in the ELM event itself.
The picture is not yet complete. Depending on the individual discharge conditions WB modes might be more or less effective in delaying the pressure build-up with respect to the peeling and ballooning stability limits. The three situations that can arise are depicted in figure 6.18. Curve 1 corresponds to the case of relative strong WB modes, where the kink-limit is reached well before the ELM. As there is a rather large gap to the ideal ballooning limit, the ELM precursors will be observed over longer times in that case. In the case of slightly less effective WB modes, the pedestal state might reach the stability limits in the vicinity of the upper-right corner of the stability triangle (curve 2). The ELM precursors are then only short-lived, and the ELM crash occurs shortly after their appearance. This case is often observed in JET, where the shorter precursors last on the order of 0.5 to 2 ms, and the ELM occurs while the precursor amplitudes are still growing. An example has been shown in figures 6.1 and 6.11, prior to the first ELM. Due to their shortness these precursors cannot affect significantly the evolution of the pedestal build-up through WB mode suppression. The hypothesis is that the radial displacements associated with the precursor oscillations themselves give rise to local transient steepenings of the pedestal.

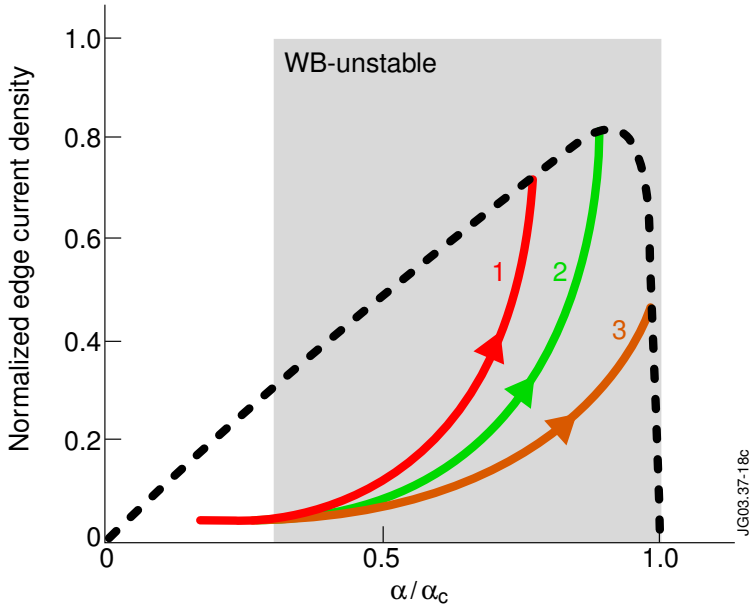

Figure 6.18: The three possible situations that may arise depending on the WB amplitude and discharge conditions. Curve 1 corresponds to the case of relative strong WB modes, where the kink-limit is reached well before the ELM. ELM precursors will be observed over longer times in that case. In the case of slightly less effective WB modes, the pedestal state might reach the stability limits close to the upper-right corner of the stability triangle (curve 2). The ELM occurs then shortly after the appearance of ELM precursors. The pedestal evolution given by the curve 3 corresponds to the case where the ideal ballooning limit is reached directly. No ELM precursors are then observed. The latter case may arise with rather weak WB modes, or in discharges where strong gas fuelling limits the amount of edge current.

Since in the upper-right corner of the stability triangle the pedestal is already close to the ideal ballooning limit, the oscillations may cause the pedestal to cross the ideal ballooning limit, where the ELM is the triggered. Finally, the pedestal evolution given by the curve 3 in figure 6.18 corresponds to the case where the ideal ballooning limit is reached directly. No ELM precursors are then observed, and the ELM is directly triggered. There are at least two situations where this may occur. First, if the WB modes are rather weak, and second, if strong gas puffing is applied. As modelling calculations predict [29], the increase in edge collisionality associated with the gas puffing leads to a decrease of the edge current density, keeping the pedestal state away from the kink-limit. This is corroborated by experiment, because ELM precursors are currently not observed at JET with strong gas puffing, even in discharges at high triangularity with strong WB modes and low type-I ELM frequency (mixed type-I/type-II ELM

regime).

6.6 Summary and Discussion

Several features of an edge instability very commonly observed in JET and named the WB mode have been presented. WB modes are observed in JET exclusively in the H-mode regime, and are thus apparently linked to the existence of a pedestal. They are composed of several bands of continuously bursting magnetic fluctuation, whose frequency evolution tends to follow the evolution of the edge electron temperature measured near the pedestal top. This is probably related to the strong diamagnetic drift associated with the large pedestal gradients. Evidence for their involvement in the pedestal and ELM dynamics has been presented. It has been shown that WB modes influence the build-up of the pedestal temperature (and, linked to this, also of the pedestal pressure) of the electrons, most likely through a continuous release of energy across the plasma boundary. This is further consistent with the observed correlation of WB mode activity with the time Δt_{ELM} between consecutive ELMs. An exclusive interaction between the type-I ELM precursor modes and the WB modes has been identified. The onset of type-I ELM precursors is associated with a weakening, or even an inhibition, of the WB modes. The reduced WB mode amplitude often results in a faster build-up of the electron pressure at the pedestal, until it is finally interrupted by the ELM event. The enhancement of WB modes through gas puffing at high triangularity may provide an explanation for the occurrence of the new regime identified on JET, that has been called mixed type-I/type-II ELM regime. WB modes provide the enhanced turbulence identified in the references [25, 26] as a characteristic signature of the mixed type-I/type-II ELM regimes, but it needs to be emphasized that WB modes are also present in regimes regarded as pure type-I ELM regimes. A modified version of the peeling-ballooning cycle that includes the WB physics has been proposed. It predicts the type-I ELMs to be triggered at the ideal ballooning limit rather than the kink-/peeling-boundary, and is therefore consistent with the experimental observation that the ELM precursors (thought to be kink-modes/peeling-ballooning modes) seem not to trigger the ELM on JET. The precursors do however favour an earlier onset of the ELM through two effects: Firstly, through the observed suppression of the WB modes. Secondly, the radial displacements associated with the precursor oscillations may cause transient local steepenings of the pedestal pressure gradient, and thus favour the onset of ideal ballooning modes as a secondary instability.
Several open questions remain. Certainly, the most relevant one concerns the nature of the WB modes, which remains an unresolved issue. WB modes show no radial phase inversions, hence magnetic islands can be excluded. The list of candidates can be further reduced by the identification of WB driving or stabilising forces. Current driven modes can be excluded from the observed WB mode en-

hancement through gas puffing (at high triangularity). For current driven modes a weakening would have been expected due to the reduced edge current density associated with the high edge collisionality. The example discussed in section 6.3, where WB modes become stabilised by the arrival of a large sawtooth heat pulse at the plasma edge, serves to exclude ideal pressure driven modes. In that case, the sawtooth heat pulse causes a sudden increase of the edge temperature while the edge density remains nearly unaffected. Therefore, the WB suppression coincides with a sudden increase in the overall edge pressure, which is difficult to justify in terms of an ideal pressure driven mode. Nevertheless, the increase in edge temperature implies a decrease in edge resistivity, and thus resistive pressure driven modes cannot be excluded. Resistive ballooning modes (RBMs) have been regarded as a possible candidate to explain the WB modes in [7], where several arguments in favour or against this are discussed in detail. In particular, RBMs have twisting parity [32] and certain branches are expected to propagate in the direction of the electron diamagnetic drift [33], like the WB modes, but on the other hand the n-numbers observed in the experiment are rather low. A ballooning character of the WB modes was inferred in [7] from the observed amplitude asymmetry measured by coils on the inboard and outboard side of the plasma. However, recent modelling calculations performed with MISHKA [34] in real JET geometry have shown that mode-induced field perturbations are subject to higher damping on the HFS than on the LFS, and that this may introduce a strong inboard-outboard asymmetry in the magnetically measured signal amplitudes even if the mode itself does not have ballooning character (more details are given in [8]). Therefore, the question whether WB modes have ballooning character or not is left open.

Kelvin-Helmholtz (KH) instabilities [35] may provide an alternative explanation for the WB modes. KH modes are driven by the shear of the parallel plasma velocity, which is expected to be large at the H-mode barrier, while density and temperature gradients provide a stabilising effect. They are not expected to be highly localised but to have rather broad radial extent, and are not bound to a certain rational surface, that is, their m and n numbers do not have to correspond to the local value of the safety factor. However, the m numbers that have been obtained for the WB bands with $n = -1$ do correspond to a rational surface localised close to the plasma boundary. The stabilisation of WB modes by the ELM precursors could be easily explained in terms of KH, because one expects the ELM precursors to affect the rotational shear at the edge. In similar terms, the arrival of a large sawtooth heat pulse at the plasma edge should be able as well to influence the parallel velocity shear and thus possibly stabilise the WB modes. Recent calculations that take into account the stabilising effect of both the temperature and the density gradients on the KH modes, show that they propagate (in the frame where $E_r = 0$) in the direction of the electron diamagnetic drift, with a frequency that is a fraction of the electron diamagnetic

frequency [36].
From the point of view of ELM and pedestal physics, it is desirable to ascertain whether MHD activity comparable to JET's WB modes is observed elsewhere. Taking into account how commonly WB modes are observed on JET, one might expect them to be present also in other machines. It is unlikely that WB modes are related to the quasi-coherent mode (QCM) observed during the EDA-regime [37] of Alcator C-Mod, although there are some similarities. In particular, both modes occur at the plasma edge, rotate in the direction of the electron diamagnetic drift and seem to lead to a continuous loss of energy into the SOL [38]. There are, however, three major differences. First, the observed toroidal mode numbers of the QCM are in the range n = 15-18 [39], which is much larger than those of the WB modes. Second, WB modes are currently composed of several bands of magnetic fluctuation activity, while for the QCM it is only a single band. Third, unlike the WB modes, the QCM is not observed in other H-mode regimes, such as in standard ELM-free H-modes.
With the perspective on ITER operation and the avoidance of large transient heat-loads onto the divertor tiles the achievement of a stationary high confinement regime combined with small ELMs is certainly desirable. These conditions have been established in the type-II or 'grassy' ELM regimes of DIII-D [40], JT-60U [41] and ASDEX Upgrade [27]. On JET, this could not be achieved yet, and it is questionable whether a mere further enhancement of the WB activity will be sufficient to obtain a pure type-II ELM regime. As shown in section 6.3, the WB modes are potentially capable of bringing the edge electron temperature to saturation. However, the edge density is not greatly affected by them but keeps increasing, at least in the gas puffed discharges. This highlights a serious problem because without a constant pedestal pressure a steady state regime will not become possible. It might be that WB modes on their own are not sufficient but that additional effects concerning the edge-related MHD have to come into play. A thorough comparison from the MHD point of view of the small ELM regimes obtained in other tokamaks is likely to clarify whether these rely on WB-like activity and whether there is a key ingredient that is missing in JET. This is intended for future work.

Acknowledgements

This work has been performed under the European Fusion Development Agreement. One author (C P P) wants to acknowledge the financial support of the Dutch Research Organisation NWO.

References

[1] Zohm H 1996 *Plasma Phys. Control. Fusion* **38** 105

[2] Connor J W 1998 *Plasma Phys. Control. Fusion* **40** 191

[3] Connor J W 1998 *Plasma Phys. Control. Fusion* **40** 531

[4] Leonard A W *et al* 1999 *J. Nucl. Mater.* **266-269** 109

[5] Janeschitz G 2001 *J. Nucl. Mater.* **290-293** 1

[6] Connor J W, Hastie R J, Wilson H R 1998 *Phys. Plasmas* **5** 2687

[7] Smeulders P *et al* 1999 *Plasma Phys. Control. Fusion* **41** 1303

[8] Perez C P *et al*, 'Type-I ELM Precursor Modes in JET', EFDA-JET Preprint EFD-P(02)11, submitted to *Nucl. Fusion*

[9] Nave M F F *et al* 1997 *Nucl. Fusion* **37** 809

[10] Huysmans G T A, Hender T and Alper B 1998 *Nucl. Fusion* **38** 179

[11] Merezhkin V G 1978 *Sov. J. Plasma Phys.* **4** 152

[12] Klueber O *et al* 1991 *Nucl. Fusion* **31** 907

[13] Buttery R J *et al* 2003 *Nucl. Fusion* **43** 69

[14] JET Team (presented by Jones T T C) 1995 *Plasma Phys. Control. Fusion* **37** A359

[15] Costley A E 1991 Microwave Reflectometry *Diagnostics for Contemporary Fusion Experiments (International School of Plasma Physics, Varenna)* ed P E Stott it et al (Bologna: Editrice Compositori) p 113

[16] Sips A C C and Kramer G J 1993 *Plasma Phys. Control. Fusion* **35** 743

[17] Gowers C *et al* 1995 *Rev. Sci. Instrum.* **66** 471

[18] Hazeltine R D 1974 *Phys. Fluids* **17** 961

[19] Kim Y B, Diamond P H, Groebner R J 1991 *Phys. Fluids B* **3** 2050

[20] Braithwaite G *et al* 1989 Rev. Sci. Instrum. **60** 2825

[21] Saibene G *et al* 1999 *Nucl. Fusion* **39** 1133

[22] Loarte A *et al* 2001 *Proc. 28th EPS Conf. on Controlled Fusion and Plasma Physics (Madeira, 2001)* P3.005

[23] Saibene G *et al* 2001 *Proc. 28th EPS Conf. on Controlled Fusion and Plasma Physics (Madeira, 2001)* P3.002

[24] Loarte A *et al* 2002 *Plasma Phys. Control. Fusion* **44** 1815

[25] Saibene G *et al* 2002 *Plasma Phys. Control. Fusion* **44** 1769

[26] Becoulet M *et al* 2002 *Plasma Phys. Control. Fusion* **44** 103

[27] Stober J *et al* 2001 *Nucl. Fusion* **41** 1123

[28] Snyder P B *et al* 2002 *Phys. Plasmas* **9** 2037

[29] Parail V *et al* 2002 *Proc. 19th IAEA Fusion Energy Conference (Lyon, 2002)* IAEA-CN-94-TH/P3-08

[30] Hurricane O A, Fong B H, Cowley S C 1997 *Phys. Plasmas* **4** 3565

[31] Fong B H 1999 "Metastable and explosive properties of ballooning modes in laboratory and space plasmas", *PhD thesis*, available at http://www.asp.ucar.edu/∼bhlfong/thesis.pdf

[32] Strauss H R 1981 *Phys. Fluids* **24** 2004

[33] Diamond P H *et al* 1985 *Nucl. Fusion* **28** 1116

[34] Mikhailovskii A B *et al* 1997 *Plasma Phys. Rep.* **23** 844

[35] D'Angelo N 1965 *Phys. Fluids* **8** 1748

[36] Rogister A, Singh R *in preparation*

[37] Greenwald M *et al* 1997 *Nucl. Fusion* **37** 793

[38] Snipes J A *et al* 2001 *Plasma Phys. Control. Fusion* **43** L23

[39] Snipes J A *et al* 2002 *Proc. 29th EPS Conf. on Controlled Fusion and Plasma Physics (Montreux, 2002)* P1.057

[40] Ozeki T *et al* 1990 *Nucl. Fusion* **30** 1425

[41] Kamada Y *et al* 2002 *Plasma Phys. Control. Fusion* **44** A279

Chapter 7

Conclusions and outlook

New and unexpected MHD phenomena have been identified in JET: (a) the regular occurrence of precursor modes prior to type-I ELMs, and (b) the relevance of the Washboard mode. Their properties and implications for the plasma edge have been studied extensively, and the observations have been compared with present theoretical ELM models (chapters 5 and 6).
The outcome of these studies does not support the widely held view that type-I ELMs are caused by kink modes or coupled kink-ballooning modes. Instead, an alternative model for a type-I ELM cycle has been proposed, which is consistent with the experimental observations presented. According to this model, the type-I ELMs are triggered by ideal non-linear ballooning modes [1].
In analogy to type-I ELMs, there have been some attempts in the past to find an explanation for the type-II ELMs in the context of ideal peeling and ballooning modes [2–4]. Within that work, semi-empirical models for type-II ELMs have been developed with the help of stability simulations. The experimental observations on Washboard modes presented here now indicate that (at least on JET) it may not be possible to describe the type-II ELMs within the scope of ideal MHD. Other instabilities, such as resistive ballooning modes or Kelvin-Helmholtz instabilities, need to be considered. If the above considerations are confirmed, then a reassessment of the understanding of ELMs would become necessary.
The work presented here is highly relevant for ITER. A number of projects are intended for future work:
The highest priority has the identification of the type-I ELM mechanism, maybe confirming the non-linear ideal ballooning model discussed above. Thus, the next natural step is to analyse the ELM crash itself (figure 7.1), to which relatively little attention has been paid within this thesis. Due to the short duration of the ELM collapse and its highly turbulent nature this is not an easy task, and it remains to be clarified whether the diagnostics available on JET are sufficient to draw any conclusions. The ultimate aim is to find out whether it is possible to ameliorate the ELM by damping its mechanism.

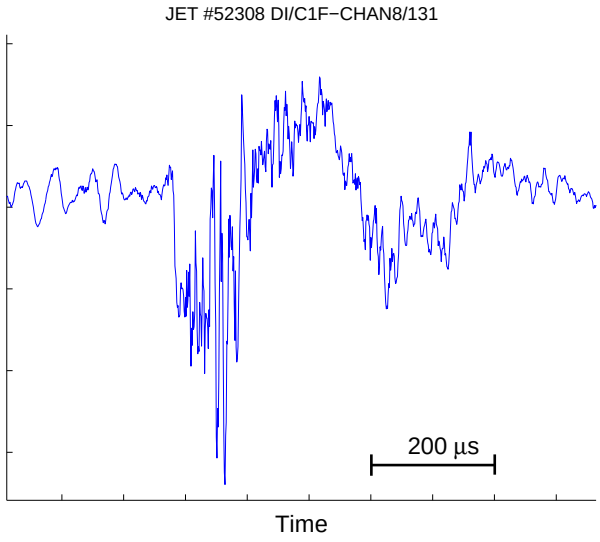

Figure 7.1: Magnetic perturbation caused by an ELM, measured by a Mirnov coil on the low field side.

Since pure type-II ELM regimes could so far not be established on JET, and might be required for ITER, further understanding of the type-II ELM physics is necessary. Its precise relationship with the Washboard modes needs to be clarified. A thorough comparison from the MHD point of view of the small ELM regimes obtained in other tokamaks is likely to clarify whether these rely on Washboard mode-like activity, and whether there is a key ingredient that is missing in JET and possible in ITER. A comparison of data from type-II ELM discharges in ASDEX Upgrade with the JET observations presented here is foreseen.

Further insight can be expected from the study of parametric dependencies of the ELM cycle and precursors. It would be worth to confirm the evolution of j_{edge} and $\alpha/\alpha_{\mathrm{crit}}$ during the ELM cycle. These quantities can so far not be measured directly in JET, but improved edge measurements combined with transport calculations (for instance from the JETTO code) may prove sufficient. When these quantities are better known, it is worth to determine the distribution of the precursor n-numbers directly in the space of normalised j_{edge} and $\alpha/\alpha_{\mathrm{crit}}$.

It would be desirable to unambiguously identify the type-I ELM precursor modes with medium and high toroidal mode numbers as coupled peeling-ballooning modes. A possible option would be to repeat the analysis performed by Huysmans *et al* [5], which led to the identification of the Outer Modes as external kink modes, for precursors with higher n numbers. This requires a higher edge temperature and/or density to improve the response of the soft-X ray cameras to edge fluctuations. It would also require the repair of at least part of the radiation damaged soft-X ray cameras to increase the number of channels available. In or-

der to get a higher edge temperature at the range of edge collisionalities where the intermediate to high n precursors are observed, it is necessary to operate the plasma with sufficient heating power at higher magnetic field and plasma current. An increase of the total heating power available at JET has been recently implemented, and a repair of soft-X ray cameras is also envisaged.

References

[1] Cowley S C, Wilson H, Hurricane O A and Fong B 2003 *Plasma Phys. Control. Fusion* **45** A31

[2] Snyder P B *et al* 2002 *Phys. Plasmas* **9** 2037

[3] Saarelma S *et al* 2003 *Nucl. Fusion* **43** 262

[4] Lonnroth J S *et al* 2003 *Proc. 30th EPS Conf. on Controlled Fusion and Plasma Physics (St Petersburg, 2003)* P1.184

[5] Huysmans G T A, Hender T C, and Alper B 1998 *Nucl. Fusion* **38** 179

Summary

The aim of nuclear fusion energy research is to demonstrate the feasibility of nuclear fusion reactors as a future energy source. The tokamak is the most advanced fusion machine to date, and is most likely the first system to be converted into a reactor.
An important subject of nuclear fusion research is the study of the equilibrium and stability of a plasma with respect to large scale displacements. In a tokamak, several instabilities can occur. A class of edge instabilities that occur in the high confinement regime, H-mode, have been called Edge Localised Modes (ELMs). ELMs are relaxation oscillations that cause quasiperiodic energy and particle losses out of the confined plasma into the scrape-off layer. These losses are of concern for future burning fusion plasmas, such as ITER, due to the large transient heat loads expected on plasma facing components in contact with the scrape-off layer. These heat loads may reduce the target lifetime below tolerable levels.
Although the existence of ELMs has been known for many years, their physics is not well understood yet. Much effort has been spent world-wide in an attempt to improve the understanding of these instabilities. A review of the present state of ELM research is given. Empirically, at least three types of ELMs have been identified, which are normally classified as type-I, type-II and type-III ELMs. From the point of view of plasma stability, research has increasingly focussed on the role of certain MHD instabilities, namely (finite-n) ballooning and kink (peeling) modes, as well as coupled ballooning-kink modes, leading to the proposition of a theoretical model called the peeling-ballooning cycle. This thesis presents new insight into ELMs obtained from the analysis of experimental data in the JET tokamak, and compares the observations with present theoretical ELM models.
Low frequency coherent type-I ELM precursor modes have been identified. Their properties are studied in detail. Precursors with low toroidal mode numbers are known to be external kink instabilities, while experimental findings and their comparison with stability calculations suggest that the precursor modes with higher toroidal mode numbers are not pure external kinks but coupled ballooning-kink modes. Above a certain edge collisionality the precursors seem to be absent, indicating that a sufficiently high edge current is important to destabilise the precursors. In spite of their regular occurrence, there is no evidence that the

precursor mode growth rate accelerates rapidly before the ELM. This is regarded as an indication that external kink modes or coupled peeling-ballooning modes do not trigger the ELMs, which would contradict present theoretical ELM models.

Another type of instability are the Washboard (WB) modes, a very common edge instability regularly observed in the H-mode regime in JET. Since their discovery in the late 90's, rather little attention has been paid to them, either theoretically or experimentally. So far they have not been regarded as an ELM-relevant instability. However, evidence for their involvement in the pedestal and ELM dynamics is presented here.

It is shown that WB modes influence the build up of the pedestal temperature of the electrons, most likely through a continuous release of energy across the plasma boundary. Furthermore, the existence of an exclusive interaction between the WB modes and the type-I ELM precursor modes has been identified. The onset of type-I ELM precursors is associated with a weakening, or even an inhibition, of the WB modes. The reduced WB amplitude often results in a faster build-up of the electron pressure at the pedestal, until it is finally interrupted by the ELM event.

The enhancement of WB modes through gas puffing at high triangularity can provide an explanation for the occurrence of a regime recently identified on JET that has been called the mixed type-I/type-II ELM regime. WB modes provide the enhanced broadband turbulence characteristic of the mixed type-I/type-II ELM regimes.

A modified version of the peeling-ballooning cycle that includes the WB physics is proposed. It predicts that the type-I ELMs are triggered at the ideal ballooning stability boundary, rather than at the kink stability boundary. It is therefore consistent with the experimental observation that the ELM precursor modes do not seem to trigger the ELM collapse on JET.

A number of future activities are envisaged. The analysis of the ELM collapse itself with the help of fast experimental data, and its comparison with non-linear ballooning models have highest priority. In addition, a comparison of the type-II ELM regime in ASDEX Upgrade with the observations made on JET (and its possible implications for ITER) is of primary interest. The continuation of type-I ELM precursor mode studies on JET may also yield further insight into the complex ELM phenomenon.